Role of Additives on the Kinetic and Thermodynamic Properties of $Mg(NH_2)_2$+LiH Reactive Hydride Composite

Von der Fakultät für Maschinenbau
der Helmut-Schmidt-Universität /
Universität der Bundeswehr Hamburg
zur Erlangung des akademischen Grades eines
Doktor-Ingenieurs
genehmigte
DISSERTATION
vorgelegt von

von
Gökhan Gizer

aus
Ağrı, Türkei

Hamburg 2020

Vorsitzender des Prüfungsausschusses: Univ.-Prof. Dr.-Ing. Jens P. Wulfsberg
1. Gutachter: Univ.-Prof. Dr.-Ing. habil. Thomas Klassen
2. Gutachter: Univ.-Prof. Dr. habil. Chiara Milanese
Tag der mündlichen Prüfung: 27.05.2020

Role of Additives on the Kinetic and Thermodynamic Properties of $Mg(NH_2)_2$+LiH Reactive Hydride Composite

Gökhan Gizer

Abstract

The hydrogen storage properties of the Li-Mg-N-H system composed of $Mg(NH_2)_2$ and LiH are investigated. In the last decade, the Li-Mg-N-H system attracted increasing attention due to its high hydrogen storage capacity (5.5 wt.%), favourable dehydrogenation enthalpy ($\Delta H \approx 40$ kJ·mol$^{-1}H_2$) and good reversibility. Theoretical calculations show that the thermodynamic properties allow a dehydrogenation reaction temperature of 90°C at a pressure of 1 bar of H_2, which is close to the operating temperature of proton exchange membrane fuel cells (PEMFCs). However, sufficient operating dehydrogenation rates are obtained only at temperatures higher than 220°C, due to kinetic constrains. In this work, a thorough study of the effect of three selected additives (i.e. K-modified $Li_xTi_yO_z$, $LiBH_4$ and $K_2Mn(NH_2)_4$) on the material kinetic properties is carried out. The effect of lithium titanates ($Li_xTi_yO_z$) on the Li-Mg-N-H system is studied, to the best of my knowledge, for the first time. Their modification with potassium leads to the formation of K_2TiO_3 species, which act as catalyst and accelerate both absorption and desorption kinetics without altering the rate-limiting step. The second part of the thesis is devoted to the study of the Li-Mg-N-H system in combination with $LiBH_4$. $LiBH_4$ stabilizes the dehydrogenation product $LiNH_2$ forming the $Li(BH_4)(NH_2)_3$ phase at the interface of amide-hydride particles. During hydrogenation, the highly ionic conductive $Li_4(BH_4)(NH_2)_3$ supports the diffusion of small ions through the interfaces of the amide-hydride matrix. In the last part of this work, the effect of the bimetallic amide additive $K_2Mn(NH_2)_4$ is studied. Structural characterizations show that the bimetallic amide $K_2Mn(NH_2)_4$ decomposes into Mn_4N and KH and these newly formed phases are stable for at least 25 cycles. A surprisingly fast reaction rate is observed at the last stage of the rehydrogenation reaction. Under the applied conditions, hydrogenation of the last 1 wt.% takes place in 2 minutes only, which is four times faster than observed in the respective Mg-Li-7KH sample. This work opens a new path to design appropriate additives to enhance the kinetic properties of Li-Mg-N-H systems for solid-state hydrogen storage.

Einfluss von Additiven auf die kinetischen und thermodynamischen Eigenschaften des reaktiven Hydridkomposits $Mg(NH_2)_2$+LiH

Gökhan Gizer

Zusammenfassung

In dieser Arbeit werden die Wasserstoffspeichereigenschaften des Li-Mg-N-H-Systems aus $Mg(NH_2)_2$ und LiH untersucht. In den letzten zehn Jahren erregte das Li-Mg-N-H-System zunehmend Aufmerksamkeit, was durch die hohe Wasserstoffspeicherkapazität (5.5 Gew.-%), der günstigen Dehydrierungsenthalpie ($\Delta H \approx 40$ kJ·mol$^{-1}H_2$) und der guten Reversibilität zu erklären ist. Theoretische Berechnungen zeigen, dass die thermodynamischen Eigenschaften eine Dehydrierungsreaktionstemperatur von 90°C bei einem Druck von 1 bar H_2 zulassen, welche nah an der Betriebstemperatur von Protonenaustauschmembran-Brennstoffzellen

(PEMFCs) liegt. Ausreichend technische Dehydrierungsraten werden jedoch aufgrund von kinetischen Einschränkungen nur bei Temperaturen von über 220°C erreicht. Mit dieser Arbeit wird eine ausführliche Untersuchung zu der Wirkung von drei ausgewählten Additiven (z.B. K-modifiziertes $Li_xTi_yO_z$, $LiBH_4$ und $K_2Mn(NH_2)_4$) auf die materialkinetischen Eigenschaften vorgestellt. Die Wirkung von Lithiumtitanaten ($Li_xTi_yO_z$) auf das Li-Mg-N-H-System wird nach bestem Wissen hier erstmals untersucht. Die Modifikation mit Kalium führt zur Bildung von K_2TiO_3-Mischoxiden, die als Katalysator fungieren und sowohl die Absorptions- als auch die Desorptionskinetik beschleunigen, ohne jedoch zu einer Änderung des geschwindigkeitsbestimmenden Schrittes zu führen. Der zweite Teil dieser Arbeit widmet sich der Untersuchung des Li-Mg-N-H-Systems in Kombination mit $LiBH_4$. $LiBH_4$ stabilisiert das Dehydrierungsprodukt $LiNH_2$, welches eine $Li(BH_4)(NH_2)_3$ Phase an der Grenzfläche der Amidhydridpartikel bildet. Während der Hydrierung unterstützt das stark ionisch leitfähige $Li_4(BH_4)(NH_2)_3$ die Diffusion von Ionen durch die Grenzflächen der Amid-Hydrid-Matrix. Im letzten Teil dieser Arbeit wird die Wirkung des Bimetallamidzusatzes $K_2Mn(NH_2)_4$ untersucht. Strukturelle Charakterisierungen zeigen, dass das Bimetallamid $K_2Mn(NH_2)_4$ in Mn_4N und KH zerfällt und diese neu gebildeten Phasen mindestens über die untersuchten 25 Zyklen lang stabil sind. Überraschend schnelle Reaktionsgeschwindigkeiten werden in der letzten Phase der Rehydrierungsreaktion beobachtet. Unter den gesetzten Bedingungen erfolgt die Hydrierung des letzten Gewichtsprozentes in nur zwei Minuten, was viermal schneller ist als in der Mg-Li-7KH-Vergleichsprobe. Diese Arbeit eröffnet einen neuen Weg zur Entwicklung geeigneter Additive im Hinblick auf die gezielte Verbesserung der kinetischen Eigenschaften von Li-Mg-N-H-Systemen zur Speicherung von Wasserstoff in Festkörpern.

Contents

1. Introduction

Since the second industrial revolution, humankind has experienced an uninterrupted period of economical and welfare growth. These have been possible thanks to a massive and widespread use of economically accessible and abundant fossil fuels as the primary energy source. Although there have been many advantages of using fossil fuels, the drawbacks associated to the atmospheric emission of pollutants during fossil fuels extraction, refinement and combustion (CO_2, NO_x, etc.) are nowadays threatening the existence of the life on planet earth. Additionally, nowadays, energy generation by renewable sources become a cheaper option compared to energy generation by fossil fuels [1]. The last report by Intergovernmental Panel on Climate Change (IPCC) in 2014 confirms that the anthropogenic influence on the climate system is clear and growing at a pace that calls for immediate actions [2]. As a consequence of the global warming effect, the average earth temperature increases, which results in extreme weather conditions, more intense droughts, rising sea levels, reduction in the yield of crops, etc. [3]. Moreover, the worsened quality of the air, in particular in heavily industrialized and populated areas, is causing serious health issues such as lung cancers, respiratory diseases, etc. In 2015, 174 states and the European Union have signed the Paris Agreement, in order to tackle climate change and accelerate the actions and investments needed for a sustainable future [4]. The long-term goal of the Paris Agreement is to limit global temperature increase to maximum 1.5 ℃. Figure 1.1 shows the anomaly of the average global temperature, for the period 1850–2017 and gives a prediction of the temperature rise for the period 2018–2065. By continuing the temperature rise trend, observed between 1980 and 2017, the average global temperature will increase of 1.5℃ by 2040 and 2℃ by 2065.

A special report published by IPCC on October 2018 reveals that limiting the temperature rise to 1.5℃ is not easy [5]. CO_2 emissions must be cut off 45 % relative to 2010 levels by 2030, and reach a net zero by 2050 (pre-industrial emission levels). Such a level of decarbonisation can be achieved only by replacing fossil fuel energy sources with renewable energy sources (solar, wind, tidal, etc.). However, due to their stochastic nature and uneven distribution on earth, an efficient exploitation is difficult to achieve. In this regard, hydrogen will play an important a significant role in exploiting the use of renewable energy sources.

Gaseous hydrogen can be produced in large scale by electrolysis, using renewables such as wind and solar power [6]. Combustion of hydrogen generates energy and water as by-product, as shown in reaction 1.1.

$$2H_2(g) + O_2(g) \rightarrow 2H_2O(l) + \text{Energy} \quad (1.1)$$

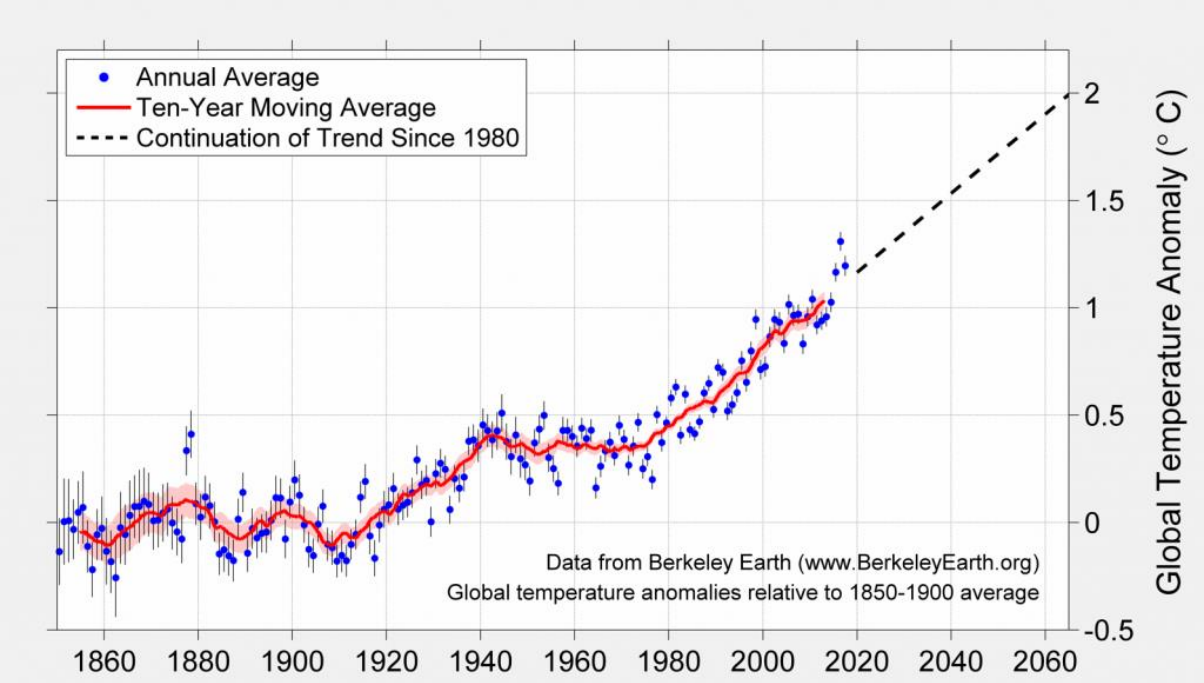

Figure 1.1 Global temperature anomalies relative to 1850–1900 average.
Source: *http://berkeleyearth.org/global-temperatures-2017/*

Hydrogen being the lightest element of the periodic table, its gravimetric energy density is the highest (120 MJ/kg (lower heating value, LHV)) with respect to that of any other fuel (e.g. gasoline or diesel: 46 MJ/kg, natural gas: 54 MJ/kg) [7]. However, as a gas at ambient conditions, its volumetric energy density is extremely low (Hydrogen: 0.01 MJ/L, gasoline: 34 MJ/L), 1 kg of hydrogen gas at ambient conditions (20°C and 1 bar) occupies a volume of 11 m^3 [8]. Three main strategies can be followed in order to increase the volumetric energy density of gaseous hydrogen: (i) compressing to 400-700 bar, (ii) liquefying at cryogenic temperatures, (iii) chemical storage in liquid form (e.g. organic hydrogen carriers LOHC) or in solid state (e.g. metal hydrides).

By compressing hydrogen to high pressure (700 bar), a volumetric capacity of 38 kg/m^3 can be obtained. Theoretically, compression of hydrogen to 700 bar requires 4% of the lower heating value (LHV) [9]. In practice, greater compression energies are required (17% of the LHV for 700 bar), due compressor inefficiencies and heating during fast fills. Besides that, the

required cylindrical tank design makes it difficult to use the available space in mobile vehicles efficiently. The gravimetric energy density of a high-pressure vessel depends strongly on the weight of the vessel itself. The tanks used in the vehicles nowadays are mainly Type IV tanks [10]. There is a non-metal liner inside a Type IV tank, to reduce the weight. Recently, liner-less all composite tanks are produced (Type V), which are costly but 10-15% lighter than Type IV tanks [11]. Although these tanks are only used in aerospace applications, new production techniques might reduce the cost of the tank, which may boost the usage in a wide range of applications.

When hydrogen is liquefied at −253°C, the volumetric capacity reaches to 70 kg/m^3 at 1 bar. Liquid hydrogen is commonly used in the field of spacecraft propulsion, and it can be used for underwater applications [12], [13]. The energy density can be further improved by compressing liquid hydrogen (81 kg/m^3 at 240 bar), which is called cyro-compressed hydrogen storage [14], [15]. Although the volumetric energy density of hydrogen is improved by liquefaction, the volume occupied is still four times higher than the respective volume occupied by kerosene-based jet fuel [16]. Additionally, boil-off phenomena and technical difficulties at such low temperatures are some of the challenges related to the use of liquid hydrogen for aviation [17].

Another strategy to store hydrogen implies the use of the so called LOHCs. [18], [19]. Besides the increased volumetric hydrogen storage density, the use of LOHCs presents several advantages. In fact, they can be stored for a long time without energy losses and transported using the existing fossil fuel-based distribution infrastructure [20]. Volumetric energy densities of LOHC can reach up to 70 kg/m^3, which is comparable to the one of liquid hydrogen [21]. Unfortunately, dehydrogenation of the LOHCs (e.g. dibenzyltoluene) is carried out at elevated temperatures (250°C–300°C) using expensive catalysts based on Ru or Pt. In addition, the stability and performance of the used catalysts through several de/rehydrogenation cycles is still unclear.

Hydrogen interacts with a large number of metals to form solid metal hydride compounds. Metal hydrides are classified by the nature of the chemical bond (ionic, metallic or covalent) between hydrogen and metal. Metallic bonds are present in interstitial hydrides, where hydrogen occupies interstitial sites of the metallic host's crystal lattice. This type of hydrides is usually able to operate at temperatures close to room temperature under a wide range of hydrogen pressures. Although the volumetric energy density of these hydrides can

reach up to 100 kg/m^3, low gravimetric capacities (< 3 wt.% H_2) are the main constraint to their widespread application.

1.1 Thermodynamics of metal hydrogen system

The formation of an interstitial hydride can be described as a reversible solid-gas reaction. The interaction between a metal ($M_{(s)}$) and hydrogen ($H_{2(g)}$) is herein explained. At certain temperature (T) and under certain pressure (P), $M_{(s)}$ reacts with $H_{2(g)}$ to form a metal hydride ($MH_{x(s)}$) according to reaction 1.2;

$$M_{(s)} + \frac{X}{2} H_2 \rightleftharpoons MH_{x(s)} + \mathrm{Heat}(T, P) \tag{1.2}$$

Clearly, this reaction is simplified and does not consider any possible multiple step reactions and the formation of intermediate phases. All hydrides considered in this thesis are stable under ambient conditions, i.e. hydride formation is exothermic and hydride decomposition is endothermic. Thermodynamics of hydrogen storage materials can be described with pressure-composition-isotherms (PCIs). PCIs provide useful information about the working temperatures and pressures of the hydride, as shown in Figure 1.2 [22]. The formation of a metal hydrides can be divided in the series of step reported in the following:

1. Molecular hydrogen (H_2) approaching the metal's surface experience the attraction of the Van der Waals forces , which confine it in a volume close to the metal surface. This phenomenon is called "physisorption".
2. Molecular hydrogen dissociates on the metal's surface and forms a metal-hydrogen bond. This phenomenon is called "chemisorption".
3. Chemisorbed hydrogen diffuses into the interstitial sites of metal's lattice and forms a solid solution (α phase) (Figure 1.2A-(a)).
4. Once a certain concentration of hydrogen is reached in a volume of the crystal lattice, a new phase characterized by a specific atomic metal-hydrogen ratio starts to form (β phase) (Figure 1.2A-(b)).
5. The growth of the β phase at the α/β interface proceeds until transformation into the β phase is complete (Figure 1.2A-(d)).

The relation between the formation of the hydride phase and the applied hydrogen pressure is described by the van't Hoff plot reported in Figure 1.2B. Using the van't Hoff equation, it is possible to obtain useful thermodynamic information regarding the

chemisorption processes, i.e. dependency of equilibrium pressure ($P_{eq.}$) on temperature, enthalpy variation ΔH and entropy variation ΔS (equation 1.1). Experimentally, the equilibrium pressure during the "plateau region" is often not perfectly constant, as shown in Figure 1.2C. The plateau slope is not necessarily constant over the length of plateau. The cause of the sloped plateau is attributed to compositional inhomogenities (e.g. around defects, partial oxidation, etc.). Furthermore, it is also observed in Figure 1.2C that the equilibrium pressure for the dehydrogenation process is lower than the equilibrium pressure for the hydrogenation process, which is known as "hysteresis". Hysteresis phenomenon is debated since 1930s [23], [24]. There are two main reasons discussed for the origin of hysteresis. One of them is the additional degree of freedom in metal hydrogen system other than the usual temperature, pressure and hydrogen concentration: mechanical strain in the lattice [23]. The phase with a higher concentration of hydrogen has much more mechanical strain, leading to the difference in absorption and desorption plateau pressures [25]. The other reason ascribed to the hysteresis is the plastic deformation during hydrogenated phase formation [26], [27]. The energy associated with the creation of dislocations due to plastic deformation must be overcome to initiate the phase transformation, resulting in an elevated pressure for the absorption plateau.

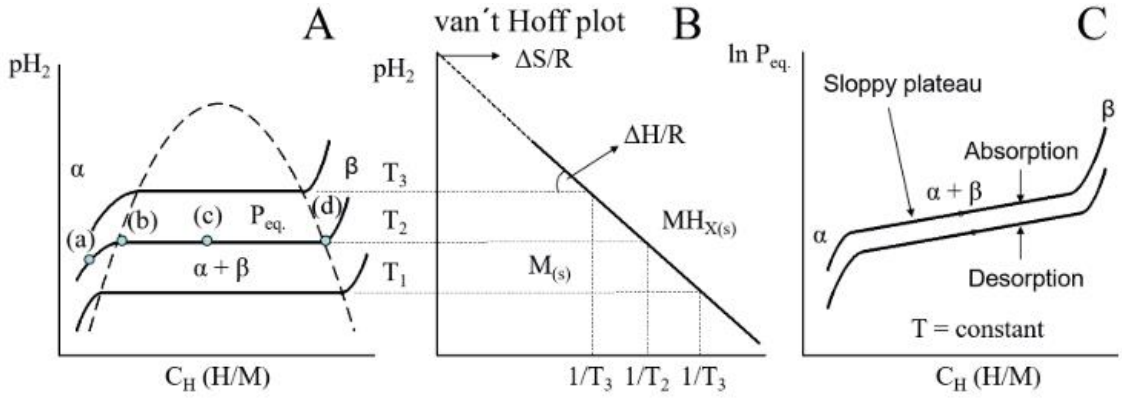

Figure 1.2 A Ideal PCIs in equilibrium conditions. **B** van't Hoff plot built from PCIs. **C** Real behavior of PCIs with slope and hysteresis. (adopted from [22])

$$lnP_{eq} = \left[\frac{\Delta H}{RT}\right] - \left[\frac{\Delta S}{R}\right] \tag{1.3}$$

If $lnP_{eq.}$ is plotted against 1/T as in Figure 1.2B, ΔH and ΔS values can be obtained from the slope of the line and intercept, respectively. ΔS indicates the entropy change for hydrogen, i.e., from molecular gas hydrogen to hydrogen in the hydride phase. For metal-hydrogen systems, the standard entropy change for hydrogen is usually considered to be 130 kJ/K mol,

however it can have sensibly different value depending on the considered hydride systems (e.g. for complex hydrides of boron, aluminium, nitrogen and alkaline or alkaline earth metals [28], [29]. ΔH of a system indicates how strong the metal-hydrogen bonds are and whether it takes a negative value (exothermic) for the hydrogenation and a positive value (endothermic) for the dehydrogenation. These two thermodynamic parameters, ΔH and ΔS, are quite important for the design of materials for practical applications. The equilibrium hydrogenation/dehydrogenation temperature of a hydrogen storage material under atmospheric pressure (~1 bar) can be calculated by using these parameters. Therefore, the ΔH of a hydrogen storage system should be low enough to achieve favourable operating temperature. In the case of fuel cells for mobile applications this temperature lies below 100°C. However, the most of common hydrides have rather high values of reaction enthalpy (ΔH: 50-200 $kJ \cdot mol^{-1}H_2$) [30]. Thus, their usage in mobile and stationary hydrogen storage application is hindered by their high operating temperatures. For example, MgH_2 having a dehydrogenation enthalpy of approx. 75 $kJ \cdot mol^{-1}H_2$ can release hydrogen at 1 bar of pressure at about 287°C [31].

"Complex hydrides" attracted considerable attention in the last decades, due to their high gravimetric and volumetric hydrogen capacities. Complex hydrides are composed of metal cations (e.g. often lightweight alkali or alkaline earth such Li, Na, Mg or Ca cations) and hydrogen-containing "complex" anions such as alanates [32], amides [33] and borohydrides [34]. Despite the fact that these compounds have high gravimetric hydrogen storage capacity, i.e. $Mg(BH_4)_2$: 14.9 wt.%, $LiBH_4$: 18.5 wt.% and $LiNH_2$: 10.5 wt.%, they are affected by sluggish reaction kinetics at low temperature and poor reversibility [35], [36].

In the beginning of the 2000´s it was reported that confining complex hydrides such as $NaAlH_4$, $LiBH_4$ or $NaBH_4$ in a nano-porous carbon based scaffold, their kinetic properties could be improved [37], [38]. Although this method was considered suitable also for improving the material kinetic properties, positive results were achieved only in few cases. In addition, the presence of the scaffolding material causes a significant reduction of the overall system hydrogen storage capacity. [39]. A possible approach to tune the reaction enthalpy of a hydrogen storage system based on complex hydride is the use of selected hydride mixtures. [40]. This approach, for complex metal hydrides, was reported first in the beginning of 2000´s by P. Chen et al. [33], J.J. Vajo et al. [41] and G. Barkhordarian et al. [42], and is called "reactive hydride composites".

1.2 Reactive hydride composites

It is discussed in the previous subsection that although some complex hydrides have very high gravimetric hydrogen capacities, their high thermodynamic stabilities and poor reversibility limit their possible range of applications. In the reactive hydride composites concept (RHCs), two or more hydride react exothermically with each other during dehydrogenation, to form one or more common reaction products. The thermodynamic destabilization in these systems is based on the exothermic heat of formation of the common compound(s), compensating in part for the endothermic hydrogen release, and vice versa for absorption. As the consequence of this thermodynamic reduction of the overall heat of reaction, i.e. an apparent "destabilization" of the hydrogen bond, these systems offer thermodynamically significantly reduced operating temperature.

The destabilization approach was applied by Chen et al. in 2002 on $LiNH_2$+LiH. This system could reversibly absorb/desorb ~ 6.5 wt.% of hydrogen according to reaction 1.4 [33];

$$Li_2NH + H_2 \leftrightharpoons LiNH_2 + LiH \qquad \Delta H = \sim 45\ kJ \cdot mol^{-1} \qquad (1.4)$$

Temperatures higher than 250 °C are required to release hydrogen from $LiNH_2$+LiH in reaction 1.4, thus this system is not suitable for most applications.

Subsequently, the RHC system $LiBH_4$+MgH_2 was reported by Vajo et al. [45] and Barkhordarian et al. [42]. The enthalpy variation associated to the decomposition of $LiBH_4$ to LiH+B+3/2H_2 (13.6 wt.%) is ~74 kJ·mol$^{-1}H_2$. A new system with a hydrogen storage capacity of 11.4 wt.% and a reduced reaction enthalpy (~40.5 kJ·mol$^{-1}H_2$) can be obtained when adding to $LiBH_4$ MgH_2 in the stoichiometric ratio 2:1. The dehydrogenation reaction of this RHC occurs as in reaction 1.5;

$$LiBH_4 + \frac{1}{2}MgH_2 \leftrightarrow LiH + \frac{1}{2}MgB_2 + 2H_2 \qquad (1.5)$$

As it has been proved by Vajo et al. and Barkhordarian et al., the key for the achieved destabilization and reversibility is the formation of MgB_2 [42].

As further systems, by substituting the Li^+ cation in amides like in reaction 1.4 with other alkaline and alkaline earth metal cations, several amide–hydride systems were discovered

[46]–[49]. The system $Mg(NH_2)_2$+2LiH ($\Delta H \approx 40\ kJ \cdot mol^{-1}$) reversibly desorbs ~ 5.5 wt.% H_2, according to reactions 1.6 and 1.7 [48], [50], [51];

$$2Mg(NH_2)_2 + 4LiH \leftrightharpoons Li_2Mg_2(NH)_3 + LiNH_2 + LiH + 3H_2 \quad (1.6)$$

$$Li_2Mg_2(NH)_3 + LiNH_2 + LiH \leftrightharpoons 2Li_2Mg(NH)_2 + H_2 \quad (1.7)$$

According to the calculated thermodynamic properties of the $Mg(NH_2)_2$+2LiH stoichiometric mixture, operating temperatures of 90°C can be achieved at 1 bar, which is highly attractive for mobile applications [52]. However, due to kinetic constraints, sufficient dehydrogenation rates can be obtained only at temperatures above 180°C [53]. Studies on reaction mechanism of $Mg(NH_2)_2$+LiH system indicate that the diffusion of small ions (e.g., Li^+, Mg^{+2}, and H^+) determine the material reaction properties [54]–[57]. Consequently, to identify additives capable to support/enhance the ions mobility in amide−hydride systems is crucial for tuning the reaction properties of this class of materials.

1.3 Scope of the work

As discussed in the previous section, the $Mg(NH_2)_2$+2LiH composite possesses relatively high reversible hydrogen storage capacity (i.e., 5.5 wt. wt.%) and suitable thermodynamic properties (i.e., $\Delta H_{des} \approx 40\ kJ \cdot mol^{-1}H_2$ and $\Delta S_{des} = 112\ J/mol\ H_2 \cdot K$) for on-board application in fuel cell driven vehicles (FCVs). However, for such applications, an important barrier to overcome is the poor reaction rate that hinders the dehydrogenation process of the system $Mg(NH_2)_2$+2LiH. The sluggish interface reactions, resulting from the relocation of atoms (such as Li^+, Mg^{2+}, and H^+ ions) across amide−imide and imide−hydride phase boundaries and the mass transport through the thus-formed imide layer (during the H_2 de/rehydrogenation for the amide−hydride system), is the consequence of the high activation energy barriers which plague these processes. These constraints lead to an increase of the material operating temperatures and therefore preclude its practical applications. Consequently, in order to consider this material suitable for vehicular applications, finding effective strategies to overcome these kinetic barriers is essential.

An effective strategy for tuning the kinetics of the amide−hydride system is to reduce the particle sizes down to the nanometer range. This approach effectively improves the material hydrogen storage performance due to the shortened diffusion distances between amides/imides/hydrides and the increased contact area [58]. In the literature, strong dependence

between the reaction kinetics and particle size of amide–hydride systems is reported both experimentally and theoretically [55], [59]. Although ball milling technique is an efficient technique to reduce the activation energy and dehydrogenation onset temperatures of hydrogen storage materials via microstructural refinement and compositional homogenization [55], [60], its benefits disappear over subsequent de/rehydrogenation cycles by committing coarsening. Another possibility to enhance the material kinetic properties is the use of selected additives/catalysts [51], [61]–[65] for inoculation during phase transformation. This approach is applied in this research work. Earning from the works recently reported in literature, I decided to investigate the effect of K-modified $Li_xTi_yO_z$, $LiBH_4$ and $K_2Mn(NH_2)_4$ on the hydrogen sorption properties of $Mg(NH_2)_2$+2LiH system.

In the first part of the thesis, I investigate the impact of the addition of potassium modified $Li_xTi_yO_z$ to the system $Mg(NH_2)_2$+2LiH. Potassium containing additives (KH, KOH, KF) are known for effectively improving the sorption properties of pristine $Mg(NH_2)_2$+2LiH [51], [66], [67]. However, hydrogen release and uptake performed at high temperature (>180°C) result with agglomeration of the particles of potassium based additives as well as increase in the inhomogeneous degree of mixing and distribution [68]. Therefore, my particular interest is to accommodate potassium within a stable structure in order to avoid agglomeration of potassium-related species. Additionally, I expect to observe the improvement from this modified additive on reaction kinetics of amide-hydride system. Puszkiel *et al.* showed that in 2LiH+MgB_2/2$LiBH_4$+MgH_2 RHC the core-shell Li_xTiO_2 nanoparticles act as Li^+ pumps, enhancing the de/rehydrogenation rates of the system [69]. Since the mobility of the Li^+ is a key issue also in the Li-Mg-N-H system, it is highly interesting to examine the addition of $Li_xTi_yO_z$. Therefore, potassium-modified $Li_xTi_yO_z$ additives are synthesized and their effect on the microstructural and hydrogen storage properties of $Mg(NH_2)_2$+2LiH system is studied for the first time. Successful formation of this mixed phase had to be proven first by X-ray diffraction (SR-PXD). SR-PXD provided a hint about the presence of stable $Li_xTi_yO_z$ compounds. Nevertheless, the composition of the additives were not clear yet. Therefore, X-ray absorption spectroscopy near edge structure (XANES) technique is applied in order to investigate the oxidation state of Ti. The nature of the formed additives upon ball milling are observed and analysed with transmission electron microscopy (TEM). Possible formation of Li-Ti-O and K-Ti-O nanoparticles are studied with HR-TEM observation. Furthermore, an analysis is carried out on the determination of rate–limiting steps of hydrogen uptake and release reactions.

Another approach to improve the hydrogen properties of amide–hydride systems is to stabilize the dehydrogenation product [70]. In this respect, the addition of $LiBH_4$ to the amide-hydride composite is beneficial on the one hand, since it improves the reaction kinetics. On the other hand, it reduces the reaction enthalpy [52], [71]. Thermodynamic tuning is the consequence of the stabilization of the dehydrogenation product, $LiNH_2$ [70] through the formation of compounds with known high ionic conductivity, i.e. $Li_4(BH_4)(NH_2)_3$ or/and $Li_2(BH_4)(NH_2)$. These compounds appear to also support the diffusion of Li^+ in the system. Additional work is required to shed more light on the sorption properties and reaction mechanism of this system. Of particular interest is to investigate the effect of $LiBH_4$ additive amount on the $6Mg(NH_2)_2$+9LiH system. In order to gain more information on the kinetic properties and cycling behaviours of this composite, thorough studies are carried out with samples contain varying amount of $LiBH_4$. Activation energies of the first and second dehydrogenation reactions are calculated using the Kissinger method. Furthermore, the determination of rate–limiting steps of hydrogen uptake and release is carried out.

The last part of the thesis is devoted to the study of the influence of bimetallic amide on the kinetic properties of $Mg(NH_2)_2$+2LiH. Recently, bimetallic amide–hydride systems $K_2Mn(NH_2)_4$+8LiH and $K_2Zn(NH_2)_4$+8LiH with ultrafast hydrogen uptake features are reported by Cao *et al.* [72]–[74]. The use of bimetallic amides as additives on amide-hydride systems has not been investigated so far. The aim of this investigation is to elucidate the reaction mechanism, phase evolution and sorption properties of the $Mg(NH_2)_2$+2LiH system containing $K_2Mn(NH_2)_4$. In this respect, the evolution of the crystalline phases is characterized via *in-situ* SR-PXD. The apparent activation energy of the dehydrogenation reaction is calculated with Kissinger method. In order to gain a deeper understanding of the kinetic barriers in this system, a correlation between the material kinetic properties and the calculated rate constants will be attempted.

All in all, the aim of this dissertation is to understand the role of additives on the amide–hydride systems. In this respect, the processes involved in enhanced hydrogen uptake and release reactions are examined systematically to deduct general mechanisms and strategies for designing new high performance amide – hydride systems for hydrogen storage purposes.

2. Experimental

In the following section, an overview of the material preparation methods and characterization techniques used in this thesis work are given.

2.1 Materials and synthesis methods

The materials used, their purity and suppliers are given in Table 2.1.

Table 2.1 − Overview of the materials used in this work and respective purities and suppliers.

Material	Purity (%)	Supplier
MgH_2	95	Rockwood Lithium GmbH
LiH	97	Alfa Aesar
KH	30 wt.% dispersion in mineral oil	Sigma Aldrich
$LiBH_4$	95	Sigma Aldrich
TiO_2 (anatase)	99	Sigma Aldrich
K (cube)	99.5% in mineral oil	Sigma Aldrich
Manganese	99	Sigma Aldrich

Due to their high reactivity against moisture, K in cubes shape and KH in powder form are stored in mineral oil. In order to clean from the mineral oil K, a piece of K-cube is washed in hexane (95 %, anhydrous, Sigma Aldrich) under continuous stirring for a couple of minutes. The slurry of KH in mineral oil, it is firstly washed with hexane. The obtained powder is then dried in the Büchner funnel under vacuum to remove hexane residues. The removed oil is collected inside of the Büchner flask, while the volatile solvent is collected in a solvent trap cooled down with liquid nitrogen. The whole filtration/washing process take place inside of a MBraun glovebox under continuously purified argon atmosphere (O_2 and H_2O levels lower than 1 ppm). Solvent trap setup was prepared by Dr. Antonio Santoru, I carried out washing and drying processes.

2.1.1 Additive synthesis

2.1.1.1 Synthesis of $Mg(NH_2)_2$

$Mg(NH_2)_2$ is synthesized in-house *via* a two-step process. Firstly, MgH_2 is ball milled at a speed of 400 rpm with ball to powder ratio of 30:1 under 7 bar of NH_3 for 24 hours. All mechanochemical milling procedures reported in this thesis are performed with a Fritsch P6 planetary ball-milling device, using high pressure stainless steel milling vials (Evico Magnetics GmbH) and milling balls. Each 6 hours, the gas in the milling vial is released and fresh NH_3 is introduced. All milling procedures and material handling in this work are carried out in a dedicated glove box under a continuously purified argon flow (O_2 and H_2O levels lower than 1 ppm). Secondly, the collected sample is annealed for 48 hours at 310 °C under 7 bar of NH_3 in a high pressure vessel (20 ml from Parr Instrument Company) to optimize the yield of $Mg(NH_2)_2$. The purity of the obtained $Mg(NH_2)_2$, determined with thermogravimetric analysis (TG), is 95%.

2.1.1.2 Synthesis of $K_2Mn(NH_2)_4$

$K_2Mn(NH_2)_4$ is synthesized by ball milling K-cubes and manganese powder in a molar ratio of 2:1 with a ball to powder ratio 10:1 for 12 h with a speed of 100 rpm under an atmosphere of 7 bar of NH_3.

2.1.1.3 Synthesis of $Li_xTi_yO_z$ and K-modified $Li_xTi_yO_z$

Additives composed of LiH, anatase TiO_2 and KH are milled in different stoichiometric ratios under argon atmosphere for two hours. Stoichiometric compositions for the synthesis of LTO and K-modified LTO additives are: 1) $0.5LiH+TiO_2$ and 2) $0.5LiH+TiO_2+0.25KH$, respectively. Following, the obtained powder batches are annealed at 600°C under argon atmosphere for 8 hours.

2.1.2 Sample preparation

For the $Mg(NH_2)_2+2LiH+x$K-modified $Li_xTi_yO_z$ system, $Mg(NH_2)_2$ is mixed with LiH and 1.0, 2.5 or 5 mol. % of LTO or K-modified LTO additives (Section 2.1.1.3). All materials are milled in a Fritsch P6 Planetary ball miller for 5 hours with ball to powder ratio of 60:1 under 50 bar of H_2 pressure, using stainless steels balls and stainless steel high pressure milling vial from

Evico GmbH [75]. The sample names used to identify the prepared specimens are listed in Table 2.2.

Table 2.2 − Compositions and designations for the $Mg(NH_2)_2$+2LiH+*x*K-modified $Li_xTi_yO_z$ system

Sample composition	Sample code
$Mg(NH_2)_2$ + 2LiH	Mg-Li
$Mg(NH_2)_2$ + 2LiH + 0.05(0.5LiH+TiO_2)	Mg-Li-5LTO
$Mg(NH_2)_2$ + 2LiH + 0.05(0.5LiH+TiO_2+0.25KH)	Mg-Li-5LTOK
$Mg(NH_2)_2$ + 2LiH + 0.025(0.5LiH+TiO_2+0.25KH)	Mg-Li-2.5LTOK
$Mg(NH_2)_2$ + 2LiH + 0.010(0.5LiH+TiO_2+0.25KH)	Mg-Li-1LTOK
$Mg(NH_2)_2$ + 2LiH + 0.05KH	Mg-Li-5K

For the $6Mg(NH_2)_2$+9LiH+*x*$LiBH_4$ system, $Mg(NH_2)_2$ is mixed with LiH and $LiBH_4$ in the molar ratios 6:9:0, 6:9:0.5, 6:9:1 and 6:9:2 for 36 hours under 50 bar of H_2 with ball to powder ratio 60:1, using the above mentioned high pressure vial. For the sake of clarity, the samples are named as shown in Table 2.3.

Table 2.3 − Compositions and designations for the $6Mg(NH_2)_2$+9LiH+*x*$LiBH_4$ system

Sample composition	Sample code
$6Mg(NH_2)_2$ + 9LiH	Mg-Li
$6Mg(NH_2)_2$ + 9LiH + 0.5$LiBH_4$	Mg-Li-0.5$LiBH_4$
$6Mg(NH_2)_2$ + 9LiH + $LiBH_4$	Mg-Li-1$LiBH_4$
$6Mg(NH_2)_2$ + 9LiH + 2$LiBH_4$	Mg-Li-2$LiBH_4$

For the $Mg(NH_2)_2$+2LiH+*x*$K_2Mn(NH_2)_4$ system, $Mg(NH_2)_2$ is mixed with LiH and $K_2Mn(NH_2)_4$ in the molar ratios 1:2:0, 1:2:0.01, 1:2:0.05 and 1:2:0.35 for 36 hours under 50 bar of H_2 with ball to powder ratio 60:1. In addition to these four samples, three additional samples containing KH are prepared for comparison purposes. Sample compositions and designations are listed in Table 2.4. Multiple de/rehydrogenation cycles (25 cycle) of Mg–Li and Mg–Li–5KMN samples are performed in a high-pressure stainless steel autoclave from

Estanit GmbH. The stainless steel specimen holder, which has six inlets, enables to simultaneously cycle several specimens under equal experimental conditions. However, due to the presence of specimens with different compositions, it is not possible to determine the gravimetric hydrogen capacities of each specimen. Powders of Mg–Li and Mg–Li–5KMN specimens are placed inside these inlets (~ 400 mg each) inside and Ar-filled glovebox (O_2 and H_2O levels lower than 1 ppm). De/rehydrogenation reactions are carried out under isothermal conditions at 180℃, with pressures of 1 bar (dehydrogenation time: 20 hours) and 80 bar of H_2 (rehydrogenation time: 4 hours), respectively.

Table 2.4 − Compositions and designations for the $Mg(NH_2)_2$+2LiH+$x$$K_2Mn(NH_2)_4$ system

Sample composition	Sample code
$Mg(NH_2)_2$ + 2LiH	Mg-Li
$Mg(NH_2)_2$ + 2LiH + 0.01$K_2Mn(NH_2)_4$	Mg-Li-1KMN
$Mg(NH_2)_2$ + 2LiH + 0.05$K_2Mn(NH_2)_4$	Mg-Li-5KMN
$Mg(NH_2)_2$ + 2LiH + 0.35$K_2Mn(NH_2)_4$	Mg-Li-35KMN
$Mg(NH_2)_2$ + 2LiH + 0.07KH	Mg-Li-7KH
$Mg(NH_2)_2$ + 2LiH + 0.15KH	Mg-Li-15KH
$Mg(NH_2)_2$ + 2LiH + 0.30KH	Mg-Li-30KH

2.2 Characterization techniques

The characterization of the prepared materials is carried out using several different techniques, which are explained in the following paragraphs. General information about the experimental conditions is provided herein, whereas details related to the each specific set of experiment are provided at the corresponding figure captions.

2.2.1 Volumetric analyses

Volumetric differential pressure method is used for the determination of hydrogen storage properties of 6$Mg(NH_2)_2$+9LiH+$x$$LiBH_4$ and $Mg(NH_2)_2$+2LiH+$x$$K_2Mn(NH_2)_4$ systems. An in-house made Sieverts apparatus, which operates in the pressure range of 10^{-2}-100 bar and in temperature range of RT-500℃, is utilized for this purpose. Hydrogen release and uptake amounts are determined by measuring the differential pressure change between the sample holder and the empty reference holder. About 100 mg of sample are loaded into the sample holder in an Ar-filled glovebox (O_2 and H_2O levels lower than 1 ppm).

Regarding the $Mg(NH_2)_2$+2LiH+$Li_xTi_yO_z$ system, the hydrogenation kinetics and gravimetric capacities are assessed using another Sieverts apparatus (HERA Hydrogen Storage Systems, Longueil, QC, Canada) based on the differential pressure technique, which is described above. The hydrogen gas used in the experiments has a purity of 99.999% (5.0 H_2). The mass of sample utilized for each measurement is approximately 100 mg.

In order to assess the rate-limiting steps of the dehydrogenation processes, Sharp and Jones method is used [76], [77]. In this method, experimental data are expressed as following:

$$F(\alpha) = A\left(\frac{t}{t_{0.5}}\right), \tag{2.1}$$

where A is the rate constant, $t_{0.5}$ is the time at the reaction fraction α = 0.5. The fraction (α) is taken as the hydrogen capacity over the maximum reached capacity for each sample. By implementing different rate equations, several plots of $(\frac{t}{t_{0.5}})_{\text{theoretical}}$ versus $(\frac{t}{t_{0.5}})_{\text{experimental}}$ are obtained. In this work, we applied this model to the portion of dehydrogenation curve between 0.1 and 0.8 fraction of the overall hydrogen capacity. We implemented 11 different rate equations as listed in Table 2.5. The best fitting reaction rate model must obey the following rules; slope of the fitted line should be ~ 1, intercept ~ 0 and R^2 ~ 1.

Table 2.5 − Fitted rate equations

Kinetic rate models	**Rate equations to be used for Sharp and Jones Method**
D1 one-dimensional diffusion	$\frac{\alpha^2}{0.25}$
D2 two-dimensional diffusion	$\frac{\alpha + ((1-\alpha) * \ln(1-\alpha))}{0.1534}$
D3 Jander eq. for three dimensional diffusion	$\frac{(1-(1-\alpha)^{\frac{1}{3}})^2}{0.04255}$
D4 Ginstling-Braunshtein eq. for three dimensional diffusion	$\frac{1-\frac{2}{3}\alpha-(1-\alpha)^{\frac{2}{3}}}{0.0367}$
F1 JMA - n = 1	$\frac{-\ln(1-\alpha)}{0.6931}$
R2 two - dimensional interface controlled	$\frac{1-(1-\alpha)^{\frac{1}{2}}}{0.29289}$
R3 three dimensional interface controlled	$\frac{1-(1-\alpha)^{\frac{1}{3}}}{0.20629}$
F2 JMA - n = ½	$\frac{-\ln(1-\alpha)^{\frac{1}{2}}}{0.832}$
F3 JMA - n = 1/3	$\frac{-\ln(1-\alpha)^{\frac{1}{3}}}{0.8849}$
F4 JMA - n = ¼	$\frac{-\ln(1-\alpha)^{\frac{1}{4}}}{0.9124}$
F5 JMA - n = 2/5	$\frac{-\ln(1-\alpha)^{\frac{2}{5}}}{0.8636}$

2.2.2 Calorimetric analyses

2.2.2.1 Differential thermal analysis with mass spectroscopy

Thermal behaviour and evolved gas analyses during the dehydrogenation reactions are carried out using a Netzsch STA 409 C Differential Thermal Analysis combined with a Hiden Analytical HAL 201 Mass-Spectrometer (DTA-MS). This system is located inside an argon-filled glovebox (H_2O and O_2 levels below 1 ppm). About 2 mg of sample is placed in an Al_2O_3 crucible and it is heated up to desired temperature in DTA. Measurements are done under 50 ml/min Ar flow. The evolved gas mixture is simultaneously transported to the MS device. For DTA measurements, higher sample amount (10 mg) is used to obtain better signal to noise ratio.

2.2.2.2 Differential scanning calorimetry

Differential scanning calorimetry (DSC) measurements are performed in a Netzsch DSC 204 HP calorimeter located inside an argon-filled glovebox (H_2O and O_2 levels below 1 ppm). About 5 mg of each sample is placed in an Al_2O_3 crucible and then heated from room temperature to 300 °C with a heating rate of 3 °C/min. All de/rehydrogenation experiments are performed under 1 bar and 80 bar of H_2 backpressure, respectively. Before starting the measurement, the residual argon gas in the DSC chamber is evacuated. Then the DSC measuring chamber is flushed with 10 bar of H_2 for three times. During heating up and cooling down, a magnetic mass flow-meter is used to maintain the set pressure with a tolerance of ± 0.2 bar.

In order to calculate apparent activation energies (E_a), many methods have been developed so far [78]–[80]. In this work, the effect of additives on the kinetic behaviour of solid-gas reactions is calculated via Kissinger method, applying calorimetry [79]. This method is suitable for the samples that exhibit multi-step reactions and it allows us to determine E_a of a reaction process without assuming a kinetic model, i.e. without determining the rate limiting step of the reaction. The E_a calculation is shown in equation 2.2;

$$ln(\beta/T_m^2) = ln(AR/E_a) - \frac{E_a}{RT_m} \quad (2.2)$$

, where A is the pre-exponential factor and R is the gas constant. The temperature for the maximum reaction rate (T_m) is obtained from DSC curves measured at heating rates (β) of

1°C/min, 3°C/min, 5°C/min and 10°C/min under 1 bar of H_2 backpressure. Then, $ln\left(\frac{\beta}{T_m^2}\right)$ against $1/T_m$ is plotted, E_a and A is calculated from linear fitting.

2.2.3 Infrared spectroscopy

Characterization of the amorphous phases are carried out with Fourier Transform Infrared Spectroscopy (FT-IR). Measurements are performed, using an Agilent Technologies Cary 630 FT-IR located in an argon filled glove box (H_2O and O_2 levels below 1 ppm). Each measurement is acquired in the transmission mode in spectral range of 650 cm^{-1} - 4000 cm^{-1} with a resolution of 4 cm^{-1}.

2.2.4 X-ray diffraction

2.2.4.1 Laboratory X-ray diffraction (PXD)

Ex-situ investigations about the compositions in the samples are done by powder X-ray diffraction method (PXD) using a Bruker D8 Discover diffractometer equipped with Cu X-ray source (λ = 1.54184 Å) operating at 50 kV and 1000 mA and a 2D VANTEC detector, in Bragg-Brentano geometry. Diffraction patterns are collected in the angular range of 2θ range from 10° to 80° with a step size $\Delta 2\theta = 10°$. Exposure time is 400 seconds for each step. For the phase identification the ICSD database is used [81]. A sample holder sealed with a poly(methyl methacrylate) (PMMA) dome is utilized to prevent the sample oxidation during PXD measurements.

2.2.4.2 *In-situ* synchrotron X-ray powder diffraction (SR-PXD)

SR-PXD experiments related to the $Mg(NH_2)_2$+2LiH+$K_2Mn(NH_2)_4$ system are performed at MAX II Synchrotron facility in Lund, Sweden, beamline I711 [82]. The diffraction patterns are acquired in Debye–Scherrer geometry. The used X-ray wavelength is λ = 0.9941 Å. The diffraction images are collected using a 2D Agilent Titan detector (2048 x 2048 pixel, each of size 60 x 60 mm^2) placed at about 80 mm from the sample holder. The exact sample to detector distance and the instrumental function are obtained performing the Rietveld refinement (using the MAUD program) of the diffraction pattern of a LaB_6 standard specimen [83], [84]. The specimen powder is introduced into a sapphire capillary inside an Ar-filled glove box (O_2 and H_2O levels lower than 10 ppm) and then fixed into an in-house developed *in-situ* cell [85], which allows controlling the heating temperatures and operating gas pressures [86]. The first

dehydrogenations are recorded in the temperature range between RT and 180°C, with a heating rate of 5°C min^{-1} under 1 bar of H_2. Following this experiment, the rehydrogenation processes are recorded heating the material from RT to 180 °C under 80 bar of H_2 (heating ramp of 5°C min^{-1}). The 2D images are integrated using the FIT2D software and quantitative analysis are performed via Rietveld method using the MAUD software [83], [84], [87].

SR-PXD experiment related to the $Mg(NH_2)_2$+2LiH+$Li_xTi_yO_z$ system is performed at Deutsches Elektronen-Synchrotron (DESY) P02.1 powder diffraction and total scattering beamline. The beamline is equipped with A Perkin Elmer XRD1621 2D detector. The used X-ray wavelength is $\lambda \approx 0.2071$. Mg-Li-5LTOK sample is heated from RT to 300°C with a heating rate of 5°C/min. Every 10 seconds a two-dimensional SR-PXD pattern is collected.

2.2.5 X-ray absorption spectroscopy

X-ray absorption spectroscopy near edge structure (XANES) regions of the prepared additives $Li_xTi_yO_z$, K-modified $Li_xTi_yO_z$, TiO_2 anatase (reference), as-milled Mg-Li-5LTO, as-milled Mg-Li-5LTOK, as-milled Mg-Li-2.5LTOK, dehydrogenated Mg-Li-2.5LTOK and rehydrogenated Mg-Li-2.5LTOK samples are carried out at a laboratory X-ray spectrometer Rigaku, R-XAS Looper. The measurements are performed in transmission mode around the Ti K-edge (4966 eV) in the range of energy from 4950 eV to 5030 eV at ambient temperature. The optimum amount of material for the measurements is calculated by the program XAFSMAS (version 2012/04, ALBA synchrotron, Barcelona, Spain) [88]. The samples are prepared by mixing the specimen powders with boron nitride (powder, purity: 98%; Sigma-Aldrich, St. Louis, Missouri, MO, USA,) in a mortar, and then pressing the obtained mixtures into pellets of 10 mm diameter inside a glove box. The pellets are sealed with Kapton tape (50 μm in thickness) to prevent the oxidation/hydrolysis of the samples. The XANES measurements are performed in an in-house device, in the Sunset Group - INIFTA Institute, La Plata, Buenos Aires, Argentina. Dr. Julián Puszkiel assisted me during preparation and I prepared all samples. Dr. José Martin Ramallo-López and Dr. Martin Mizrahi did the measurements and analyses, using the IFEFFIT software (version 1.2.11, University of Chicago, Chicago, IL, USA) package [89].

2.2.6 Transmission electron microscopy

Transmission electron microscopy (HR-TEM) observations, diffraction patterns (DP) and dark field (DF) are done using a Tecnai G2 microscope with an information limit of 0.12 nm and Schottky Emission gun operating at 300 kV. Samples after milling and after hydrogenation-dehydrogenation conditions are observed. All samples are prepared in a glove box under controlled O_2 and H_2O atmosphere (O_2 and H_2O levels lower than 1 ppm) by dispersing the powders in lazy carbon grids. In order to avoid oxidation of the material at the time to introduce the grids into the microscope column, the dispersed powder on the grid is covered with a special polymeric film which does not preclude the electron interactions with the sample. Then HR-TEM observations of the identified zones are done. The TEM measurements are carried out at IFW Dresden, Helmholtzstr. 20, 01069 Dresden, Germany. M. V. Castro Riglos and Dr. Julián Puszkiel did the observation and data analyses. HR-TEM image processing is done with the following programs: Digital Micrograph (License no. 90294175), i-TEM (License no. A2382500, EMSIS GmbH, Münster, Germany).

3. Results

3.1 $Mg(NH_2)_2$+2LiH+K-modified $Li_xTi_yO_z$ system

In this section, the results obtained in the investigation of the properties of the samples listed in Table 2.2 are presented systematically. Thermal behaviour during desorption process of the as-milled samples is studied in combination with the analysis of the evolving gasses. Hydrogen capacities, reaction kinetics as well as cycling stabilities are measured and the phases formed during the desorption reactions are studied *in-situ*. Complementary information about the phases, which are appear to be responsible for the improved kinetic performances, are obtained by the combination of X-ray absorption near edge structure (XANES) and high-resolution transmission electron microscopy (HR-TEM) techniques. The results presented in this section are published in *Scientific Reports*, **10,** 8 (2020) doi:10.1038/s41598-019-55770-y [90].

3.1.1 Compositions of the synthesized additives

Details regarding the additive synthesis were presented in section 2.1.1.3. Initial structural analysis on the composition of the additives after synthesis is done by Rietveld refinement of the corresponding powder X-ray diffraction (PXD) patterns. Results acquired after milling and annealing, indicate that LTO additive (initial composition: $0.5LiH+TiO_2$) is composed of the single phase $LiTi_2O_4$ (Figure 3.1-A). The constituents of potassium modified LTO additive (initial composition: $0.5LiH+TiO_2+0.25KH$), after the synthesis are 10 wt.% $K_{1.04}O_{16}Ti_8$, 17 wt.% $LiTi_2O_4$, 27 wt.% $LiTiO_2$ and 46 wt.% $K_2O_{17}Ti_8$ (Figure 3.1-B).

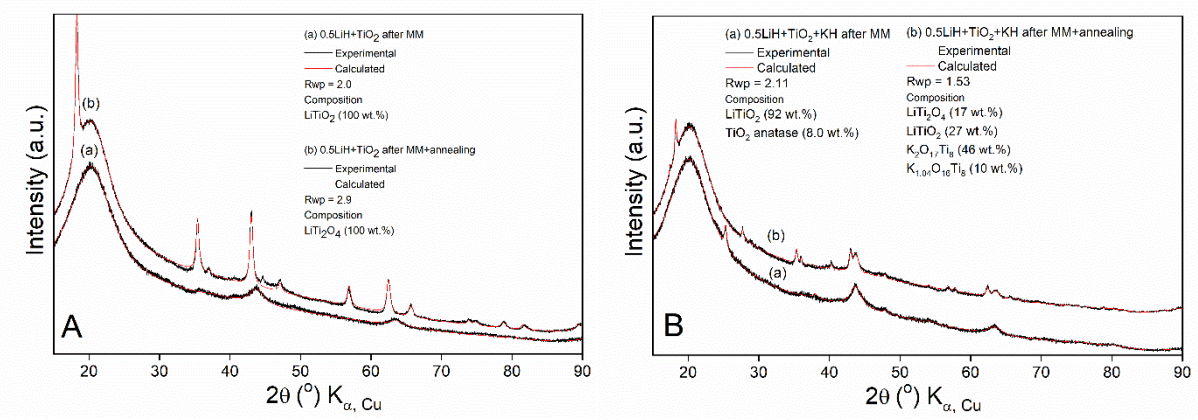

Figure 3.1 A Powder X-ray diffraction (PXD) of $0.5LiH+TiO_2$ **(a)** after milling, **(b)** after milling and annealing **B** PXD of $0.5LiH+TiO_2+0.25KH$, **(a)** after milling **(b)** after milling and annealing. Figure readopted from [90].

3.1.2 Thermal analysis - mass spectroscopy

Thermal and evolving gas analysis of the samples containing LTO or the K-modified LTO additive is presented in Figure 3.2-A. The differential thermal analysis (DTA) curve of the additive-free sample, Mg-Li, exhibits two overlapping endothermic events between 170°C and 230°C. These two events are due to desorption reactions in accordance with reactions 1.6 and 1.7. Desorption peak temperature is at 205°C. The LTO additive containing sample, Mg-Li-5LTO, shows a desorption trend similar to that of Mg-Li. The presence of the LTO additive does not lead to improvement neither of the onset nor of the peak temperatures. Accordingly, also the MS analyses of the gases (H_2 and NH_3) evolving from the two samples upon heat treatment are almost identical (Figure 3.2-B and Figure 3.2-C). However, the sample containing the K-modified additive, Mg-Li-5LTOK, shows reduction about 30°C of the desorption onset temperature and 20°C of the peak maxima of the main thermal event. Moreover, the ammonia release between 180°C and 220°C is minimized.

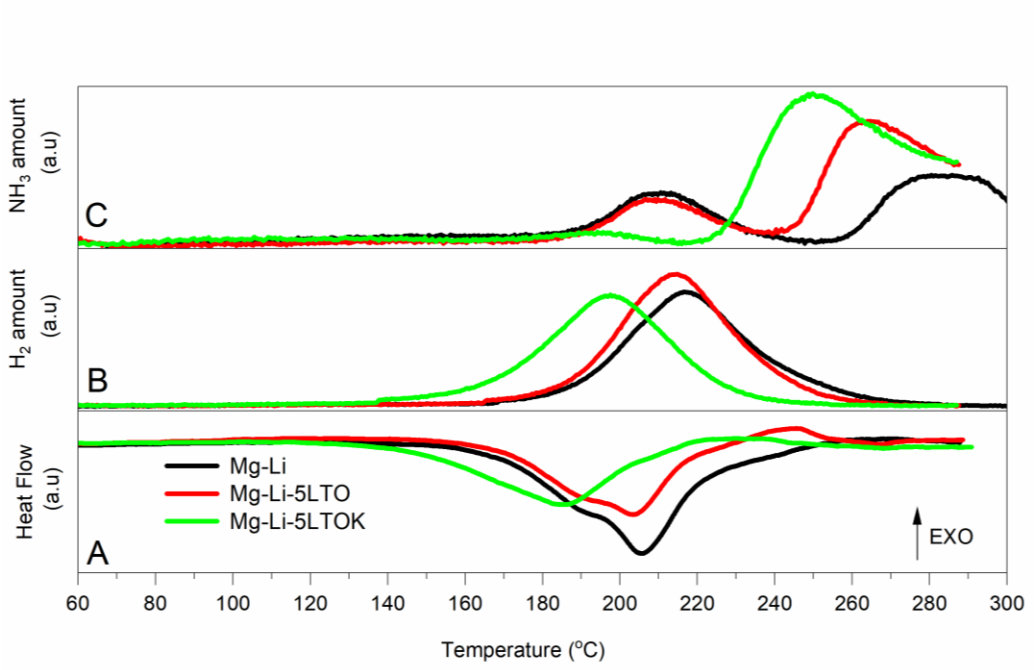

Figure 3.2 A DTA, **B** and **C** MS traces of as-milled samples measured in the temperature range of 60°C − 300°C with a heating ramp of 3°C/min and 50 ml/min Ar flow. Figure readopted from [90].

3.1.3 *In-situ* synchrotron powder X-ray diffraction characterization

The advantages of using the K-modified LTO additive with respect to the LTO additive are illustrated by the thermal analysis reported in Figure 3.2. In order to understand the processes

taking place upon desorption of the sample containing K-modified LTO (Mg-Li-5LTOK), the evolution of the crystalline phases are studied by *in-situ* SR-PXD (Figure 3.3). The SR-PXD pattern acquired at room temperature reveals that it is not possible to assign any potassium-containing phases from the observed Bragg reflections. This implies that potassium-containing phases are either in amorphous or extremely fine-crystalline state. Existing peaks are ascribable to the presence of the LTO additive ($LiTi_2O_4$). However, due to the broadness of the observed diffraction peaks, we cannot exclude the presence of several phases having a general formula $Li_xTi_yO_4$ ($0.75 \leq x \leq 1$, $1.9 \leq y \leq 2$). This fact suggests that the additive´s composition changes upon milling. The presence of reflections belonging to $Li_2Mg(NH)_2$ (orthorhombic phase) at around 170°C indicates that desorption reaction has already started, which is in good agreement with DTA analysis (Figure 3.2-A). Formation of the cubic $Li_2Mg(NH)_2$ takes place at the temperatures higher than 220°C. This transition is expected since the phase transformation of $Li_2MgN(H)_2$ from the orthorhombic to the cubic structure occurs over 200°C [91].

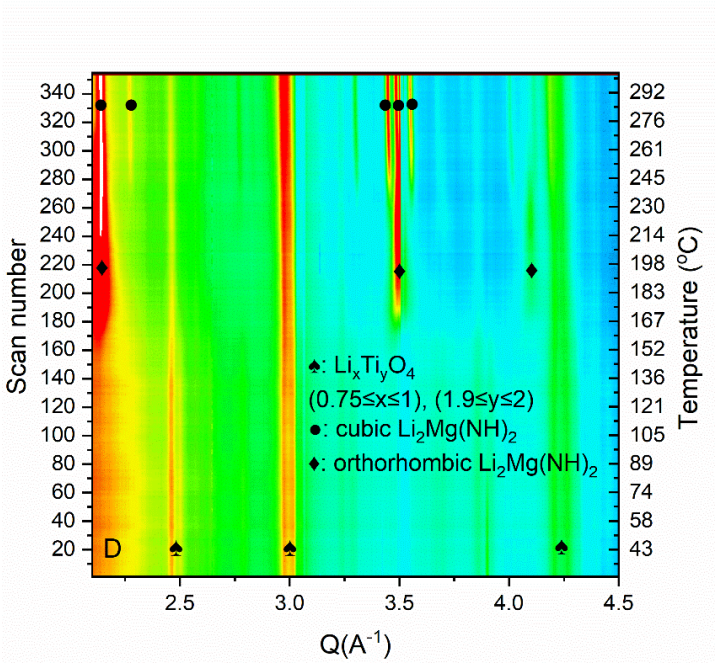

Figure 3.3 *In-situ* SR-PXD data of the Mg-Li-5LTOK sample, which is heated from room temperature to 300°C with a heating ramp of 5°C/min under 1 bar of argon pressure. Measurement is performed at Deutsches Elektronen-Synchrotron (DESY) in the P02.1 beamline (λ= 0.207 Å). Figure readopted from [90].

3.1.4 Volumetric analyses

First desorption kinetics of as-milled samples are presented in Figure 3.4-A. Desorption of Mg-Li starts at 180°C and 4.5 wt.% of gas is released within 120 minutes. Mg-Li-5LTO sample displays a similar behaviour as Mg-Li, though with a reduced capacity to 2.3 wt.% due to the presence of additive. Modification of the additive with potassium (Mg-Li-5LTOK, Mg-Li-

2.5LTOK and Mg-Li-1LTOK) leads to a reduction on desorption onset temperature from 180°C to 150°C, which is in agreement with thermal analysis (Figure 3.2-A). This temperature reduction changes to some extent with the amount of the LTOK additive. It is possible to observe in the inset plot of Figure 3.4-A that higher additive amounts lead to slightly lower onset temperatures. Besides that, the decrement of the amount of the LTOK additive lead to an increase in the desorbed gas amount. Mg-Li-5LTOK desorbs 3 wt.%, whereas Mg-Li-2.5LTOK and Mg-Li-1LTOK desorbs 3.8 wt.% and 4.3 wt.%, respectively. In the literature, K-containing additives, especially KH, are known to improve reaction kinetics of $Mg(NH_2)_2$+LiH system [51], [66], [67]. In order to compare our findings with the KH containing system, an additional sample with $Mg(NH_2)_2$+2LiH+0.05KH composition (Mg-Li-5K) is prepared. Despite the fact that the lowest onset temperature (135°C) is obtained for this sample, its reaction rate is slower in comparison with the samples containing K-modified additive.

Reabsorption kinetics of Mg-Li and Mg-Li-LTO are sluggish and require more than 10 hours to reach full capacity (Figure 3.4-B). On the contrary, samples containing K-modified LTO absorb H_2 notably faster (Mg-Li-5LTOK within 1 hour, Mg-Li-2.5LTOK within 2.5 hours and Mg-Li-1LTOK within 2 hours). Therefore, the effect of K-modified LTO on Mg-Li is clearly seen both in the absorption and desorption kinetic properties. Despite the fact that Mg-Li-1LTOK has fast H_2 absorption kinetic, H_2 capacity reduces from 4.3 to 3 wt.% after a single cycle. Based on these results, we have chosen the sample Mg-Li-2.5LTOK in order to investigate the material properties upon cycling (section 3.1.5).

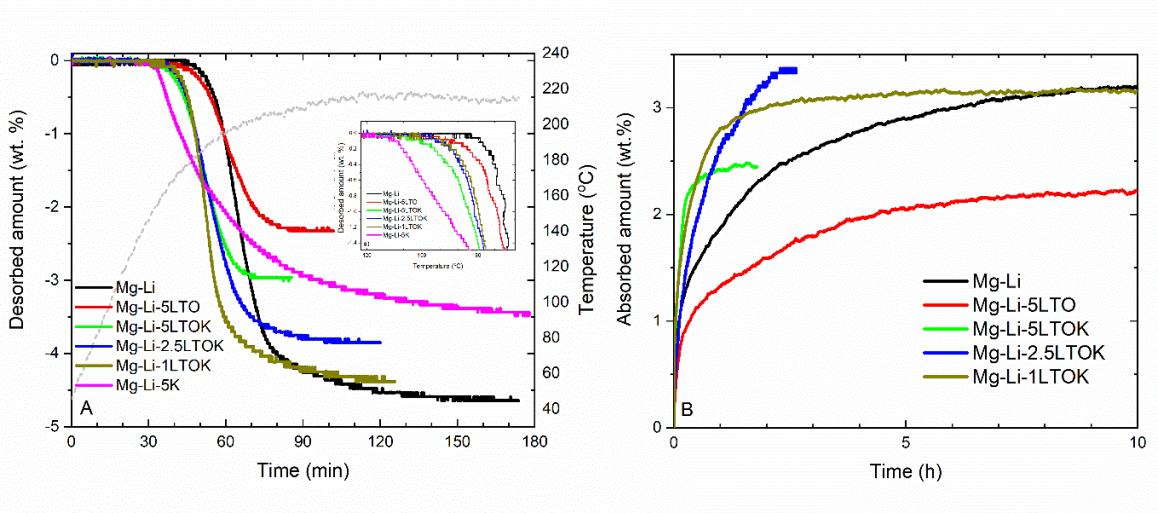

Figure 3.4 A 1st Desorption kinetics of as-milled samples (RT→ 220 °C under 1 bar of H_2, 3°C/min heating rate) **B** Reabsorption kinetics at 180°C (isothermal) and 80 bar of H_2 pressure. Figure readopted from [90].

3.1.5 Cycling stability

In Figure 3.4, it was presented that Mg-Li-2.5LTOK possesses the best hydrogen storage properties among the investigated materials, i.e. reduced desorption temperature, fast reabsorption kinetics, the highest H_2 storage capacity (about 3.5 wt.%) and reversibility. Hence, this subsection presents its cycling stability comparison with the additive-free sample, Mg-Li. Figure 3.5 shows the cycling stability upon 5 absorption/desorption cycles for Mg-Li and Mg-Li-2.5LTOK samples. During cycling, both desorption and absorption kinetics of Mg-Li-2.5LTOK are faster than those of Mg-Li, 2 and 5 times, respectively. In addition, the hydrogen storage capacity of Mg-Li is reduced by a half, from 3.4 to 1.7 wt.%, after 5 cycles. On the other side, it reduces only 10%, from 3.1 to 2.75 wt.% in the case of Mg-Li-2.5LTOK sample. In Figure 3.5-B it is possible to observe that the chosen measurement time of 12 hours is not enough for achieving the complete absorption in the Mg-Li sample, whereas Mg-Li-2.5LTOK reaches nearly complete absorption in the same time frame.

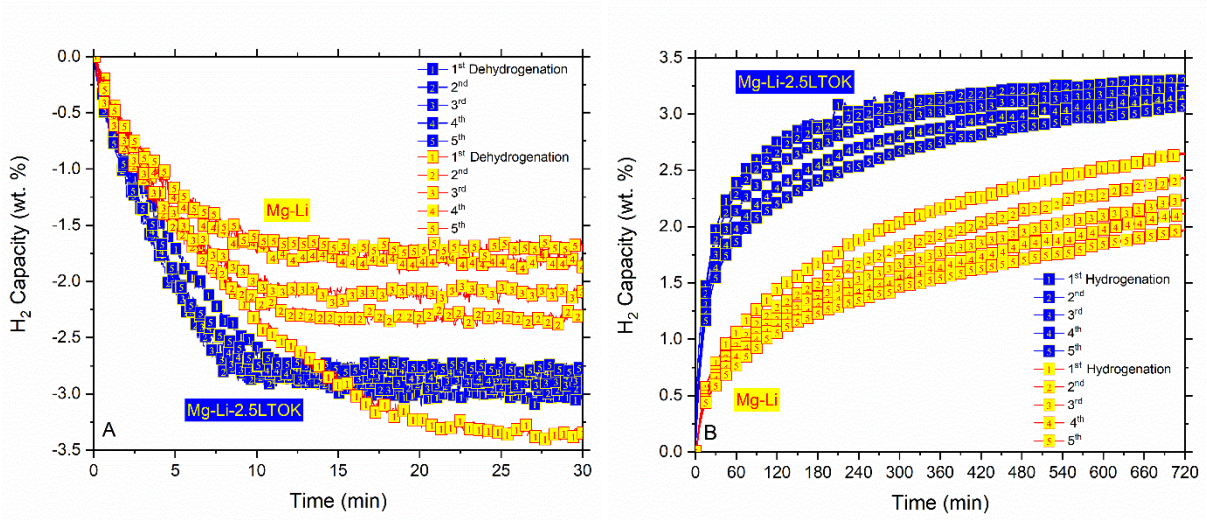

Figure 3.5 Reaction kinetics of Mg-Li and Mg-Li-2.5LTOK within the first 5 H_2 absorption/desorption cycles, **A** Isothermal desorption at 180°C and 1 bar of H_2 pressure **B** Isothermal absorption at 180°C and 80 bar of H_2. Figure readopted from [90].

3.1.6 Initial structural analysis

First overview to the structural analysis is done with PXD and FT-IR techniques (Figure 3.6 A-D and E-H, respectively). PXD patterns of the samples after ball milling (Figure 3.6-A) exhibit broad peaks with low intensity, which can be attributed to the harsh milling conditions. As-milled Mg-Li contains cubic LiH structure with *Fm3m(225)* space group and a broad peak at 2θ=30°, which corresponds to the tetragonal $Mg(NH_2)_2$ structure with $I4_1/acd(142)$ space group. Since $Mg(NH_2)_2$ is amorphous after intense ball milling, it can be hardly observed in PXD [92]. In contrast, it is more visible on the FT-IR pattern (Figure 3.6-E), where N-H stretching vibrations of $Mg(NH_2)_2$ are positioned at 3268 and 3324 cm^{-1} . When Mg-Li is half desorbed, $LiNH_2$ can be detected at 3257 and 3310 cm^{-1} (Figure 3.6-F). Fully desorbed sample contains small bumps at 3240 and 3197 cm^{-1}, which correspond to IR signals from MgNH (Figure 3.6-G) [93]. $LiNH_2$ and MgNH products from the desorption of the sample should have a solid-solid reaction to form a ternary imide: $Li_2Mg(NH)_2$ [94]. PXD reflections coming from the cubic $Li_2Mg(NH)_2$ phase with *iba2(45)* space group are found in the half and fully desorbed samples (Figure 3.6 B-C). This imide is also observed by FT-IR at 3170 cm^{-1} (Figure 3.6 F-G). Absorption of the desorbed Mg-Li at 180°C leads to recrystallization of $Mg(NH_2)_2$ (Figure 3.6-D).

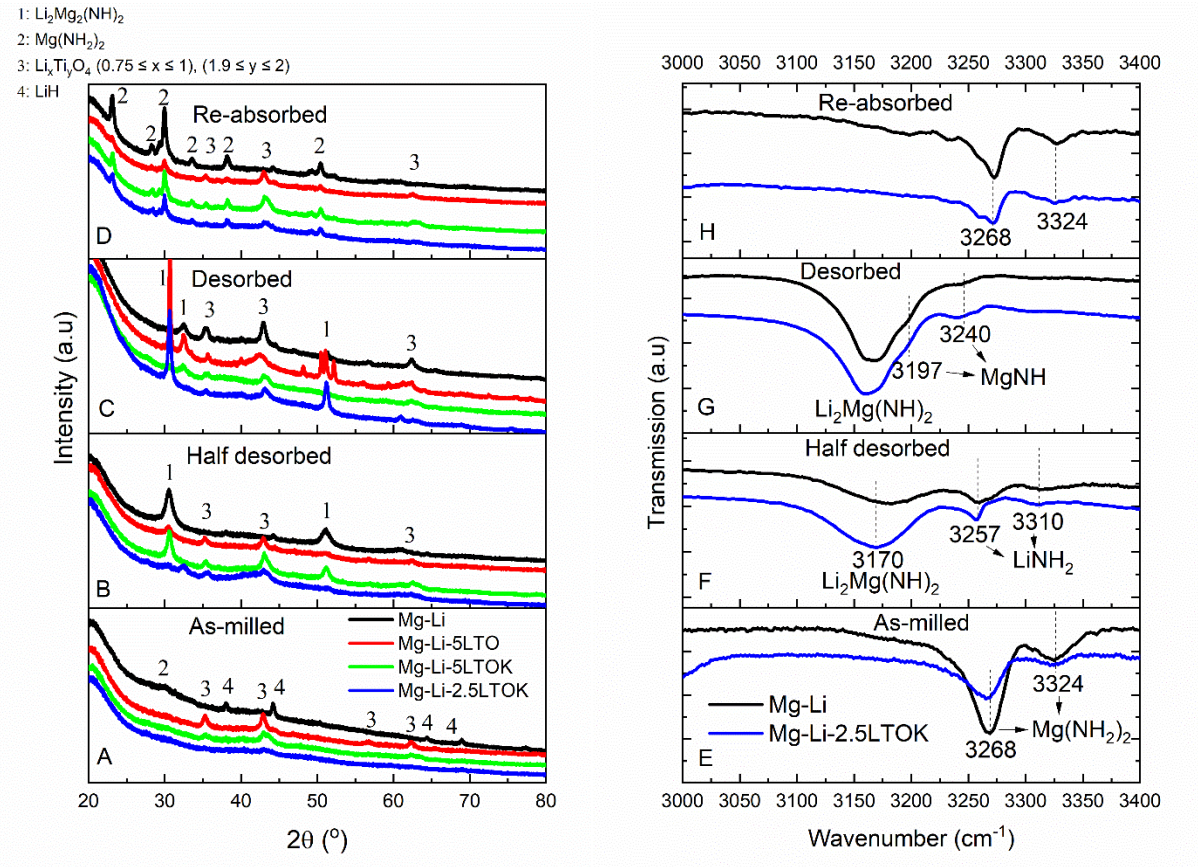

Figure 3.6 A-D PXD plots of samples at different reaction states. **E-H** Corresponding FT-IR plots of samples Mg-Li and Mg-Li-2.5LTOK. Desorption and absorption reactions are performed under 1 bar of H_2 at 210°C and 80 bar of H_2 pressure at 180°C, respectively. Figure readopted from [90].

Regarding the additives, PXD analyses (Figure 3.6 A-D) reveal that in all cases $Li_xTi_yO_4$ compounds with $0.75 \leq x \leq 1$ and $1.9 \leq y \leq 2$ are present. In the ICSD database, it is possible to find several crystal structures belonging to $Li_xTi_yO_4$ that fit well with all reflections [81]. These formed phases are stable and their peaks positions do not change within desorption/absorption processes. The compositions of the as-synthesized additives were already presented in section 3.1.1. However, it is observed that further mechanical milling of these additives with $Mg(NH_2)_2$ and LiH leads to some changes in the additives´ composition, which will be later discussed in section 4.

3.1.7 Apparent activation energies and rate constants

In order to evaluate the effect of the modified additives on desorption apparent activation energy (E_a), the Kissinger method [79] is applied for the first and second desorption reactions of the Mg-Li, Mg-Li-5LTO, Mg-Li-5LTOK and Mg-Li-2.5LTOK samples. For the calculations of the E_a, the peak maximum of the main thermal event (Appendix Figure A1-A4)

is considered. Figure 3.7-A and Figure 3.7-B show the Kissinger plots and obtained values of E_a and A. It is possible to see that the first desorption reaction of Mg-Li has an activation energy of 183±7 kJ·mol^{-1}H$_2$ (Figure 3.7-A). The presence of additive lowers the E_a to 170±3 kJ·mol^{-1}H$_2$ and 173±2 kJ·mol^{-1}H$_2$, as well as the frequency factor (A), for Mg-Li-5LTO and Mg-Li-5LTOK, respectively. On the contrary, E_a value rises to 211±1 kJ·mol^{-1}H$_2$ for the sample Mg-Li-2.5LTOK. It is worthy to note that the frequency factor of this sample is considerably higher (A=1.2x10^{19} s^{-1}) compared to the ones of the Mg-Li, Mg-Li-5LTO and Mg-Li-5LTOK samples.

The E_a values calculated for the second desorption reactions (Figure 3.7-B), increase in comparison with the first desorption, except for Mg-Li-2.5LTOK, which decreases by nearly 15 kJ·mol^{-1}. Moreover, the E_a values for Mg-Li, Mg-Li-5LTO and Mg-Li-2.5LTOK overlap. However, the frequency factor for Mg-Li-2.5LTOK is higher than the ones for Mg-Li and Mg-Li-5LTO. The highest values of E_a and A are measured for Mg-Li-5LTOK. It is also noticed that K-containing additives reduce desorption temperature both in the first and second desorption.

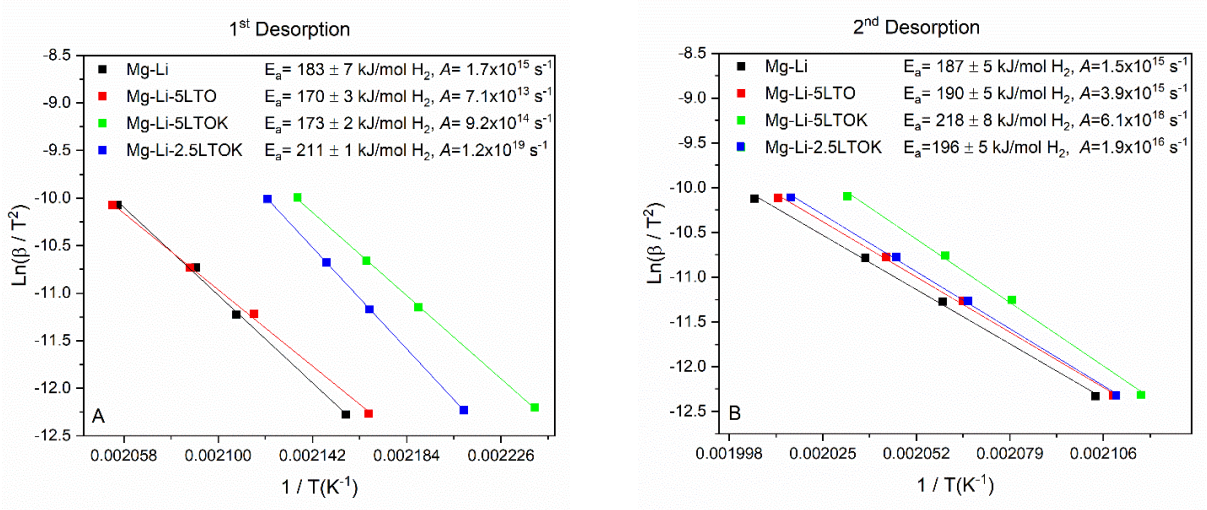

Figure 3.7 Kissinger plots of samples: **A** 1st desorption, **B** 2nd desorption derived from DSC curves at different heating rates (1, 3, 5 and 10 ºC/min) for the calculation of the E$_a$. Figure readopted from [90].

In terms of the observed improved kinetic behaviour (Figure 3.5), and the calculated desorption E_a for the first and second desorption reactions (Figure 3.7), I found contradictory results. On one hand, the Mg-Li-2.5LTOK sample clearly shows reduced onset temperature upon the first desorption and faster kinetics in comparison to the Mg-Li sample. On the other hand, the activation energy values are higher than the one of the material without additive, Mg-Li (Figure 3.7). In order to shed light onto this fact, the kinetic constant (k) is calculated by the Arrhenius expression k = A·exp[-E_a/RT] (1/s) at 180 ºC, which is the cycling temperature

(Figure 3.8). Then, to take into account the effect of the capacity of each sample, *k* is multiplied by the capacity after reabsorption taken from Figure 3.4-B, which can be considered as the more realistic value. As seen in Figure 3.8, the first and second desorption reaction rates for the samples containing LTOK additive are faster than the ones for the Mg-Li and Mg-Li-5LTO samples. However, the activation energies for LTOK containing samples are similar or higher. This behaviour can be mainly attributed to an increase in the frequency factor, which hints towards a possible more efficient contact of the reactants at the interface.

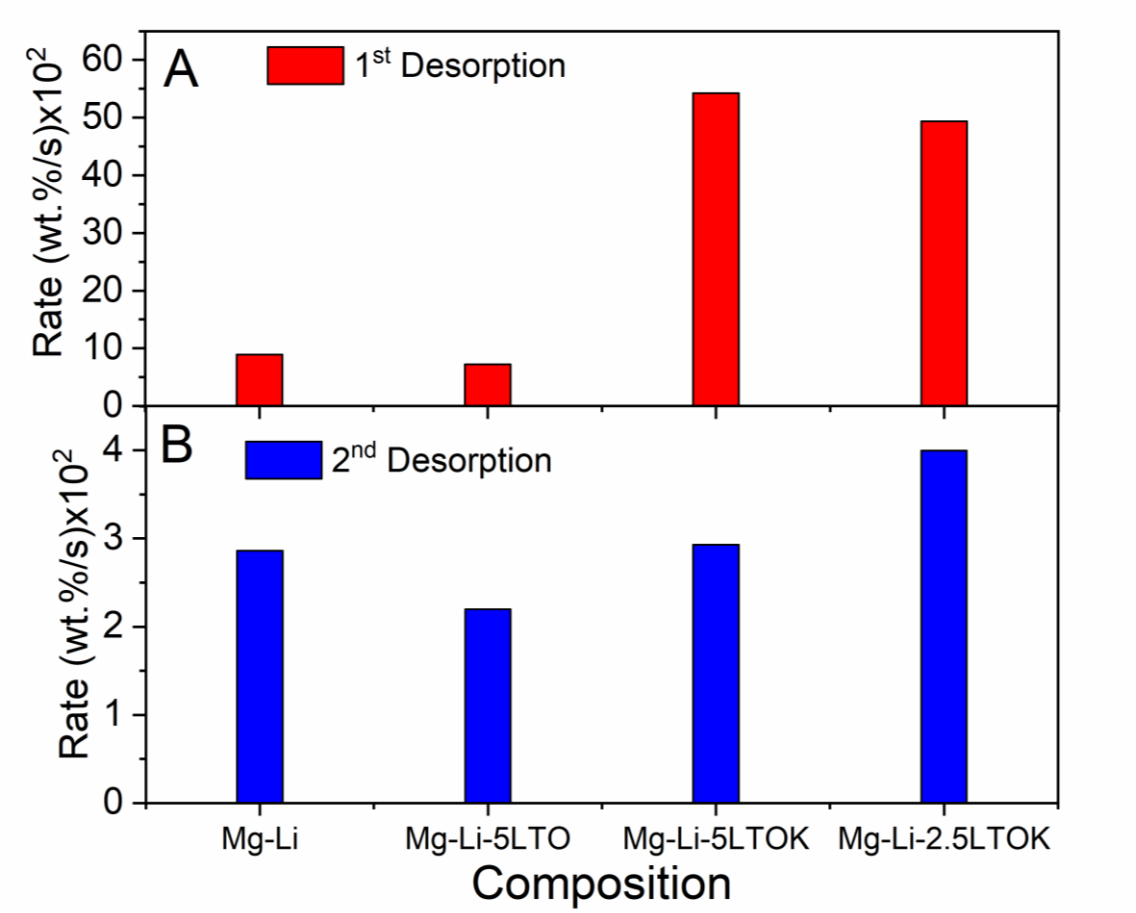

Figure 3.8 Reaction rate for the first and second desorption processes for the investigated samples. Figure readopted from [90].

3.1.8 X-ray absorption spectroscopy analysis

As we reported in section 3.1.3, the composition of the additive after milling with $Mg(NH_2)_2$ and LiH changes. SR-PXD analyses of the Mg-Li-5LTOK sample (Figure 3.3) provide a hint about the presence of stable $Li_xTi_yO_4$ compounds ($0.75 \leq x \leq 1$ and $1.9 \leq y \leq 2$). Nevertheless, compositions of the LTO and LTOK additives after milling with $Mg(NH_2)_2$ and LiH are not clear yet. Therefore, in order to investigate the oxidation state of Ti, X-ray absorption spectroscopy near edge structure (XANES) technique is applied. The changes in the oxidation

state of Ti are determined by the shift of the absorption edges of the samples. The results are compared with the measured XANES spectra of TiO_2 and $LiTi_2O_4$ reference materials.

In Figure 3.9, the spectra of the Mg-Li-2.5LTOK after milling, desorption and reabsorption are compared. It is possible to observe that desorption/absorption does not alter the spectra, thus the nature of the additive LTOK does not change upon hydrogen interaction.

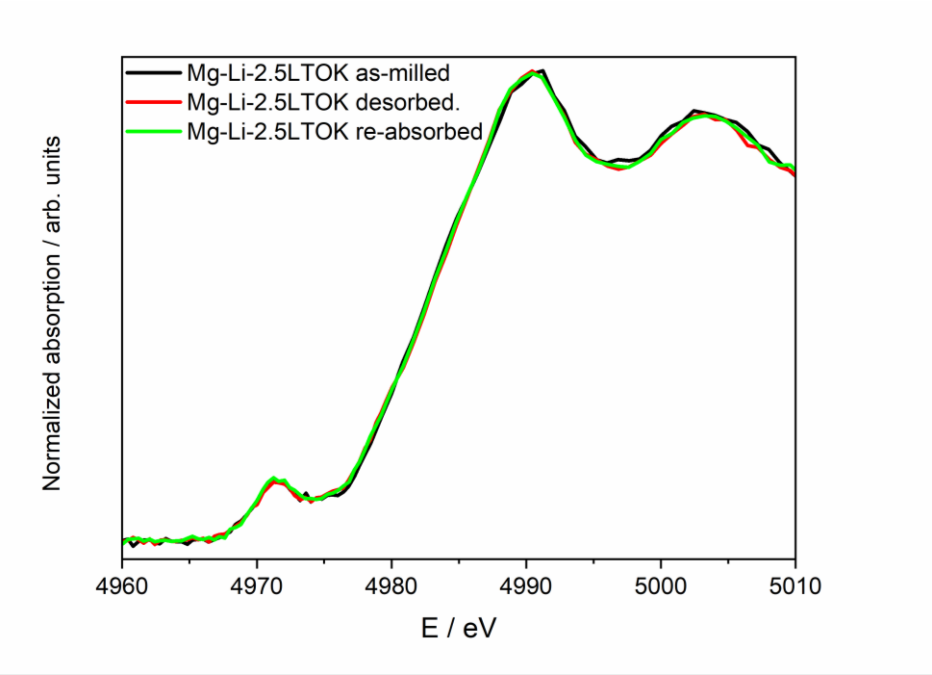

Figure 3.9 XANES spectra at the Ti K-edge of Mg-Li-2.5LTOK after milling (black line), after dehydrogenation (red line) and after rehydrogenation (green line). Figure readopted from [90].

Besides that, oxidation state of Ti in both additives LTO (Figure 3.1-A, $LiTi_2O_4$: 100 %) and LTOK (Figure 3.1-B, 10 wt.% $K_{1.04}O_{16}Ti_8$, 17 wt.% of $LiTi_2O_4$, 27 wt.% $LiTiO_2$ and 46 wt.% $K_2O_{17}Ti_8$) is the same (Figure 3.10). Durmeyer *et al.* already reported that Ti in $LiTi_2O_4$ has an effective valence state of +3.5 [95]. This implies that the effective oxidation state of Ti in the LTOK additive is also +3.5.

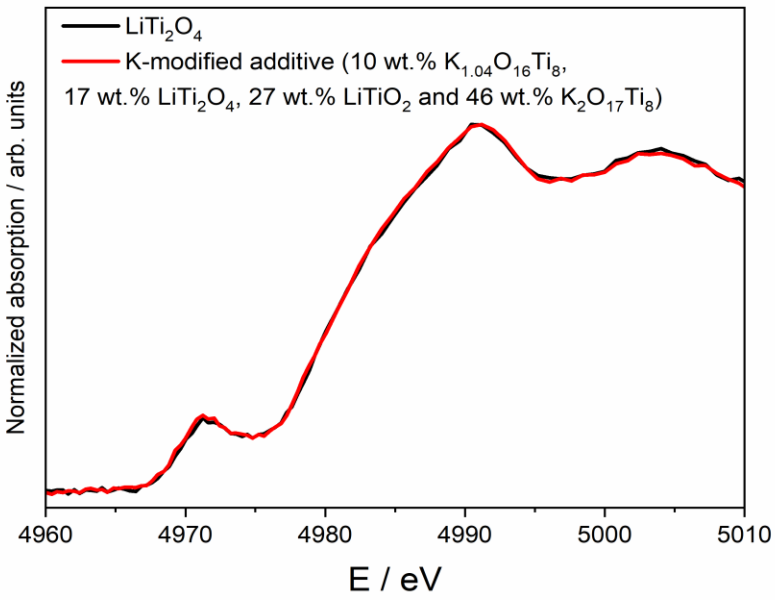

Figure 3.10 XANES spectra at the Ti K-edge of $LiTi_2O_4$ (black line) and K-modified additive (red line). Figure readopted from [90].

Comparing the XANES spectra of the as-milled Mg-Li-5LTO, the LTO additive and anatase TiO_2 (Figure 3.11-A), it is possible to observe a change in the position of the absorption edge. The absorption edge of the Mg-Li-5LTO is higher than the one of LTO additive and lower than the one of TiO_2. Hence, this indicates that the valence state of Ti atoms in Mg-Li-5LTO is, on average, higher than +3.5 and lower than +4. A similar behaviour is observed for the Mg-Li-5LTOK sample, with a slight shift toward higher energies on the absorption edge with respect to Mg-Li-5LTO. This fact suggests that a different titanium compound could be formed in the potassium-containing samples. Comparing two samples with different LTOK additive loads (Mg-Li-5LTOK and Mg-Li-2.5LTOK), it is possible to observe that the absorption edge of both samples seems to be similar, showing that the average Ti valence in these samples is also similar (Figure 3.11-B). Then, the results from the Figure 3.11 show that the effective valence state of the Ti atoms in the samples slightly depends on the presence of the K-based additive.

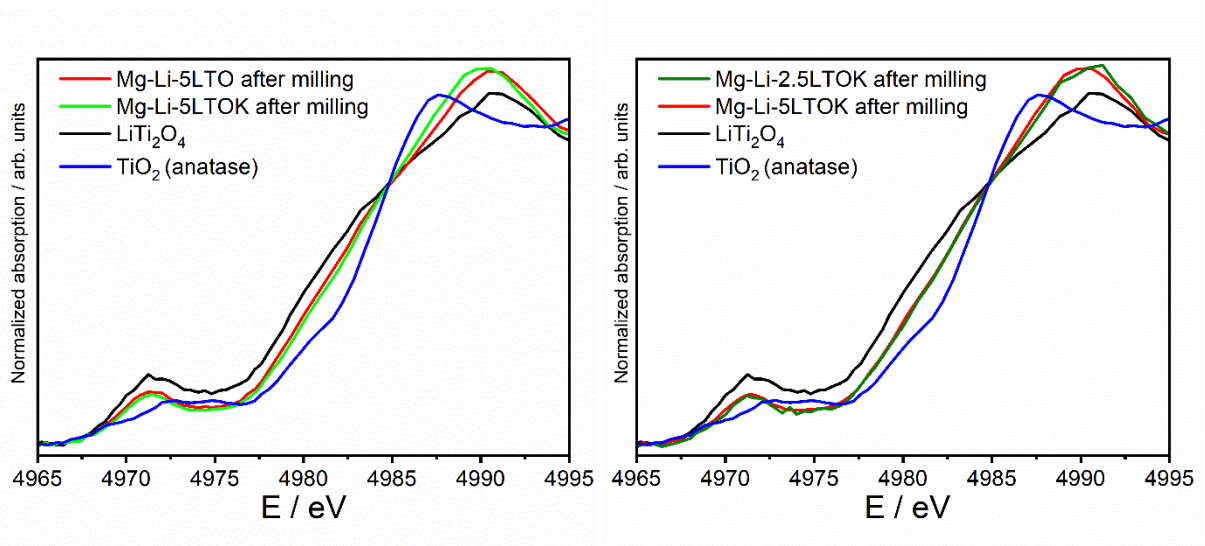

Figure 3.11 XANES curves for: **A** Mg-Li-5LTO and Mg-Li-5LOTK and **B** Mg-Li-2.5LTOK and Mg-Li-5LTOK. $LiTi_2O_4$ and TiO_2 (anatase) are the references. Figure readopted from [90].

Based on the analysis shown above, it is possible to reproduce the Mg-Li-5LTOK spectrum with 76 % of Mg-Li-2.5LTOK and 24 % of LTO additive ($LiTi_2O_4$) as shown in Figure 3.12. Thus, K-modified additive in the Mg-Li-5LTOK sample is composed of 24 % of $LiTi_2O_4$ ($Ti^{+3.5}$) and 76 % of other species, suggesting that the effective Ti valence state is slightly lower than in the Mg-Li-2.5LTOK sample.

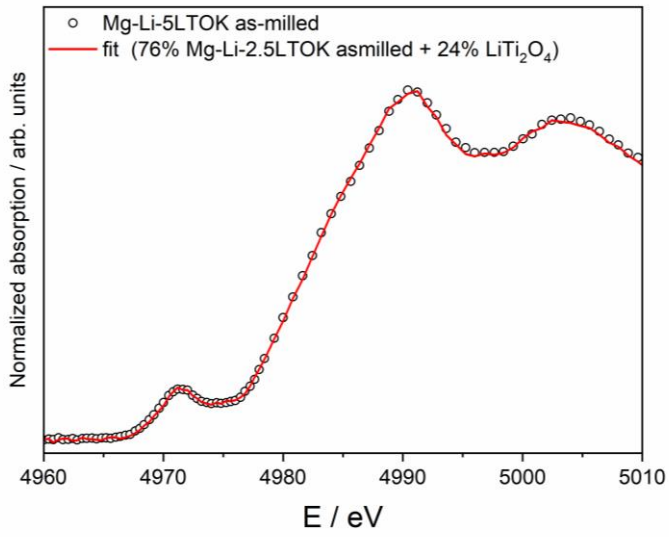

Figure 3.12 Linear combination fit (red line) for the XANES spectrum of Mg-Li-5LTOK (circles). Figure readopted from [90].

3.1.9 Transmission electron microscopy observation

TEM observations and analyses are performed to determine the nature of the additive related compounds formed upon milling. Figure 3.13 shows bright field TEM photos (BF), diffraction patterns (DP) and tables of possible phases based on the DP and dark field images (DF), for the as-milled Mg-Li-5LTO and Mg-Li-2.5LTOK samples. The DP of as-milled samples are taken in the region shown by the BF images. Reflections from the DP are related to the main phase of the material, $Mg(NH_2)_2$ compound. Due to the thickness of the rings, it is not possible to discard some intermediate ($LiNH_2$), product ($Li_2Mg(NH)_2$) and by-product (Li_3N and Mg_3N_2) species. However, these phases are not expected in the as-milled state, unless $Mg(NH_2)_2$ and LiH interacts during the observations promoted by the incident beam. It is also possible to attribute the observed reflections to species composed of Li-Ti-O (Figure 3.13-A) and K-Ti-O (Figure 3.13-B). On one hand, species such as $LiTi_2O_4$ and $Li_{0.07}TiO_2$ are found for the Mg-Li-5LTO sample and on the other hand, species composed of K-Ti-O as well as $LiTi_2O_4$ are present in the Mg-Li-2.5LTOK sample. Dark field images formed from 3rd and 4th rings for Mg-Li-5LTO and from the 3rd ring for Mg-Li-2.5LTOK reveal the presence of small nanoparticles in the range of 5 to 30 nm that can be attributed to the Li-Ti-O and K-Ti-O species.

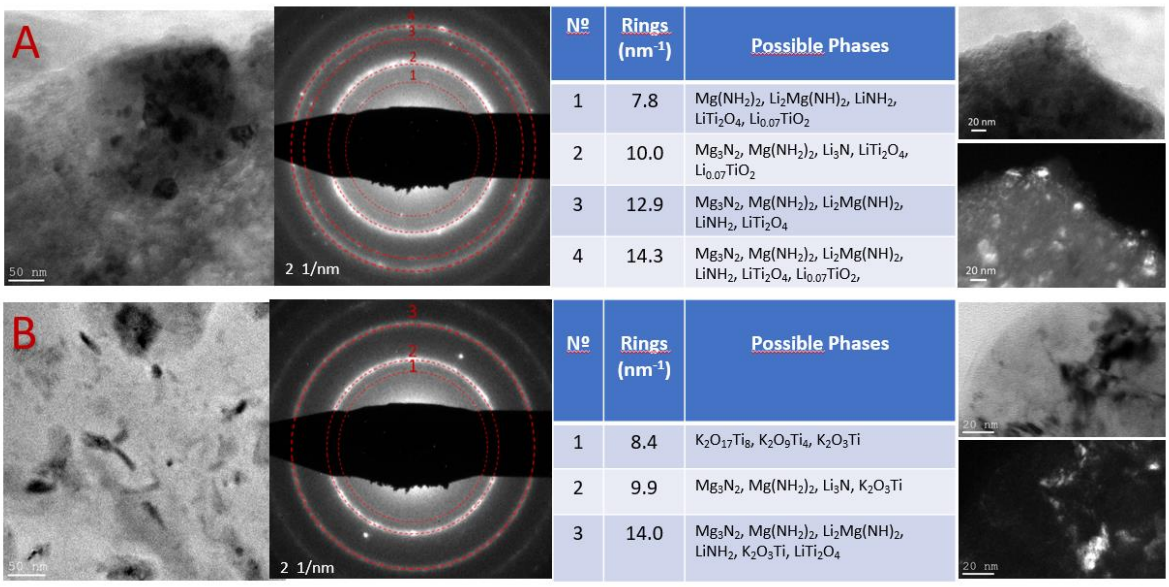

Nº	Rings (nm^{-1})	Possible Phases
1	7.8	$Mg(NH_2)_2$, $Li_2Mg(NH)_2$, $LiNH_2$, $LiTi_2O_4$, $Li_{0.07}TiO_2$
2	10.0	Mg_3N_2, $Mg(NH_2)_2$, Li_3N, $LiTi_2O_4$, $Li_{0.07}TiO_2$
3	12.9	Mg_3N_2, $Mg(NH_2)_2$, $Li_2Mg(NH)_2$, $LiNH_2$, $LiTi_2O_4$
4	14.3	Mg_3N_2, $Mg(NH_2)_2$, $Li_2Mg(NH)_2$, $LiNH_2$, $LiTi_2O_4$, $Li_{0.07}TiO_2$,

Nº	Rings (nm^{-1})	Possible Phases
1	8.4	$K_2O_{17}Ti_8$, $K_2O_9Ti_4$, K_2O_3Ti
2	9.9	Mg_3N_2, $Mg(NH_2)_2$, Li_3N, K_2O_3Ti
3	14.0	Mg_3N_2, $Mg(NH_2)_2$, $Li_2Mg(NH)_2$, $LiNH_2$, K_2O_3Ti, $LiTi_2O_4$

Figure 3.13 TEM bright field photos (BF, left), diffraction patterns (DP, middle), table for possible phases and, BF+DF set of images (right column): **A** Mg-Li-5LTO and **B** Mg-Li-2.5LTOK. Figure readopted from [90].

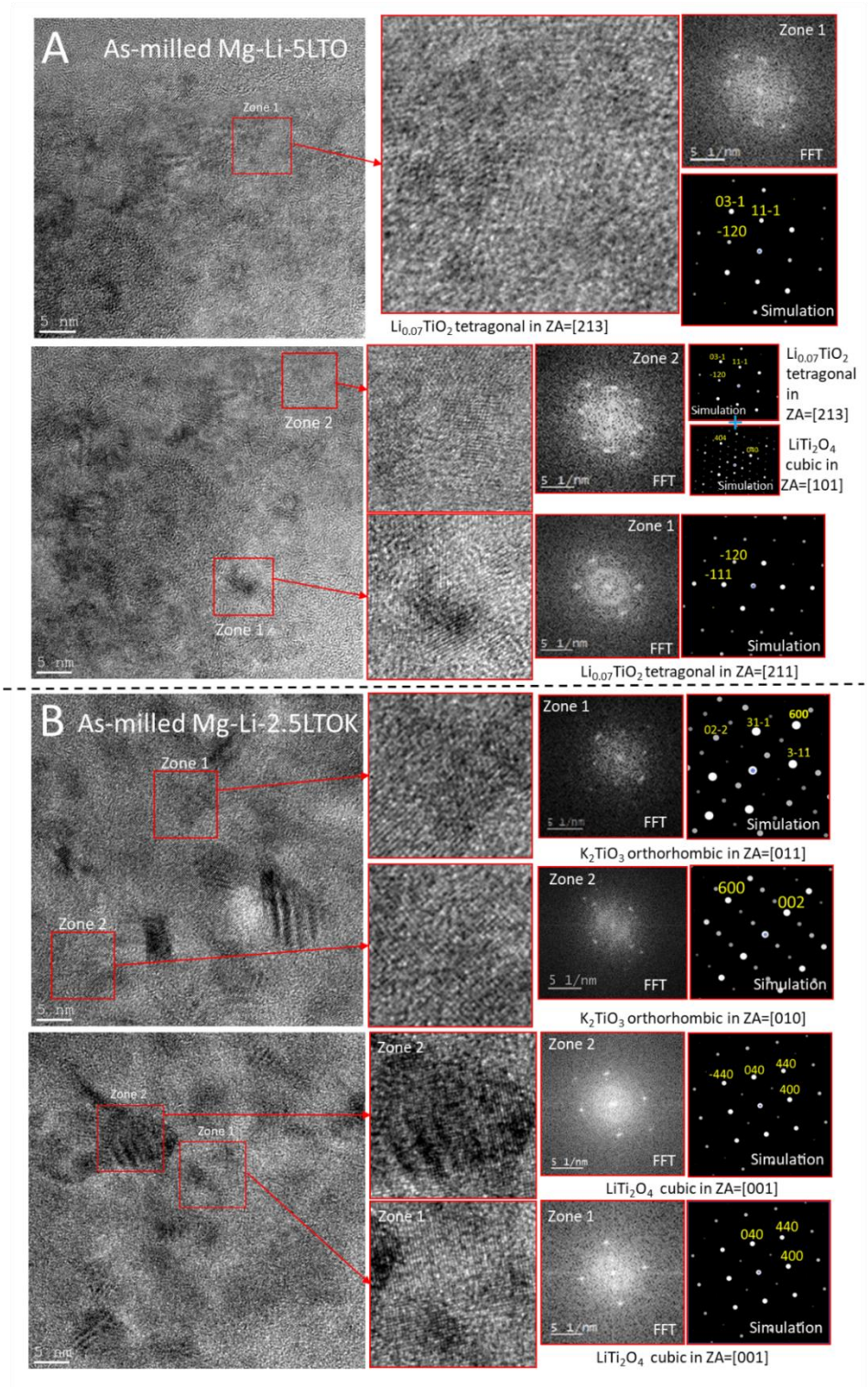

Figure 3.14 Characterization of the nanosized Li-Ti-O and K-Ti-O for **A** as-milled Mg-Li-5LTO and **B** as-milled Mg-Li-2.5LTOK by means of HR-TEM. FFT is calculated in each region and compared to simulated diffraction patterns (DPs) in the adequate orientation. Figure readopted from [90].

In order to verify the formation of such Li-Ti-O and K-Ti-O nanoparticles, HR-TEM observation, fast Fourier transform (FFT) and crystal structure simulation analyses are performed. Figure 3.14 shows the HR-TEM of the as-milled Mg-Li-5LTO and as-milled Mg-

Li-2.5LTOK samples along with its FFTs calculated in each region, and the comparison to simulated diffraction patterns (DPs). In the as-milled Mg-Li-5LTO sample (Figure 3.14-A), the presence of nanoparticles of $Li_{0.07}TiO_2$ (tetragonal) and $LiTi_2O_4$ (cubic) are confirmed by the structure analyses of the HR-TEM photos. For the as-milled Mg-Li-2.5LTOK (Figure 3.14-B), nanoparticles of K_2TiO_3 (orthorhombic) and $LiTi_2O_4$ (cubic) are found. The presence of these nanoparticles leads to an effective oxidation state of Ti between +3.5 and +4 (K_2TiO_3 = +4, $LiTi_2O_4$= +3.5), which is in good agreement with the conclusion drawn from XANES results (section 3.1.7)

3.2 $6Mg(NH_2)_2+9LiH+LiBH_4$ system

In this section, we study several different aspects of the hydrogen storage properties of the $6Mg(NH_2)_2+9LiH+xLiBH_4$ (x = 0, 0.5, 1, 2) system (Table 2.3). The effects of the presence of $LiBH_4$ on the thermal properties, apparent activation energies and especially the reaction kinetics of $6Mg(NH_2)_2+9LiH$ system are studied intensively. Particular emphasis is put on the cycling properties of the system, over 20 de/rehydrogenation cycles. Furthermore, it is herein performed an analysis about the dependence of reaction pathway and rate-limiting step on the amount of $LiBH_4$ present in the system. The results presented in this section are published in the International Journal of Hydrogen Energy, 44(23), 11920-11929, 2019, https://doi.org/10.1016/j.ijhydene.2019.03.133) [57].

3.2.1 Thermal analysis - mass spectroscopy

DSC curves of as-milled samples Mg-Li, Mg-Li-0.5$LiBH_4$, Mg-Li-1$LiBH_4$ and Mg-Li-2$LiBH_4$ are presented in Figure 3.14. Detailed information related to the stoichiometric compositions of prepared samples are given in Table 2.3 . DSC curve of Mg-Li has two overlapping endothermic peaks with maxima at 197℃ and 205℃ ascribed to the two reaction steps described by reactions 1.6 and 1.7. In the samples containing $LiBH_4$, peak maxima are positioned at 191℃ and 180℃ for Mg-Li-0.5$LiBH_4$ and Mg-Li-1$LiBH_4$, respectively. Interestingly, Mg-Li-2$LiBH_4$ sample shows a single dehydrogenation peak at temperature of 176℃, which is nearly 25℃ lower in respect to Mg-Li. The presence of a single peak instead of two peaks is most likely due to a change in the reaction pathway. All $LiBH_4$-containing samples present exothermic broad peaks between 75℃ and 125℃, which most likely are caused by recrystallization of $LiBH_4$ on the $Mg(NH_2)_2$ [96]. Additionally, they have a small endothermic peak at 113℃ (Figure 3.15-B), which is ascribable to the phase transition of $LiBH_4$ from orthorhombic to hexagonal lattice structure [97]. However, this is not always visible as observed in the DSC curve of Mg-Li-1$LiBH_4$. Non-isothermal measurements of the gas evolved during dehydrogenation measured in an Ar flow in the temperature range ~ 20 - 300℃ (Figure 3.16) show that the main released gas is hydrogen. Additionally, small amounts of NH_3 are also released by all the samples beyond 175℃.

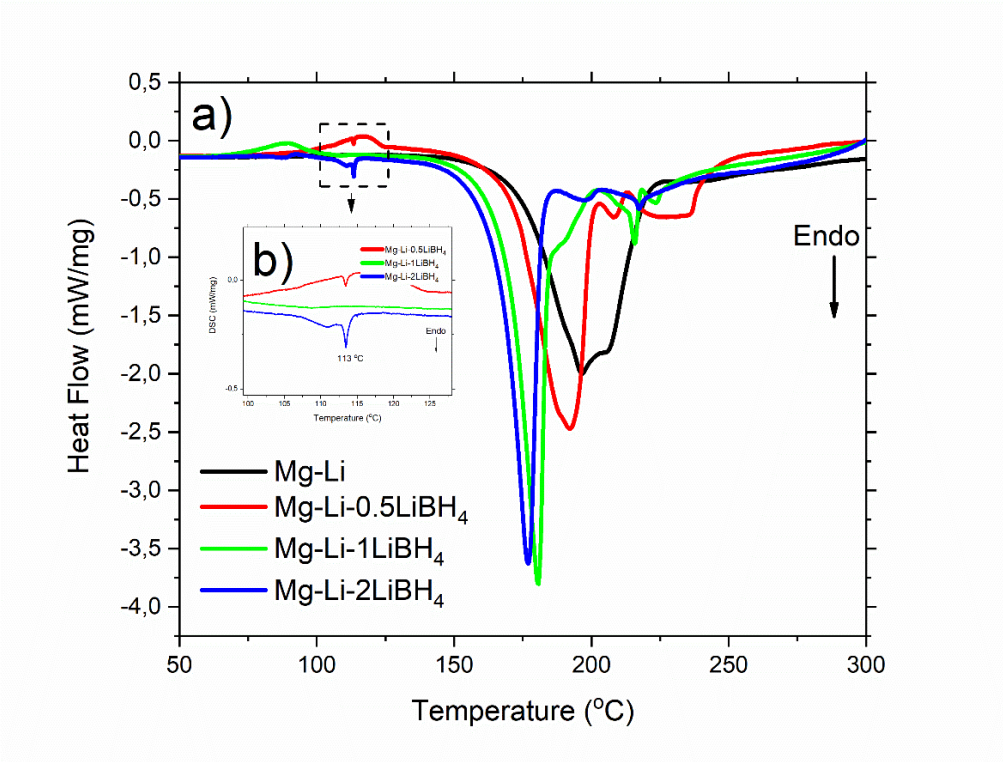

Figure 3.15 **(a)** DSC curves of as-milled samples measured in the temperature range of 20℃ - 300℃ with a heating ramp of 3℃/min and 1 bar of H_2 pressure **(b)** Phase transition of $LiBH_4$. Figure readopted from [57].

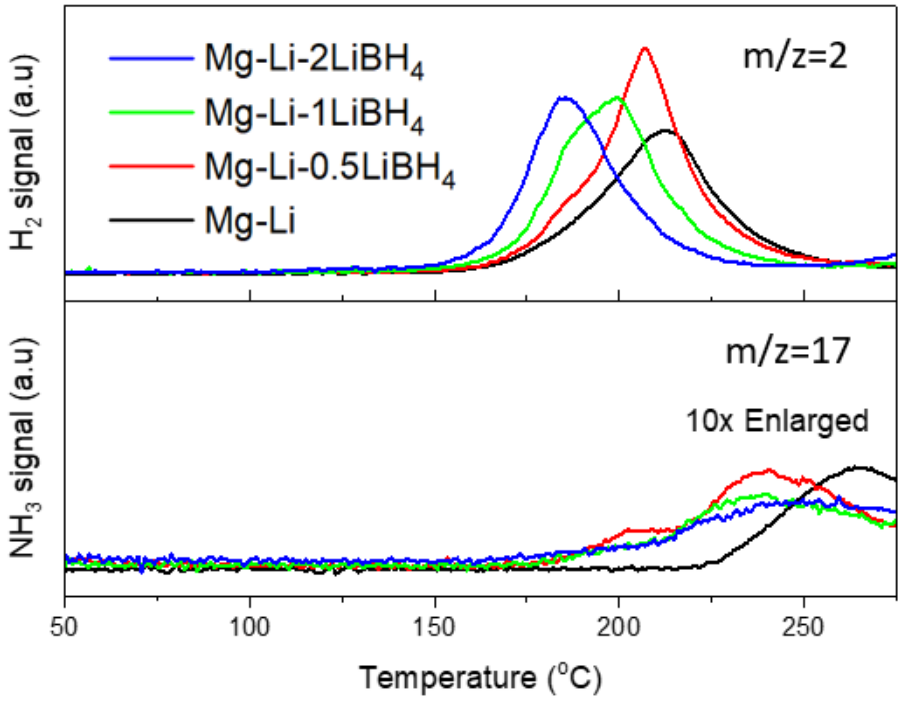

Figure 3.16 Evolved gas analysis of as-milled samples, in the temperature range of 20℃ - 300℃ with a heating ramp of 3℃/min and 50 ml/min Ar flow. Figure readopted from [57].

3.2.2 *Ex-situ* powder X-ray diffraction characterization

In order to identify crystalline phases present in the investigated samples, PXD measurements are performed after 1st dehydrogenation at 180°C, as seen in Figure 3.17. Bragg peaks belonging to $Li_4(BH_4)(NH_2)_3$ are identified in the diffraction patterns of samples Mg-Li-0.5$LiBH_4$, Mg-Li-1$LiBH_4$ and Mg-Li-2$LiBH_4$. The characteristic diffraction peaks of $Li_2Mg_2(NH)_3$ are noted in all samples. In the diffraction pattern of Mg-Li, a broad peak around $2\theta = 51°$ is visible. On the contrary, such a broad peak is not present in the other diffraction patterns. The broad peak observed in the pattern of Mg-Li can be attributed to the presence of $Li_2Mg(NH)_2$. Since the peak is very broad, it might also be attributed to a mixture of $Li_2Mg(NH)_2$ and $Li_2Mg_2(NH)_3$.

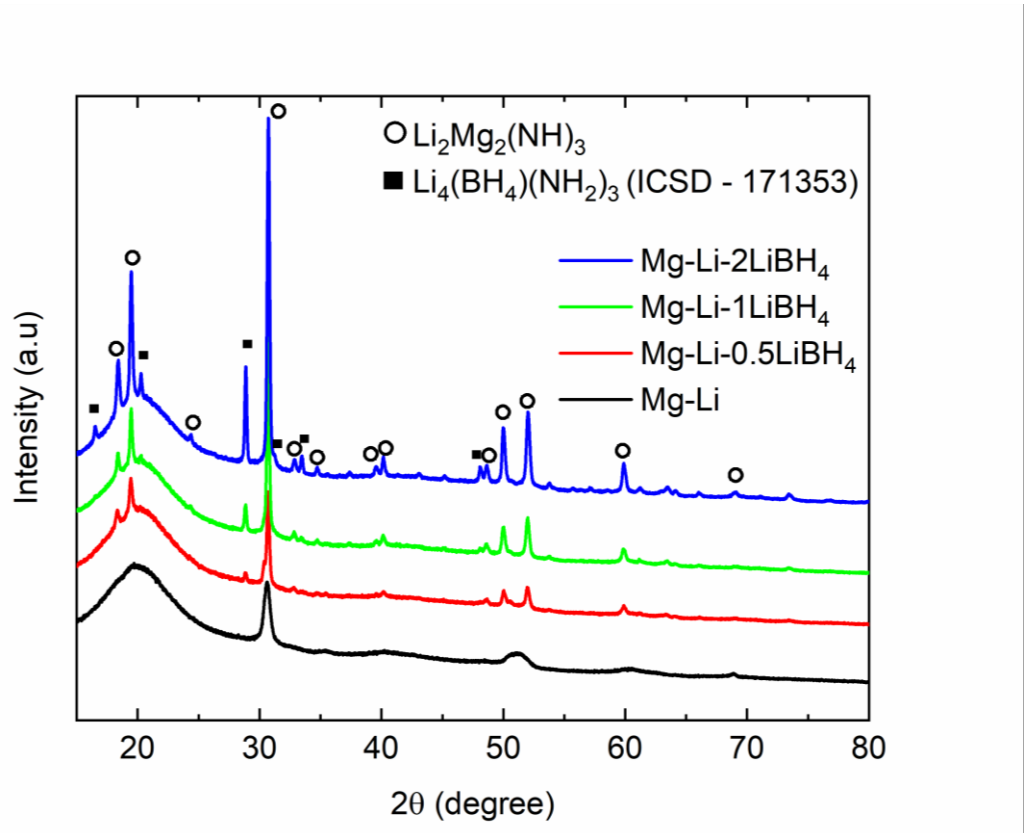

Figure 3.17 PXD patterns of samples after the first dehydrogenation at 180°C and 1 bar of H_2. Figure readopted from [57].

3.2.3 Fourier transform infrared spectroscopy characterization

In order to shed light into the non-crystalline phases present in the investigated samples, the FT-IR measurements are carried out. The FT-IR spectrum acquired for Mg-Li sample shows two different absorption bands at 3257 cm^{-1} and 3310 cm^{-1} (Figure 3.18). These signals are related to the N–H stretching of $LiNH_2$. Interestingly, for sample Mg-Li-0.5$LiBH_4$, in addition to signal of the $LiNH_2$, N–H stretching modes from $Li_4(BH_4)(NH_2)_3$ at wavenumbers 3243 cm^{-}

[1] and 3302 cm^{-1} are also observed. This suggests that the amount of $LiBH_4$ in Mg-Li-0.5$LiBH_4$ is not enough completely react with all $LiNH_2$. When the amount of $LiBH_4$ is further increased, as in the case of Mg-Li-1$LiBH_4$ and Mg-Li-2$LiBH_4$, the typical absorption bands of $LiNH_2$ disappeared. This fact could be attributed to the formation of $Li_4(BH_4)(NH_2)_3$ from the interaction between $LiNH_2$ and $LiBH_4$ during dehydrogenation as previously reported in the literature [96].

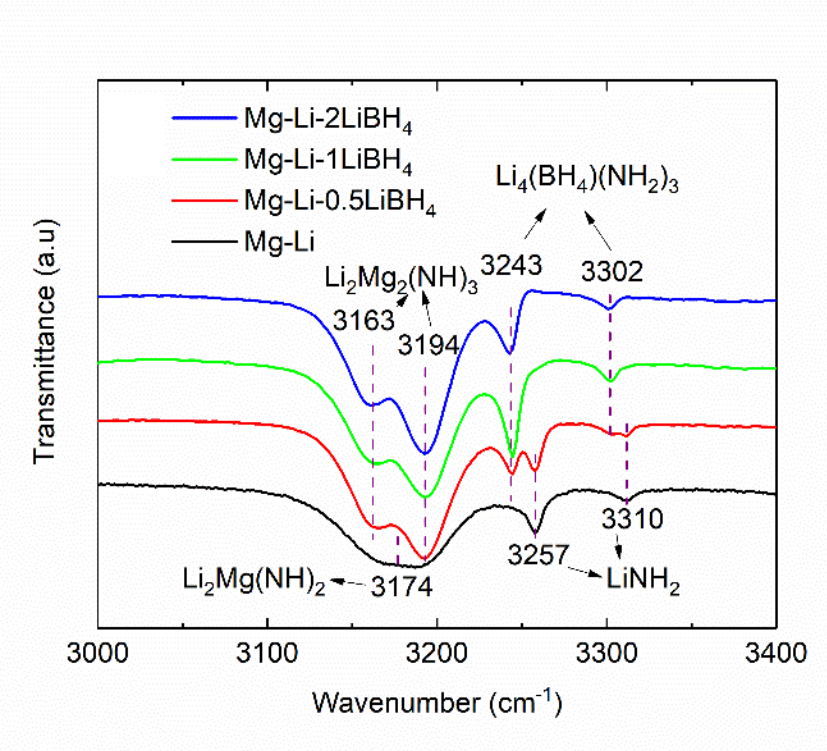

Figure 3.18 FT-IR spectra for samples after the first dehydrogenation at 180°C and 1 bar of H_2. Figure readopted from [57].

3.2.4 Volumetric analyses

The dehydrogenation/hydrogenation curves measured during the 1st cycle for all the samples are presented in Figure 3.19. It is clear that the addition of $LiBH_4$ improves the material kinetic behaviour. In 20 minutes, Mg-Li sample dehydrogenates only ~ 1.1 wt.% of H_2. During the same period, all other samples release more than 3 wt.% of H_2. Improvements in the absorption reaction kinetics are even more significant. Within 10 minutes, Mg-Li-0.5$LiBH_4$, Mg-Li-1$LiBH_4$ and Mg-Li-2$LiBH_4$ samples absorb nearly 3.7 wt.%, 3.6 wt.% and 3.1 wt.% of H_2, respectively. Whereas, Mg-Li sample absorbs only ~ 1.4 wt.% of H_2 during the same time period.

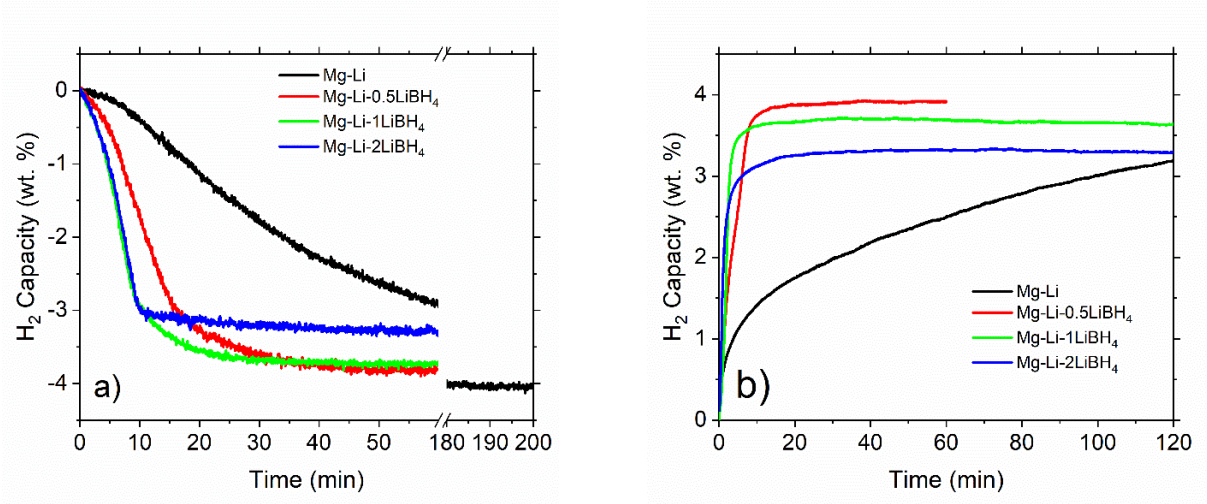

Figure 3.19 (a) 1st isothermal dehydrogenation kinetics of as-milled samples at 180°C and 1 bar of H_2 pressure. **(b)** 1st isothermal hydrogenation kinetics at 180°C and 80 bar of H_2 pressure. Figure readopted from [57].

3.2.5 Cycling stability

Twenty dehydrogenation/hydrogenation cycles are performed for all the as-milled samples isothermally at 180°C. Measured gravimetric H_2 capacities for all the investigated systems over the 20th cycles are reported in Figure 3.20. The amount of desorbed H_2 is reduced from 4.0 wt.% to 3.6 wt.% within 10 cycles for Mg-Li, even if the measurement time is extended. The Mg-Li-0.5$LiBH_4$ sample desorbs ~ 3.9 wt.% of H_2 over 20 cycles. With increasing $LiBH_4$ fraction, total H_2 storage capacities are slightly lower, ~ 3.7 wt.% and 3.5 wt.% for Mg-Li-1$LiBH_4$ and Mg-Li-2$LiBH_4$ samples, respectively. All $LiBH_4$-containing samples exhibit excellent cycling stabilities with no detectable capacity drop as reported in a previous work [70]. In order to compare hydrogenation and dehydrogenation kinetic behaviour upon cycling, for all the studied systems the absorption and desorption times necessary to achieve the 80 % of the hydrogen storage capacity are taken into consideration. The collected results are summarized in Figure 3.21 and original curves are plotted in Figure 3.22. In the first cycle of sample Mg-Li, dehydrogenation and hydrogenation times necessary to achieve 80 % of the maximum capacity are 70 and 63 minutes, respectively. $LiBH_4$ helps significantly to improve the kinetic behaviour, since H_2 desorption and absorption times in the first cycle take just 17 and 6 minutes for Mg-Li-0.5$LiBH_4$ sample, respectively. This values are ~ 4 and ~ 10 times faster than the dehydrogenation and hydrogenation processes of Mg-Li without $LiBH_4$. A further improvement is observed when the amount of additive is increased in the composite. For Mg-Li-1$LiBH_4$ and Mg-Li-2$LiBH_4$ samples, dehydrogenation and hydrogenation times are achieved in about 10 minutes and 3 minutes, respectively. These times increase in the following cycles for all samples except for Mg-Li-2$LiBH_4$, which has the highest amount of additive. An

increase in the H_2 absorption and desorption characteristic times between the 1st and the 19th cycle is only about 1 minute for the Mg-Li-2LiBH$_4$ sample. Therefore, Mg-Li-2LiBH$_4$ has a good potential for application in larger scale thanks to its stable reaction kinetics, excellent cycling stability and gravimetric capacity of about 3.5 wt.% H_2.

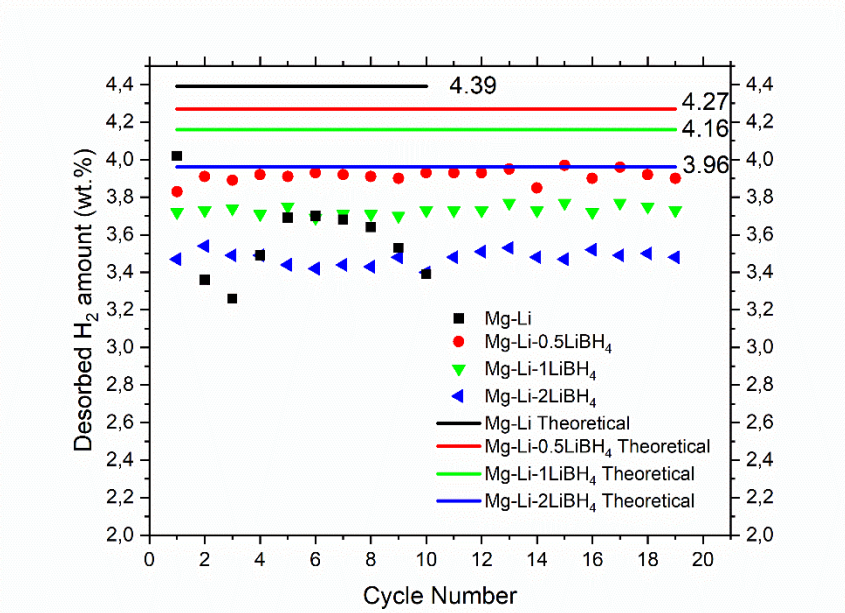

Figure 3.20 Desorbed H_2 amounts from the samples for the first 20 isothermal dehydrogenation cycles (180°C and 1 bar of H_2 pressure). Mg-Li sample is cycled 10 times due to long measurement time. Figure readopted from [57].

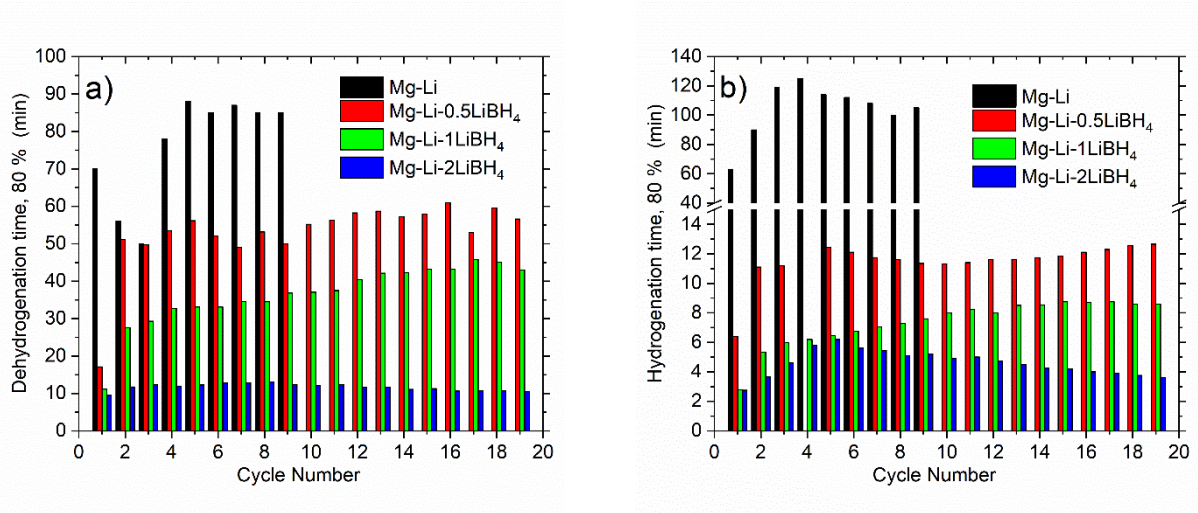

Figure 3.21 Times to reach 80% of the **(a)** dehydrogenation and **(b)** hydrogenation capacities over 20 cycles. Figure readopted from [57].

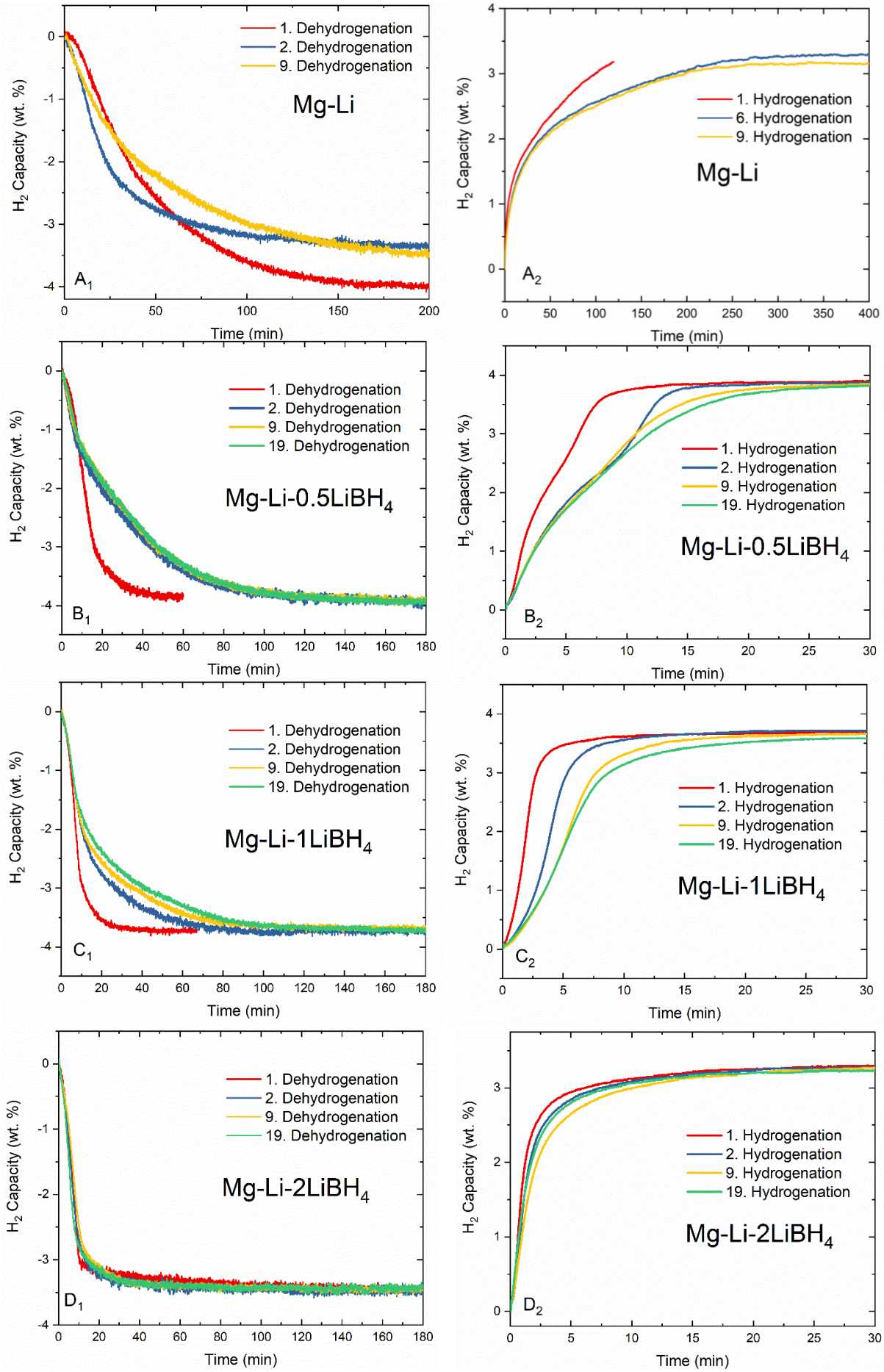

Figure 3.22 Kinetic curves upon cycling: Dehydrogenation (A_1-D_1) and hydrogenation (A_2-D_2) at 180°C and under 1 bar and 80 bar of H_2

3.2.6 Apparent activation energies

In order to evaluate the effect of the addition of $LiBH_4$ on the dehydrogenation kinetic behaviour of the Mg-Li composite, apparent activation energies (E_a) are calculated from DSC measurements by applying the Kissinger method. Figure 3.23 shows the results from Kissinger plots. All DSC curves along with the linear fitting for all the samples are shown in Appendix Figure A5. The apparent activation energy measured for the dehydrogenation of sample Mg-Li is found to be 170±1 $kJ \cdot mol^{-1}H_2$. The activation energies reported in literature for the dehydrogenation of Li-Mg-N-H system are very diverse and range from 102 to 180 $kJ \cdot mol^{-1}H_2$ [52], [98]. These variations can be attributed to different experimental conditions, i.e. gas flows, atmosphere, type of device and sample holder, as well as intrinsic parameters of the sample such as particle sizes, degree of mixture of reactants, crystal defects, among others. Reducing the particle size of $Mg(NH_2)_2$+2LiH system from 2 µm to 100 nm, the dehydrogenation E_a can be decreased from 182 to 122 $kJ \cdot mol^{-1}$ [98]. Introducing $LiBH_4$ has also an effect on the decrease of the E_a. For the Mg-Li-0.5$LiBH_4$ sample, E_a is lowered to 156±7 $kJ \cdot mol^{-1}$. A further reduction in the activation energy is observed for the samples Mg-Li-1$LiBH_4$ and Mg-Li-2$LiBH_4$, where E_a amounts 127±2 $kJ \cdot mol^{-1}$ and 129±1 $kJ \cdot mol^{-1}$, respectively. This represents 24 % of reduction in the E_a compared to $LiBH_4$-free sample, which is in good agreement with the data reported in literature [99].

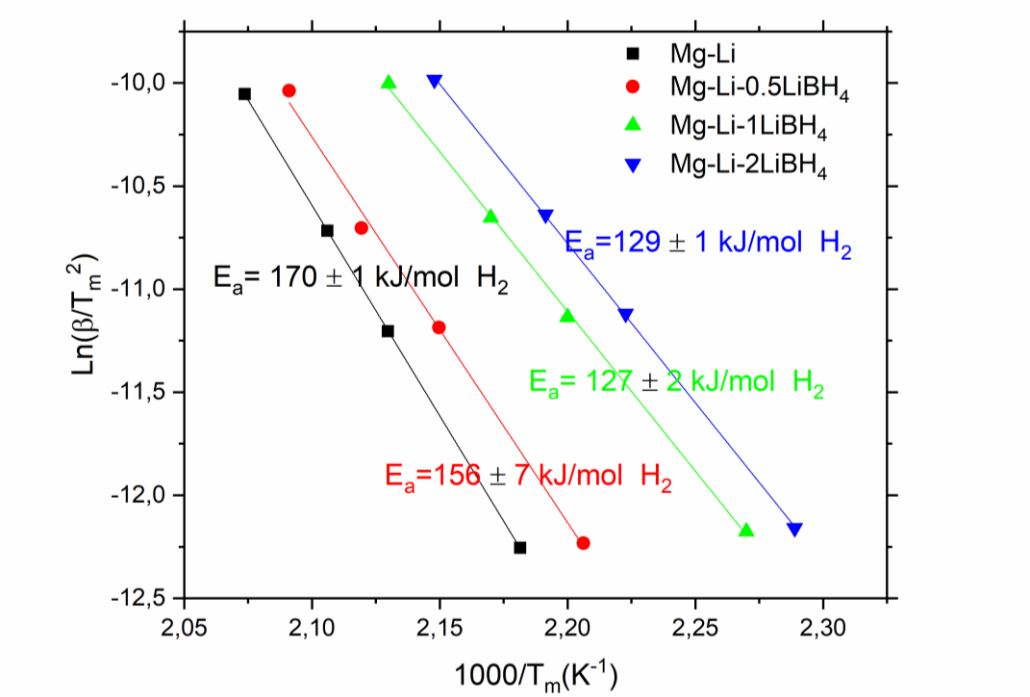

Figure 3.23 Kissinger plots of as-milled samples derived from DSC curves at different heating rates (1, 3, 5 and 10°C/min) for the calculation of the apparent activation energies. Figure readopted from [57].

3.3 $Mg(NH_2)_2$+2LiH+$K_2Mn(NH_2)_4$ system

In this section, we study the effect of bimetallic amide $K_2Mn(NH_2)_4$ on the hydrogen storage properties of $Mg(NH_2)_2$+2LiH. Detailed information related to the stoichiometric compositions of prepared samples are given in Table 2.4 . Thermal analyses coupled with evolved gas analyses are done via differential thermal analysis (DTA) coupled with a mass spectrometer (MS). Structural characterization during de/rehydrogenation reactions are investigated *in-situ* with synchrotron powder X-ray diffraction (SR-PXD) method, during both the first and the following cycles. This study provides new insight into the use of bimetallic amides as an additive on amide–hydride systems. The results presented in this section are published in Energies, 12(14), 2779, 2019, https://doi.org/10.3390/en12142779 [65].

3.3.1 Thermal analysis - mass spectroscopy

DTA curves and associated MS traces measured for the additive-free sample Mg-Li as well as for the $K_2Mn(NH_2)_4$-containing samples (Table 2.4) are shown in Figure 3.24. The curve of the Mg-Li sample exhibits an endothermic peak at 200°C with a shoulder at 190°C, which is in agreement with the two-step dehydrogenation pathway of $Mg(NH_2)_2$+2LiH (reactions 1.6 and 1.7). At this temperature, mainly H_2 is released together with a small amount of NH_3. Above 225°C, the release of NH_3 becomes dominant. Compared to the pristine system, the dehydrogenation reaction of the system containing 1 mol% $K_2Mn(NH_2)_4$ starts at a lower temperature (i.e. 110°C), whereas the maximum of the dehydrogenation peak at 200°C remains unchanged. When the additive amount is increased to 5 mol% (Mg-Li-5KMN), both dehydrogenation onset and peak temperature decrease to 80°C and 172°C, respectively. For both samples, Mg-Li-1KMN and Mg-Li-5KMN, the release of NH_3 below 200°C is most likely lower than the detection limit. However, increasing the amount of additives beyond 5 mol% (Mg-Li-35KMN) leads to a significant NH_3 release, which already starts at around 175°C. Despite the fact that the dehydrogenation peak temperature of Mg-Li-35KMN is the lowest (143°C), the H_2 peak area is also notably smaller in respect to those of the other samples. This is clearly due to the high amount of additive contained in this sample (~ 49 wt.%). Due to the low amount of released H_2 and high amount of released NH_3, the sample Mg-Li-35KMN is not investigated further. DTA and MS results indicate that Mg-Li-5KMN has the most promising properties (among the investigated systems), since it presents the lowest H_2 release onset temperature (80°C) with no NH_3 release until 200°C.

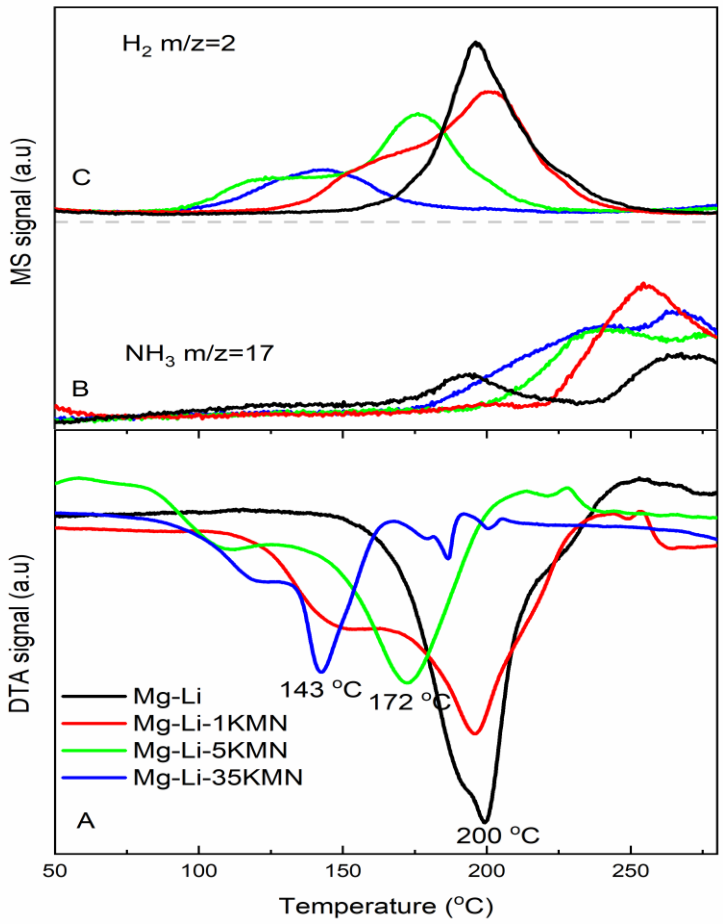

Figure 3.24 A Differential thermal analysis (DTA), **B–C** Mass spectroscopy (MS) traces of as-milled samples. Heating is applied from room temperature until 300°C with 3°C/min heating rate under 50 ml/min Ar flow. Figure readopted from [65].

3.3.2 *In-situ* synchrotron powder X-ray diffraction characterization

In order to understand the reaction pathway of Mg-Li-5KMN, its de/rehydrogenation reactions are investigated via *in-situ* SR-PXD technique. The results of this investigation (SR-PXD patterns as the function of temperature) are presented in the two-dimensional contour plot of Figure 3.25. The diffraction pattern acquired at room temperature (after ball milling) shows the existence of tetragonal $Mg(NH_2)_2$, cubic LiH, MgO and Mn_4N. Besides that, no $K_2Mn(NH_2)_4$ reflections are observed. During the first dehydrogenation (Figure 3.25-A), the reflections of cubic KH appear at 85°C. At the same temperature, peaks belonging to orthorhombic $Li_2Mg(NH)_2$ are also observed. As the temperature increases, the intensity of the $Mg(NH_2)_2$ peaks diminishes and the intensity of the $Li_2Mg(NH)_2$ peaks increases. The continuous shift of the diffraction peaks towards lower 2θ angles, observed upon heating, is due to thermal expansion. Through the first hydrogenation attempt (Figure 3.25-B), $Li_2Mg(NH)_2$ peak

intensities start to decrease at 110°C and a broad peak of $Mg(NH_2)_2$ appears at about $2\theta = 9°$. $Mg(NH_2)_2$ and LiH suddenly recrystallize at 165°C (sharp $Mg(NH_2)_2$ and LiH peaks appear). The absence of peaks ascribable to $K_2Mn(NH_2)_4$ through all the first cycles indicates that during ball milling, $K_2Mn(NH_2)_4$ transforms into Mn_4N and a potassium compound with amorphous or nanocrystalline features. Therefore, $K_2Mn(NH_2)_4$ must be considered as a precursor for the formation of Mn_4N and KH.

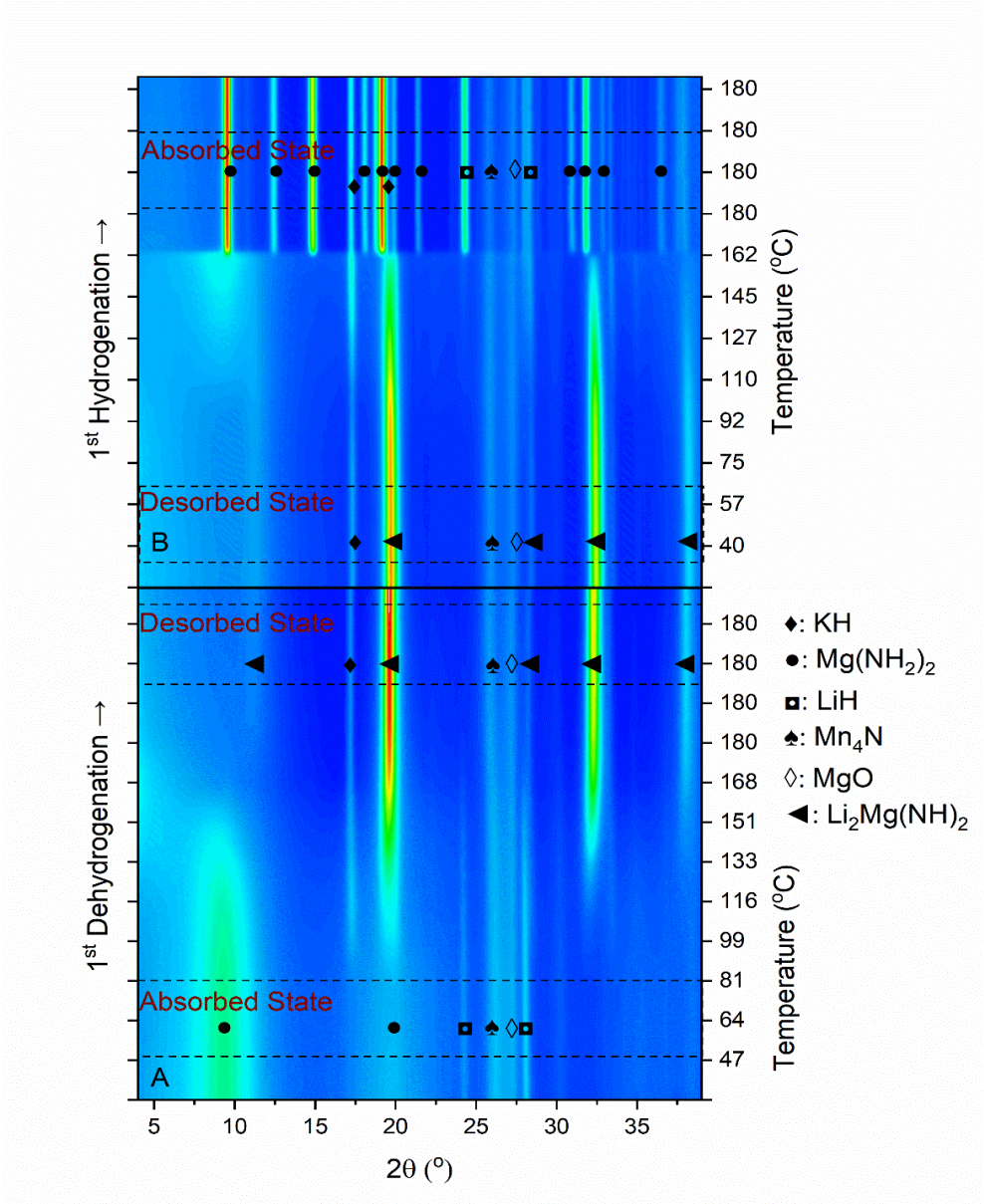

Figure 3.25 A *In-situ* synchrotron powder X-ray diffraction (SR-PXD) pattern for the first dehydrogenation of Mg-Li-5KMN under 1 bar of H_2. **B** *In-situ* SR-PXD pattern for the first hydrogenation of Mg-Li-5KMN under 80 bar of H_2. Sample is heated from RT until 180°C with 3°C/min heating rate and each 15 seconds, a SR-PXD data is collected (λ= 0.9941 Å). Additionally, dehydrogenation and hydrogenation experiments are extended to 30 minutes in isothermal conditions (180°C). Figure readopted from [65].

3.3.3 Volumetric analyses

The measured reaction kinetics of all the investigated samples are presented in Figure 3.26. Upon dehydrogenation, Mg-Li shows a release of hydrogen equal to 4.1 wt.%. The same amount is released in the Mg-Li-7KH system. The sample Mg-Li-5KMN has slightly lower H_2 capacity (3.8 wt.%). The amount of released hydrogen decreases to 3.5 wt.% and 3.2 wt.% for the samples Mg-Li-15KH and Mg-Li-30KH, respectively. The rehydrogenation kinetics of Mg-Li are slower than those of KH-containing samples and those containing $K_2Mn(NH_2)_4$. Interestingly, the rehydrogenation rate of Mg-Li-5KMN noticeably increases toward the end of the hydrogenation.

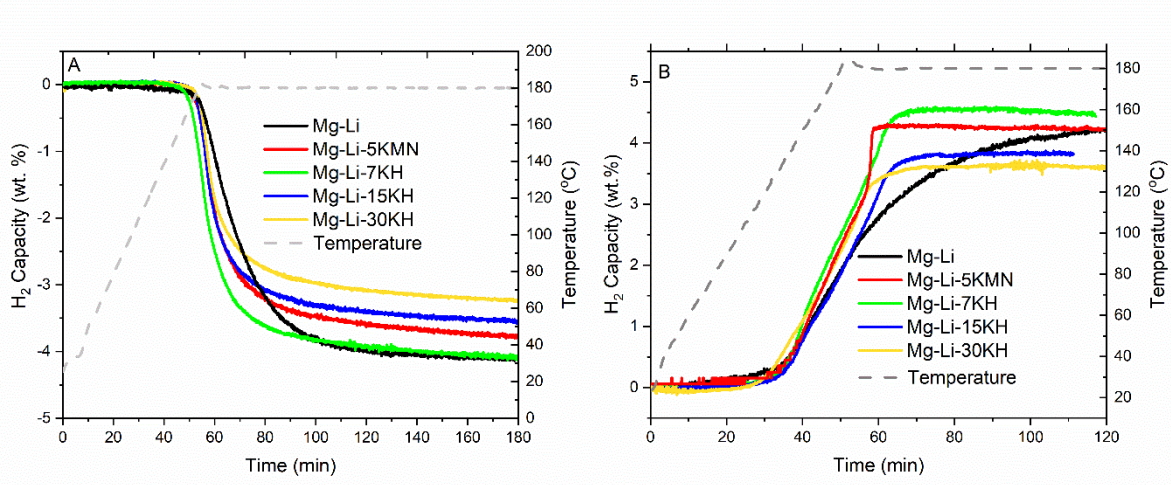

Figure 3.26 Non-isothermal (**A)** dehydrogenation, (**B)** rehydrogenation kinetics of prepared samples. Heating is applied from room temperature until 180°C, with a heating rate of 3°C/min. Dehydrogenation and rehydrogenation reactions are carried out under 1 bar and 80 bar of H_2, respectively. Figure readopted from [65].

3.3.4 Cycling stability

The observed rehydrogenation rate increases toward the end of the reaction (Figure 3.26-B), is preserved upon the following two de/rehydrogenation cycles, as seen on Figure 3.27.

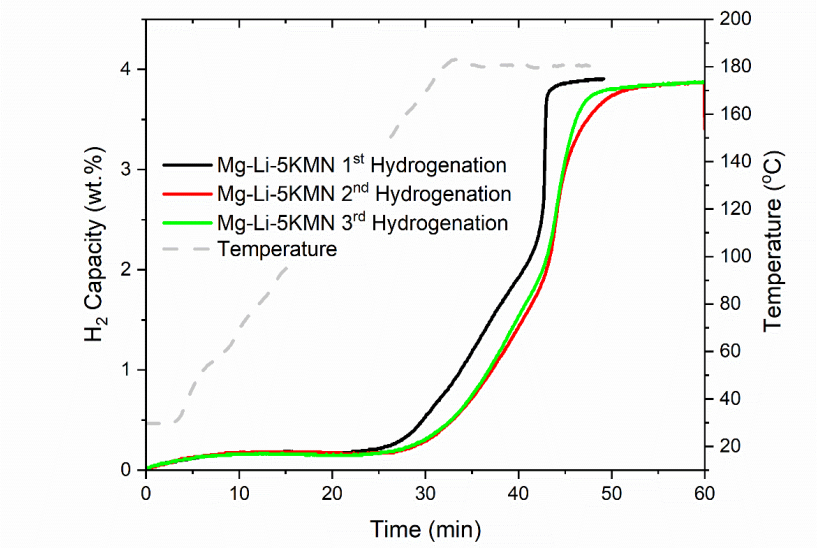

Figure 3.27 Hydrogenation kinetics of Mg-Li-5KMN for the first three cycles. Sample is heated from room temperature until 180°C with a heating rate of 5°C/min under 80 bar of H_2. Figure readopted from [65].

The volumetric measurements of the H_2 dehydrogenation for the 1st and 25th cycles of Mg-Li and Mg-Li-5KMN are presented in Figure 3.28-A. Mg-Li-5KMN sample releases 3.8 wt.% of H_2 within 3 hours in the first dehydrogenation. The amount of released H_2 reaches 4.2 wt.% in the second dehydrogenation, due to a longer measurement time. For this system, no noticeable loss in H_2 capacity is observed for 25 cycles. In contrast, the amount of released H_2 for Mg-Li after 25 cycles decreased from 4.2 wt.% to 2.2 wt.%. It is clear that repeated de/rehydrogenation cycles lead to slower reaction kinetics for both samples. *In-situ* SR-PXD contour plot of the Mg-Li-5KMN sample at the 25th dehydrogenation (Figure 3.28-B) reveals that identified phases are the same as in the first dehydrogenation (Figure 3.25). Thus, once formed, KH and Mn_4N additives appear to be stable.

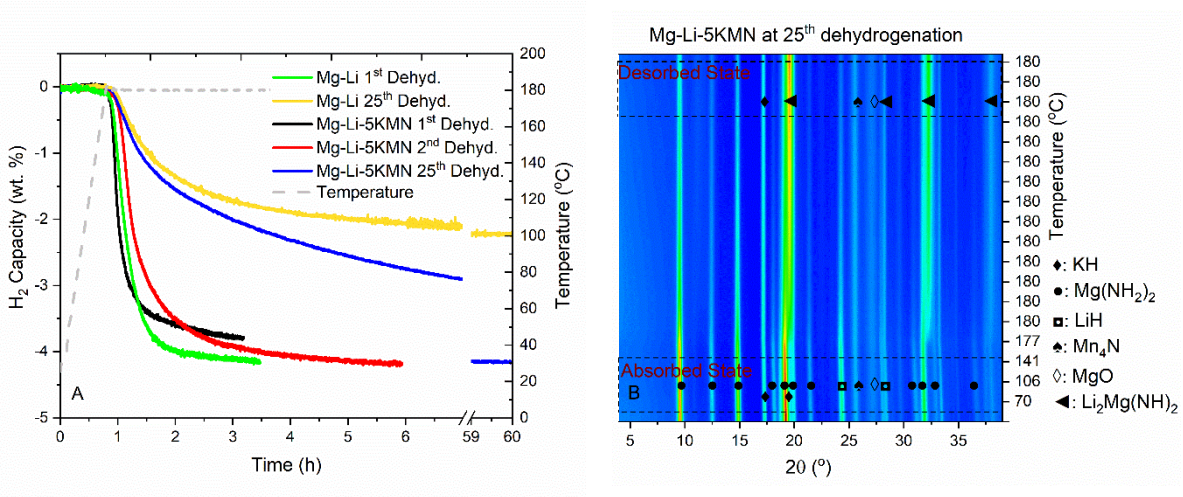

Figure 3.28 (A) Dehydrogenation kinetics of Mg-Li and Mg-Li-5KMN samples in the 1st and 25th cycles. Samples are heated from RT until 180°C with a heating rate of 5°C/min under 1 bar of H_2. **(B)** *In-situ* SR-PXD contour plot of Mg-Li-5KMN at 25th dehydrogenation under 1 bar of H_2. Sample is heated from room temperature until 180°C with 3°C/min heating rate, and each 15 seconds, a SR-PXD data is collected (λ= 0.9941 Å). Additionally, dehydrogenation experiment is extended to 120 minutes at isothermal conditions (180°C). Figure readopted from [65].

3.3.5 Apparent activation energies and rate constants

The Kissinger method is applied to calculate the apparent activation energies (E_a) and frequency factor (A) from DSC curves for Mg-Li and Mg-Li-5KMN samples (Figure 3.29-A). Considering the complexity of the reaction, mainly for the material with the additive, the temperatures at the observed maximum reaction rate are taken for the calculation of these parameters (Appendix Figure A6-A7). It is worthy to remind that the dehydrogenation peak temperature of Mg-Li-5KMN is 30°C lower than that of the pristine Mg-Li (Figure 3.24-A), and reaction kinetics are comparably faster (Figure 3.26). However, the E_a as well as A values are higher for the Mg-Li-5KMN than for Mg-Li, i.e. 196±5 kJ·mol^{-1}H_2 and 2.7 x 10^{22}, 161±5 kJ·mol^{-1}H_2 and 3.5 x 10^{17}, respectively. In order to understand these contradictory findings, rate constants (k) are calculated (Figure 3.29-B) by the Arrhenius expression $k = A \cdot \exp[-E_a/RT]$ (1/s) at the cycling temperature of 180°C. Then, k is multiplied with the H_2 capacities obtained from Figure 3.26-A in order to obtain reaction rates. Despite the fact that Mg-Li-5KMN has a higher E_a value in respect to Mg-Li, the calculated kinetic constant and reaction rate indicate faster kinetic behaviour for Mg-Li-5KMN at 180°C.

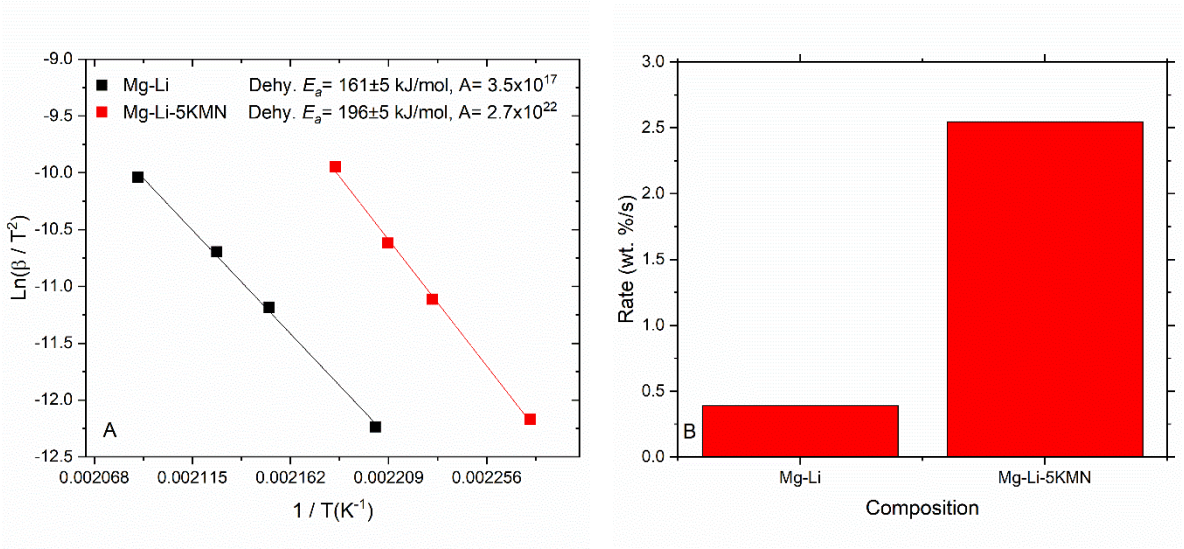

Figure 3.29 (A) Kissinger plots of samples Mg-Li and Mg-Li-5KMN, derived from Differential scanning calorimetry (DSC) curves of the first dehydrogenation reaction at different heating rates (1, 3, 5 and 10°C/min). Fitting goodness (R^2): 0.9979 for Mg-Li and 0.9985 for Mg-Li-5KMN. **(B)** Calculated reaction rate related to the corresponding samples. Figure readopted from [65].

4. Discussion

In the following section the experimental data reported in section 3 will be thoroughly discussed. As mentioned in the introduction section, until the early 2000s´ metal amides, e.g. $Mg(NH_2)_2$, were not considered as hydrogen storage materials, since significant amount of NH_3 is released from their thermal decomposition, as seen in Figure 4.1. From the thermogravimetric analysis carried out in the range of temperature RT-600°C, a weight loss of 39.75 % is determined for $Mg(NH_2)_2$, which is in agreement with the expected decomposition of $3Mg(NH_2)_2$ to Mg_3N_2 (~40%). Thermal analysis data in Figure 4.1 indicates that decomposition of $Mg(NH_2)_2$ takes place in two endothermic events with peak maxima at 375°C and 485°C entailing an overall enthalpy change (ΔH) of 120 $kJ \cdot mol^{-1}$ (per mol of NH_3). The decomposition reaction is expected to follow the mechanism described in reactions 4.1 and 4.2:

$$3Mg(NH_2)_2 \rightarrow 3MgNH + 3NH_3 \quad (4.1)$$

$$3MgNH \rightarrow Mg_3N_2 + NH_3 \quad (4.2)$$

Although $Mg(NH_2)_2$ desorbs only NH_3 at relatively high temperatures (>250°C), the composite system made of $Mg(NH_2)_2$ and LiH, upon thermal input, releases mostly H_2 in the temperature range 170-230°C, depending on the amide–hydride ratio (Figure 3.2 and Figure 3.15). According to the calculated thermodynamic properties of the $Mg(NH_2)_2$+2LiH mixture, if the kinetic issues could be solved, an operating temperature of 90°C would be possible at 1 bar H_2, which is highly attractive for mobile hydrogen storage applications in combination with PEM fuel cells. However, so far severe kinetic barriers prevent de/rehydrogenation from occurring at such a low temperature.

In literature, two mechanisms are proposed to explain the interactions between $Mg(NH_2)_2$ with LiH. The first mechanism can be described as an ammonia mediated mechanism, where $Mg(NH_2)_2$ first decomposes to MgNH and releases NH_3, which then reacts with LiH to produce hydrogen. The kinetic barrier in this mechanism should originate from the decomposition of $Mg(NH_2)_2$, since the reaction of LiH with NH_3 takes place in a milliseconds regime. The second mechanism is a coordinated solid-solid reaction mechanism. Hydrogen atoms attached to nitrogen normally possess positive charge ($H^{\delta+}$) whereas hydrogen atoms in ionic hydrides possess negative charge ($H^{\delta-}$). The strong attraction between $H^{\delta+}$ from the amide and $H^{\delta-}$ from the hydride is expected to be the driving force for the H_2 formation/release and

formation of imide products. Dehydrogenation reaction starts at the amide-hydride interface forming an imide layer, which then thickens as the reaction proceeds further. The reactions at the interfaces, the mass transport through the imide layer and particle size of amide and hydride phases determine the kinetic properties of the system.

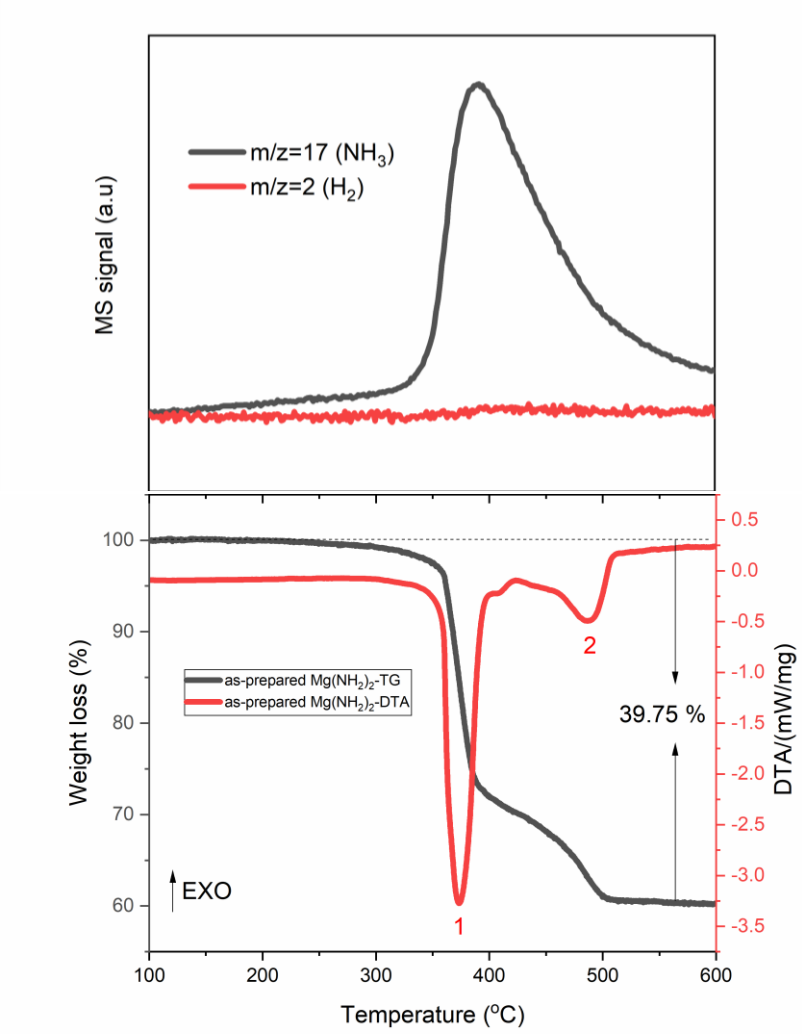

Figure 4.1 Thermal decomposition of $Mg(NH_2)_2$, corresponding weight loss and released gasses The specimen is heated from room temperature until 700°C under 50 ml/min Ar flow, with a heating rate of 5°C/min.

The optimization of the hydrogen storage capacity, the suppression of the ammonia release and the tailoring of the operating temperature of the Li-Mg-N-H system can be done by tuning the amide–hydride ratio [94], [100]. The tuning of the material properties is a direct consequence of the different dehydrogenation products, e.g. $Li_2Mg(NH)_2$, $Li_2Mg_2(NH)_3$, Li_2NH, Li_3N, Mg_3N_2 that are obtained by changing this ratio. In this work, the $Mg(NH_2)_2$/LiH ratios 1/2 and 6/9 are studied. The theoretical hydrogen storage capacity of the system $Mg(NH_2)_2$+2LiH is 5.5 wt.%, while it is 4.39 wt.% for the system $6Mg(NH_2)_2$+9LiH. Increasing the LiH content in the composite slightly increases the dehydrogenation peak

temperature from 195°C to 200°C, as shown in Figure 3.15-A and Figure 3.24-A. According to the ammonia-mediated mechanism as discussed above, the increment of LiH content in the composite will reduce the released amount of NH_3. Although with the current MS measurement the total amount of released gas cannot be calculated exactly, results from $6Mg(NH_2)_2$+9LiH (Figure 3.16-B) indicate a NH_3 to H_2 ratio of 1/2. In the case of $Mg(NH_2)_2$+2LiH composite (Figure 3.24), the NH_3 to H_2 ratio is only 1/15. These results confirm that increasing the LiH amount in the composite significantly reduces the NH_3 release, which is in good agreement with literature [100], [101]. Further improvements in terms of reaction kinetics, operating temperatures and NH_3 release can only be obtained by using appropriate additives and or modifying the system composition by the addition of further reactants. These approaches will be discussed in the following.

4.1 The $Mg(NH_2)_2$+2LiH+K-modified $Li_xTi_yO_z$ system

In the section 3.1, the microstructural and kinetic effects of the addition of $Li_xTi_yO_z$ and K-modified $Li_xTi_yO_z$ additives on the $Mg(NH_2)_2$+2LiH system have been studied. K-modified additives not only play a role in improving the kinetic behaviour (Figure 3.4) and cycling stabilities (Figure 3.5), but also help lowering the desorption onset and peak temperatures (Figure 3.2) in comparison to the pristine sample (Mg-Li). Mainly hydrogen is released from Mg-Li at the cycling temperature of 180°C, with comparably low amount of NH_3. However, suppression of NH_3 release at this temperature is achieved by the addition of LTOK (Figure 3.2-C). Then, the H_2 storage capacity is optimized by tuning the amount of this additive. Thus, a reversible H_2 capacity of about 3 wt.% at 180°C is achieved for Mg-Li-2.5LTOK (Figure 3.5). FT-IR analyses carried out for the sample Mg-Li and Mg-Li-2.5LTOK after milling, after desorption and absorption (Figure 3.6 E-H) confirmed that the reaction pathway described in reactions 1.6 and 1.7, is not altered.

When reaction rates of all samples are investigated in detail, the first and second desorption reaction rates for the samples containing potassium modified additive are faster than those of Mg-Li and Mg-Li-5LTO samples (Figure 3.8). However, the activation energies for LTOK containing samples are similar or higher than those of Mg-Li and Mg-Li-5LTO samples (Figure 3.7). This behaviour can be mainly attributed to an increase in the frequency factor, which hints towards a possible more efficient contact of the reactants at the interface. The faster rate of the sample with 5-mol. % LTOK during the first desorption is in agreement with the lower E_a in comparison with sample with 2.5-mol. % LTOK, suggesting a better distribution

of the additive. However, during the second desorption, the beneficial effects of the larger amount of additive is lost, suggesting that the additive might have agglomerated and now behave as a barrier between reactants.

Initial structural analysis on the composition of the additives after synthesis indicate that LTO additive (initial composition: 0.5LiH+TiO_2) is composed of the single phase $LiTi_2O_4$ (Figure 3.1-A). The constituents of the as synthesized potassium modified additive (initial composition: 0.5LiH+TiO_2+0.25KH), are 10 wt.% $K_{1.04}O_{16}Ti_8$, 17 wt.% $LiTi_2O_4$, 27 wt.% $LiTiO_2$ and 46 wt.% $K_2O_{17}Ti_8$ (Figure 3.1-B). The composition of the additive after milling with $Mg(NH_2)_2$ and LiH appear to change. SR-PXD analyses of the Mg-Li-5LTOK sample (Figure 3.3) provide a hint about the presence of stable $Li_xTi_yO_4$ compounds ($0.75 \leq x \leq 1$ and $1.9 \leq y \leq 2$). Therefore, the composition of the additives in the LTOK after milling is not known. For this reason, X-ray absorption spectroscopy near edge structure (XANES) technique is applied in order to investigate the oxidation state of Ti. From this analyses, it is found that after milling, after dehydrogenation or rehydrogenation, the nature of the K-modified additive is not altered (Figure 3.9). XANES spectra of the as-milled LTO and K-modified LTOK indicate that the valence state of Ti atoms in Mg-Li-5LTO and Mg-Li-5LTOK are, on average, higher than +3.5 and lower than +4. There is a slight shift toward higher energies on the Ti absorption edge of Mg-Li-5LTOK sample in comparison to Mg-Li-5LTO. This suggests that a different titanium compound could be formed in the potassium-containing samples. If potassium containing samples (Mg-Li-5LTOK and Mg-Li-2.5LTOK) are compared, there is a slight change on the Ti absorption edge (Figure 3.11-B). This means, the effective valence state of the Ti atoms in the samples slightly depends on the amount of the K-based additive. In the case of Mg-Li-5LTOK, it is possible to reproduce the obtained spectrum considering the following contributions: 76 % of Mg-Li-2.5LTOK and 24 % of LTO additive ($LiTi_2O_4$) as shown in Figure 3.12.

TEM analysis reveals that Mg-Li-5LTO contains species such as $LiTi_2O_4$ and $Li_{0.07}TiO_2$. Whereas K-Ti-O and $LiTi_2O_4$ are observed in Mg-Li-2.5LTOK (Figure 3.13). Dark field images formed from 3rd and 4th rings for Mg-Li-5LTO and from the 3rd ring for Mg-Li-2.5LTOK reveal the presence of small nanoparticles in the range of 5 to 30 nm that can be attributed to the Li-Ti-O and K-Ti-O species. HR-TEM results indicate the presence of nanoparticles of $Li_{0.07}TiO_2$ (tetragonal) and $LiTi_2O_4$ (cubic) in the as-milled Mg-Li-5LTO sample (Figure 3.14-A). Nanoparticles of K_2TiO_3 (orthorhombic) and $LiTi_2O_4$ (cubic) are found for the as-milled Mg-Li-2.5LTOK (Figure 3.14-B). The presence of these nanoparticles

leads to an effective oxidation state of Ti between +3.5 and +4 (K_2TiO_3 = +4, $LiTi_2O_4$= +3.5), which is in good agreement with the XANES results (section 3.1.7).

In order to further investigate the role of the additive on the Li-Mg-N-H system, an analysis on the rate-limiting steps [102] of Mg-Li and Mg-Li-2.5LTOK samples is carried out for the 1st,2nd and 5th absorption/desorption kinetic curves from Figure 3.5(APPENDIX Figure A8-A19, Table A1-A4). The results are summarized in Table 4.1. Desorption rates are limited by an interface controlled mechanism (F1: JMA, n=1), while absorption rates are limited by a diffusion controlled mechanism. In the case of absorption reaction, D3 and D4 represent diffusion mechanisms as rate limiting step, but with different geometries of particles (D3: spheres and D4: different forms). Therefore, the K-modified additive does not change the rate-limiting step for desorption/absorption reactions. However, in both absorption and desorption mechanisms, the rate-limiting step is notably accelerated. In general, the results are in well agreement with the results obtained from our previous work, where amide/hydride molar ratio is 6/9 instead of 1/2 [57].

Table 4.1 Using Sharp and Jones method [76], [77], rate-limiting processes of samples, which are taken from isothermal cycling kinetic curves of Figure 3.5

Desorption		
	Mg-Li	Mg-Li-2.5LTOK
1st Desorption	F1	F1
2nd Desorption	F1	F1
5th Desorption	F1	F1
Absorption		
	Mg-Li	Mg-Li-2.5LTOK
1st Absorption	D3	D3
2nd Absorption	D4	D3
5th Absorption	D3	D3
F1 : JMA, n = 1, Random nucleation, one-dimensional interface controlled growth D3 : Three-dimensional diffusion, spherical particles D4 : Three-dimensional diffusion, free geometry		

The results reported in this work suggest that the presence of the K_2TiO_3 species are responsible for the observed improvements in the kinetic behaviour and cycling stability of the Mg-Li-2.5LTOK. Kinetic enhancements from the alkali metals and their hydrides/hydroxides/amides are still debated in literature. In particular, the possibility that they modify the thermodynamics of the system or that they have a catalytic effect on the system is

a matter of discussion [64], [66], [103]–[108]. In literature the catalytic activity of KH and RbH is explained via destabilization of the N-H bond due to their high electronegativity [64]. KH firstly reacts with $Mg(NH_2)_2$ and later metathesizes with LiH to regenerate KH [66]. Based on our results from *in-situ* SR-PXD (Figure 3.3) and XANES (Figure 3.9), it is possible to state that K_2TiO_3 does not change the reaction pathway, i.e. it does not affect the thermodynamics of the system. However, the presence of K_2TiO_3 positively affects the reaction kinetic behavior and improves the reversibility of the $Mg(NH_2)_2$+2LiH system (Figure 3.5). These improvements are revealed by the increased reaction rate constant, while hydrogen capacities stay constant upon cycling (Figure 3.5, Figure 3.8). An analysis on the rate-limiting steps showed that the presence of K_2TiO_3 does not lead to a change of the rate-limiting step, but it accelerates this step both in hydrogen absorption and desorption reactions (Table 4.1). The rate limiting step upon hydrogenation is one-dimensional interface controlled growth, but upon dehydrogenation is diffusion controlled. The fact that the presence of the *in-situ* formed K_2TiO_3 nanoparticles improves the cycling stability can be ascribed to the location of the additive on the boundaries precluding agglomeration phenomena. In terms of mechanism, in the literature, it is found that potassium reacts both with amide and hydride to create more intermediate compounds to generate energy-favorable pathway [66], [109]. The species KH, $KLi_3(NH_2)_4$ and $K_2Mg(NH_2)_4$ are reversible during hydrogenation-dehydrogenation. On the contrary, it is reported that KH acts as a catalyst and does not change the thermodynamic behavior of the material [110], as well as it is shown for the system reported here. For the amide-hydride reactive hydride composite system, the transport of species at the interfaces are critical and represents the most severe kinetic constraint [111]. Thus, the formation of K_2TiO_3, the observed accelerated interface movements and diffusion mechanism can be ascribed to the enhancement of mobility of the species. Certainly, a thorough investigation of the observed phenomena should be carried out to shed light on the catalytic mechanism of K_2TiO_3. However, this could not be done in the time frame of this work.

4.2 The $6Mg(NH_2)_2$+9LiH+$LiBH_4$ system

In the section 3.2, the hydrogen storage properties of $6Mg(NH_2)_2$+9LiH+$x(LiBH_4)$ (x = 0, 0.5, 1, 2) system and the role of $LiBH_4$ on the kinetic behaviour and on the de/rehydrogenation reaction mechanism are systematically investigated. Previous reports, which investigated the effect of borohydrides on the Li-Mg-N-H system [112], [113], revealed that both $Mg(BH_4)_2$ and $CaBH_4$ undergo metathesis reactions with LiH to form $LiBH_4$ and MgH_2 or CaH_2. $LiBH_4$

is the species that improves the system performance and the formation of side products such as MgH_2 or CaH_2 reduces the reversible hydrogen capacity of the system. The addition of 0.1 mole $LiBH_4$ to $Mg(NH_2)_2$+2LiH not only improves the reaction kinetics, but also reduces the reaction enthalpy from ~40 kJ·mol$^{-1}H_2$ to 36.5 kJ·mol$^{-1}H_2$ [52], [71], [114] . Thermodynamic alteration is achieved by stabilizing the dehydrogenation product, which refers to $LiNH_2$ in this system [70]. Depending on the molar ratios of $Mg(NH_2)_2$, LiH and $LiBH_4$; H_2 capacities and operating temperatures can be tailored [115]. $6Mg(NH_2)_2$+9LiH+$x$$LiBH_4$ (x = 0, 0.5, 1, 2) system offers theoretical H_2 capacities ranging between 4.0 to 4.5 wt.% at moderate temperatures (140℃-200℃), based on the general reaction 4.3;

$$6Mg(NH_2)_2 + 9LiH + xLiBH_4 \leftrightharpoons 3Li_2Mg_2(NH)_3 + (LiNH_2)_3(LiBH_4)_x + 9H_2 \quad (4.3)$$

In this work, based on the results from PXD (Figure 3.17) and FT-IR (Figure 3.18), we confirm that the reaction pathways of $LiBH_4$-containing samples are multiple. On the one hand, the Mg-Li-0.5$LiBH_4$ sample forms $LiNH_2$, $Li_4(BH_4)(NH_2)_3$ and $Li_2Mg_2(NH)_3$ as dehydrogenation products, following the reaction 4.4

$$6Mg(NH_2)_2 + 9LiH + 0.5LiBH_4 \leftrightharpoons 3Li_2Mg_2(NH)_3 + 1.5LiNH_2 + 0.5Li_4(BH_4)(NH_2)_3 + 9H_2 \quad (4.4)$$

On the other hand, $LiNH_2$ is not present in the Mg-Li-1$LiBH_4$ and Mg-Li-2$LiBH_4$ samples. The main dehydrogenation products are $Li_2Mg_2(NH)_3$, $Li_4(BH_4)(NH_2)_3$ and possibly $Li_2(BH_4)(NH_2)$, following reaction 4.4. In a previous work, the formation of $Li_2(BH_4)(NH_2)$ during the dehydrogenation reactions of Li-Mg-B-N-H system was shown [114]. This phase is present at the beginning of dehydrogenation and transforms into $Li_4(BH_4)(NH_2)_3$ and $LiBH_4$ in the later stage of the reaction [114]. Since we focused on the characterization of the samples after dehydrogenation, it is possible that this intermediate already transformed into $Li_4(BH_4)(NH_2)_3$.

$$6Mg(NH_2)_2 + 9LiH + 1LiBH_4 \leftrightharpoons 3Li_2Mg_2(NH)_3 + Li_4(BH_4)(NH_2)_3 + 9H_2 \quad 4.5$$

$$6Mg(NH_2)_2 + 9LiH + 2LiBH_4 \leftrightharpoons 3Li_2Mg_2(NH)_3 + Li_4(BH_4)(NH_2)_3 + LiBH_4 + 9H_2 \quad 4.6$$

The formation of complex amide-borohydrides ($Li_4(BH_4)(NH_2)_3$, $Li_2(BH_4)(NH_2)$) plays a crucial role in improving the kinetic behaviour of the $6Mg(NH_2)_2$+9LiH+$x$$LiBH_4$ system

[116]. Moreover, the complex amide-borohydride $Li_4(BH_4)(NH_2)_3$ is known to have a high ion conductivity and a melting point of ~190 °C [117]. In addition, the melting point of $Li_2(BH_4)(NH_2)$ is at 90 °C and ion conductivity at its melting temperature is doubled respect to $Li_4(BH_4)(NH_2)_3$ [117].

These results illustrate that addition of $LiBH_4$ to the $6Mg(NH_2)_2$+9LiH system leads to a noticeable decrement of the apparent activation energies (170 $kJ \cdot mol^{-1}H_2$ for Mg-Li and 129 $kJ \cdot mol^{-1}H_2$ for Mg-Li-$2LiBH_4$) and significant improvement in reaction kinetics (Figure 3.22) as well as cycling stability (Figure 3.21). In order to gain an understanding of the intrinsic kinetic constraints for the hydrogenation and dehydrogenation processes upon cycling, solid-state reaction rate models are applied to the 1st and 9th de/rehydrogenation cycles (Figure 3.22) for the samples. Mg-Li, Mg-Li-$0.5LiBH_4$ and Mg-Li-$2LiBH_4$. This is the first time that such thorough analysis is carried out with this tri-component system, to the best of my knowledge. The results from the fittings are listed in Table 4.2. All the fitting details are shown in Appendix Figure A20-A25 and Table A5-A16.

Table 4.2 Rate-limiting processes of samples, which are defined from isothermal reaction curves with Sharp and Jones method

Sample code	**Dehydrogenation**		**Hydrogenation**	
	1st	**9th**	**1st**	**9th**
Mg-Li	R3	D1	D3	D3
Mg-Li-$0.5LiBH_4$	F2	D1	R3	R3
Mg-Li-$2LiBH_4$	F2	F2	F1	F1

R3 : Three-dimensional growth of contracting volume with constant interface velocity

D1 : One-dimensional diffusion

D3 : Three-dimensional diffusion

F1 : JMA, n = 1, Random nucleation, one-dimensional interface controlled growth

F2 : JMA, n = 1/2, Random nucleation, one-dimensional diffusion with constant number of nuclei

In the case of the first dehydrogenation, it is possible to see that the rate-limiting steps are different, if the sample contains $LiBH_4$ (Table 4.2). The Mg-Li sample is limited by interface mechanism, while all the $LiBH_4$-containing samples present diffusion controlled mechanism (F2).

For the pristine sample Mg-Li, R3-model suggests that the reaction rate during the first dehydrogenation is controlled by the reactions occurring at the interfaces, in agreement with previously reported work [111]. Independently from the concentration of $LiBH_4$, best fitting for all $LiBH_4$-containing samples is obtained by the F2 diffusion controlled model. In comparison to the system Mg-Li, these samples have a faster 1st dehydrogenation kinetics (Figure 3.22). It is clear that the reaction pathway for the $LiBH_4$-containing samples are different from the pristine one. In the presence of $LiBH_4$, more stable dehydrogenation products are obtained at the amide-imide interfaces by the formation of $Li_4(BH_4)(NH_2)_3$. Formation of this phase accounts for the change in the mechanism, i.e. from R3 (Mg-Li) to F2. Once $Li_4(BH_4)(NH_2)_3$ is formed, this highly ionic conductive species may assist the mass transport of ions that are responsible for de/rehydrogenation reactions.

For the ninth dehydrogenation, the results of the kinetic modelling indicate that both Mg-Li and Mg-Li-0.5$LiBH_4$ are controlled by D1 diffusion model as rate-limiting step. It is noteworthy that the dehydrogenation kinetics of the Mg-Li-0.5$LiBH_4$ sample significantly slows down after cycling (Figure 3.22). It is possible to see that the rate-limiting step for Mg-Li-0.5$LiBH_4$ is the same as for the pristine one. The poor kinetic properties observed in the samples containing a small amount of $LiBH_4$ can be due to agglomeration and phase segregation, occurring at temperature (i.e. 180 °C). It was reported before that this is a general problem for the Li-Mg-N-H system [61], [118]. For the Mg-Li-2$LiBH_4$, instead, the rate-limiting step does not change after cycling (F2). This sample maintains its fast dehydrogenation kinetics over the 20 cycles (Figure 3.22). Adding more $LiBH_4$ could lead to the formation of $Li_4(BH_4)(NH_2)_3$ and $Li_2(BH_4)(NH_2)$. However herein, based on the analysis through the gas-solid models, it is proposed that the kinetic constraints come mainly from the solid-solid diffusion processes of the species to form $Li_4(BH_4)(NH_2)_3$ and $Li_2(BH_4)(NH_2)$.

Also in the case of the 1st hydrogenation kinetic of samples containing $LiBH_4$, depending of the system stoichiometry, the rate-limiting steps change (Table 4.2). Reaction-rate of the Mg-Li sample is controlled by three-dimensional diffusion (D3) model. This limiting mechanism has been observed in several metal hydride systems [119]. Considering that the Mg-Li is a multi-component system, it is possible to relate the diffusion-controlled mechanism to the slow mobility of the species upon hydrogenation. Mg-Li-0.5$LiBH_4$ and Mg-Li-2$LiBH_4$ sample show interface controlled mechanisms (R3 and F1). Hydrogenation kinetics of all $LiBH_4$-containing samples are much faster than the one of Mg-Li sample (Figure 3.22). The faster hydrogenation rates, the reaction pathways and the rate-limiting step models, suggest

that the enhancement of the kinetic behaviour (Figure 3.22) can be attributed to the presence of highly ionic species as shown in reaction 4.3. At the ninth hydrogenation, the rate-limiting steps do not change for any of the samples compared to the first hydrogenation, which is in agreement with the changes observed for the hydrogenation curves.

4.3 The $Mg(NH_2)_2$+2LiH+$K_2Mn(NH_2)_4$ system

In the section 3.3, the effect of bimetallic amide $K_2Mn(NH_2)_4$ on the hydrogen storage properties of $Mg(NH_2)_2$+2LiH system is studied. DTA and MS results indicated that Mg-Li-5KMN has the most promising properties (among the investigated systems), since it presents the lowest H_2 release onset temperature (80°C) with no NH_3 release until 200°C (Figure 3.24). Rietveld refinement performed on the diffraction patterns acquired after the first de/rehydrogenation cycle (Figure 3.25 and Figure 4.2) reveals that Mg-Li-5KMN sample is composed of $Mg(NH_2)_2$ (60.6 wt.%), LiH (29.8 wt.%), KH (3.1 wt.%), MgO (3.5 wt.%).

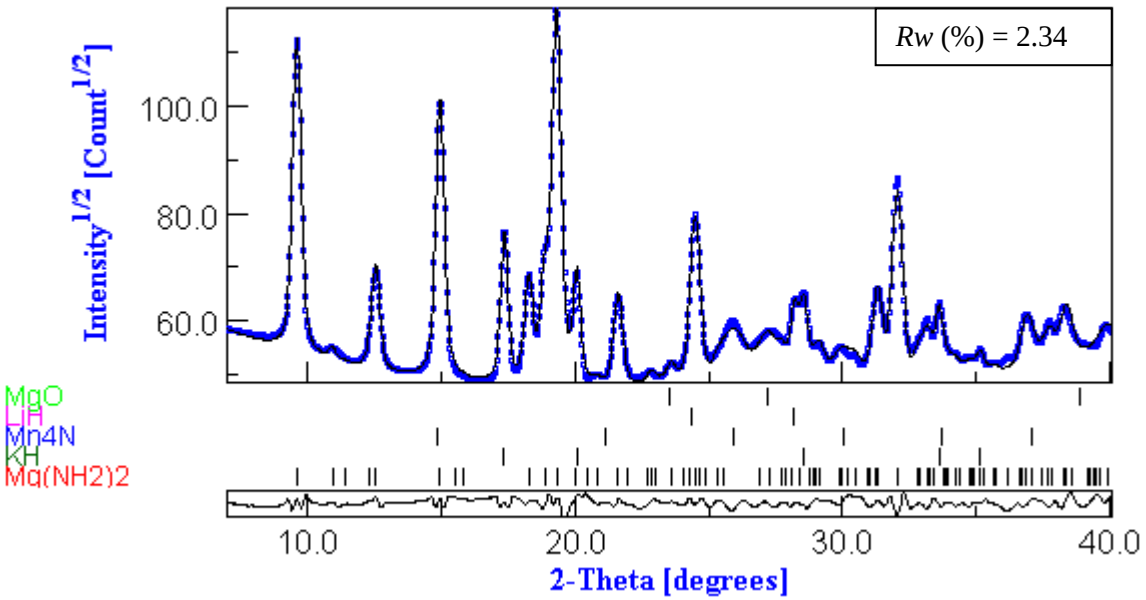

Figure 4.2 SR-PXD pattern of the Mg-Li-5KMN after rehydrogenation, λ= 0.9941 Å. Blue dots: Measurement data, Black line: Calculated fit

Since $K_2Mn(NH_2)_4$ is not present in the *in-situ* SR-PXD data (Figure 3.25), we expect that it decomposes into KH and Mn_4N with NH_3 and H_2 release as shown in reaction 4.7;

$$4Mg(NH_2)_2 + 8LiH + 4K_2Mn(NH_2)_4 \rightarrow 4Li_2Mg(NH)_2 + 8KH + Mn_4N + xNH_3(g) + yH_2(g) \quad 4.7$$

In the literature, some metal nitrides (TaN and TiN) are known to catalytically enhance the dehydrogenation of the $2LiNH_2+MgH_2$ system [120]. Besides that, the Mn_4N+LiH system is known to be an effective catalyst for NH_3 synthesis [121]. Therefore, we firstly studied the possible effect of Mn_4N on the reaction kinetics and thermal behaviour of the $Mg(NH_2)_2+2LiH$ system. However, we could not observe any beneficial effect from Mn_4N either in DSC analysis or in the volumetric H_2 release curves (Figure 4.3 and 4.4).

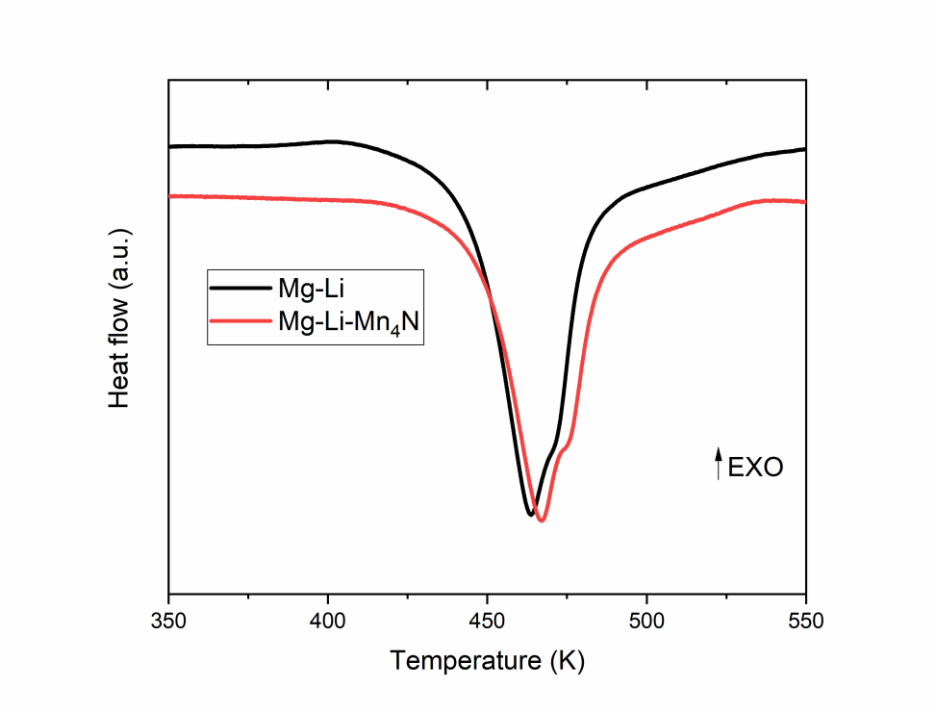

Figure 4.3 DSC curves of Mg-Li and 5 mol % Mn_4N containing Mg-Li samples. Heating rate: 3K/min

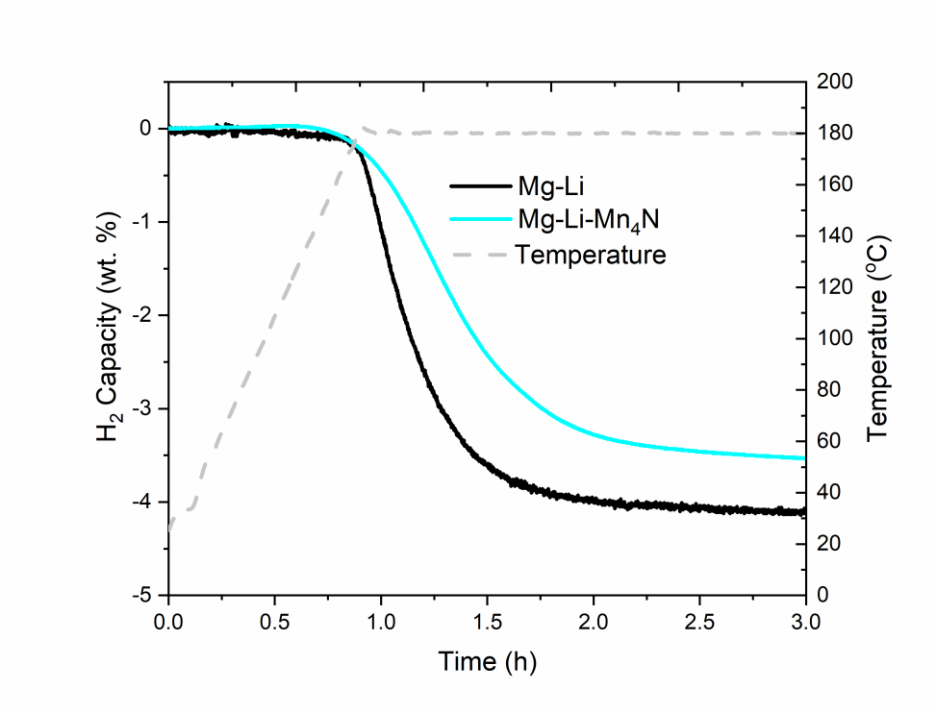

Figure 4.4 H_2 release curves of Mg-Li and 5 mol % Mn_4N containing Mg-Li samples under 1 bar of H_2. Heating: RT → 180°C, 3°C/min

Secondly, the effect of pure KH additions is investigated, which is also known to be an effective additive to reduce dehydrogenation peak temperature and improve reaction kinetics of the $Mg(NH_2)_2$+2LiH system [51], [66]. In order to compare the kinetic behaviour of all investigated samples, the measured H_2 capacity from Figure 3.26 is normalized. Apparently, the kinetic behaviours of all additive-containing samples are very similar and they are comparably faster than the pristine Mg-Li. The slow dehydrogenation kinetics obtained from the Mg-Li sample at 180°C is not surprising, since the corresponding peak temperature observed in the DSC analysis measured under 1 bar of H_2 is as high as 216°C (Figure 3.24).

Interestingly, the rehydrogenation rate of Mg-Li-5KMN noticeably increases toward the end of the hydrogenation. In fact, the last 1 wt.% of H_2 is loaded in only 2 minutes (Figure 3.24). This rehydrogenation rate (at this stage of hydrogenation) is four times faster than that of Mg-Li-7KH. This result suggests that the presence of $K_2Mn(NH_2)_4$ and the *in-situ* dual formation of KH and Mn_4N accelerated the diffusive processes commonly found in the last stage of hydrogenation processes owing to the formation of low H_2 diffusion coefficients of the hydride phases [79]. The fast rehydrogenation behaviour is preserved in the following two cycles (Figure 3.27). Interestingly, the third hydrogenation is faster than the second, which is observed before with a similar system [73]. Usually, hydrogenation of materials are slower at

the later stage [40], [122]. In practical applications, fast kinetics are favoured [123], [124]. In the case of $K_2Mn(NH_2)_4$-containing samples, the fast hydrogenation kinetics at later reaction stages represent an advantage over other hydrogen storage systems, with which full saturation is hardly reached.

The cycling performance of the Mg-Li-5KMN sample revealed that H_2 capacity is retained over 25 cycles (Figure 3.28-A). In contrast, the amount of released H_2 for Mg-Li after 25 cycles decreased from 4.2 wt.% to 2.2 wt.%. It is clear that repeated de/rehydrogenation cycles lead to slower reaction kinetics for both samples. It was already reported that for the amide-hydride systems, high operating temperatures cause the agglomeration of de/rehydrogenation products and segregation of reactants and K-based additives [125]. Although reaction kinetics of Mg-Li-5KMN slow down upon cycling, the positive effect of the presence of additives on the reversibility of the sample remains within the measured 25 cycles. *In-situ* SR-PXD contour plot of the Mg-Li-5KMN sample at the 25th dehydrogenation (Figure 3.28-B) reveals that formed KH and Mn_4N additives are stable over 25 cycles.

It is reported that the reaction pathway of KH-doped $Mg(NH_2)_2$+2LiH is different under argon and hydrogen atmosphere [66], [126]. Dehydrogenation under hydrogen instead of argon alters the dehydrogenation products, which results in an increase of E_a in the case of Mg-Li-5KMN with respect to Mg-Li. This behaviour is different from the reports in the literatures, where E_a is lowered with the addition of K-compounds [104], [127]. Despite the fact that Mg-Li-5KMN has a higher E_a value in respect to Mg-Li, the calculated kinetic constant and reaction rate indicate faster kinetic behaviour for Mg-Li-5KMN at 180°C (Figure 3.29). These outcomes are in agreement with the observed kinetic behaviour (Figure 3.26). It suggests that the notable increase of the frequency factor for Mg-Li-5KMN prompts a more efficient interaction between reactants at the interphases, resulting in faster kinetic behaviour.

Among the different systems investigated in this work, $Mg(NH_2)_2$+LiH+$LiBH_4$ appears to be the most promising system for future applications. One of the main advantages of this system, differently from the systems containing $K_2Mn(NH_2)_4$ or K-modified $Li_xTi_yO_z$ additives, is its stable reaction kinetics over several hydrogen release and uptake (Figure 3.22). In contrast, $K_2Mn(NH_2)_4$-containing system shows very poor reactions kinetics after 25 de/rehydrogenation cycle (Figure 3.28). In the case of K-modified $Li_xTi_yO_z$ containing samples, although the hydrogen storage capacities are stable over five de/rehydrogenation cycles, the hydrogenation rates are significantly slower respect to $LiBH_4$-containing samples (Figure 3.5, Figure 3.22). One of the other advantages of $Mg(NH_2)_2$+LiH+$LiBH_4$ system is its

tuneable thermodynamic properties. Changing the amide-hydride-borohydride ratio, operating temperatures can be reduced to the working temperatures of PEM fuel cells, which is extremely appealing from the application point of view. As well as advantages, there are also some disadvantages of this system. The most common drawback of $Mg(NH_2)_2$+LiH+$LiBH_4$ system is the release of NH_3 during the de/rehydrogenation reactions (Figure 3.16), which is expected to negatively affect the overall H_2 storage capacity. Furthermore, even few ppm of NH_3 can be poisonous for PEM fuel cell membranes. However, no detectable reduction in the H_2 capacity is observed for the samples (Figure 3.20). It is possible that during dehydrogenation under constant pressure (volumetric measurements), released NH_3 from the magnesium amide reacts again with the lithium hydride to proceed dehydrogenation. Deeper investigations on the NH_3 release of the samples under real operating conditions are planned for the near future.

5. Summary and Conclusions

The main objective of this work is to study the interaction of additives with the Li-Mg-N-H system, composed of $Mg(NH_2)_2$ and LiH with 1/2 or 6/9 molar ratios. The findings of this work, for each investigated additive, are summarized in individual paragraphs and are reported hereunder.

Microstructural and kinetic effects of lithium titanate ($Li_xTi_yO_z$) and potassium modified lithium titanate (K-modified $Li_xTi_yO_z$) additives on the $Mg(NH_2)_2$+2LiH system indicate that the addition of 5 mol. % of K-modified $Li_xTi_yO_z$ reduces the desorption peak temperature of pristine sample, $Mg(NH_2)_2$+2LiH, by 30°C and suppresses NH_3 release until 220°C. Interestingly, 2.5 mol. % of K-modified $Li_xTi_yO_z$ (Mg-Li-2.5LTOK) has comparably higher apparent activation energy (211±1 kJ·mol^{-1}) with respect to the pristine sample (183±7 kJ·mol^{-1}), whereas the calculated rate constant (*k*) values for the first and second desorption reactions are higher than in the pristine sample, which is in good agreement with the observed reaction behaviour. In accordance with XANES analysis, orthorhombic K_2TiO_3 and cubic $LiTi_2O_4$ phases are detected in HR-TEM. Based on the results from *in-situ* SR-PXD plot and XANES analysis, it is proposed that K_2TiO_3 nanoparticles act as catalyst and they positively affect the reversible reactions of the $Mg(NH_2)_2$+2LiH system. Analyses on the rate-limiting steps, kinetic behaviour and rate constants calculations illustrate that presence of K_2TiO_3 does not lead to a change of the rate-limiting step, but it accelerates this step both in hydrogen absorption and desorption reactions. K_2TiO_3 containing samples possess a possible more efficient contact of the reactants at the interface. Therefore K_2TiO_3 acts as a catalyst rather than as a reactant capable of changing the thermodynamics of the system.

The addition of $LiBH_4$ clearly reduces the apparent activation energy of $6Mg(NH_2)_2$+9LiH system, while improving reaction kinetics and cycling stability. Increasing the amount of $LiBH_4$ in the composite results in lowering apparent dehydrogenation activation energies (170 kJ·mol$^{-1}H_2$ for $6Mg(NH_2)_2$+9LiH and 129 kJ·mol$^{-1}H_2$ for $6Mg(NH_2)_2$+9LiH+2$LiBH_4$). During the dehydrogenation, reactions between $LiNH_2$ and $LiBH_4$, the formation of $Li_4(BH_4)(NH_2)_3$ leads to a change of the reaction mechanism from interface-controlled to diffusion controlled. Once it is formed, this phase may have positive effect on the mass transport properties in order to form imide phases. During the hydrogenation, the highly ionic conductive phase $Li_4(BH_4)(NH_2)_3$ according to the findings of this work assists

the diffusion of small ions into the interfaces of the amide-hydride matrix. To the best of my knowledge, such intensive analysis regarding the cycling properties and reaction mechanism is performed for the first time. This research provides detailed information about the kinetic behaviour and reaction mechanism on the Li-Mg-B-N-H system and presents $6Mg(NH_2)_2+9LiH+2LiBH_4$ composition (Mg-Li-$2LiBH_4$) as a material with interesting properties for hydrogen storage applications.

The presence of $K_2Mn(NH_2)_4$ positively effects the $Mg(NH_2)_2+2LiH$ (Mg-Li) system, especially during hydrogenation reactions. *In-situ* SR-PXD analysis of 5 mol. % $K_2Mn(NH_2)_4$ added $Mg(NH_2)_2+2LiH$ (Mg-Li-5KMN) in the as-milled state reveals that $K_2Mn(NH_2)_4$ decomposes into Mn_4N and a potassium compound with amorphous or nanocrystalline nature. KH appears during the first dehydrogenation. Once formed, Mn_4N and KH are stable over the investigated 25 cycles. The observed dehydrogenation peak temperature of Mg-Li-5KMN is ~30°C lower than that of Mg-Li. Furthermore, Mg-Li-5KMN has a high and stable hydrogen storage capacity (i.e. 4.2 wt.%). Another interesting feature of this system that emerged during this study is the surprisingly fast rehydrogenation rate at the last stage of the rehydrogenation reaction. Under the applied conditions, hydrogenation of the last 1 wt.% takes place in only 2 minutes, which is four times faster than in the respective Mg-Li-7KH sample ($Mg(NH_2)_2+2LiH+7KH$). These fast reaction rates are preserved in the following three cycles. Further investigations should be made to understand this fast reaction behaviour and the nature of the dual *in-situ* formed additives.

6. Outlook

The results presented in this work shed new light on the role played by selected additives in enhancing the kinetic properties of the system $Mg(NH_2)_2$+LiH. Therefore, the present work enriches existing literature by providing an extensive and thorough study on the kinetic tuning of amide-based systems. Moreover, it constitutes a solid base for future works.

In-situ characterizations via SR-PXD on the K-modified titanate or bimetallic amide containing samples are challenging and they do not provide a complete information on the reaction mechanisms. In fact, this type of experiments requires long exposure times as well as the presence of a sufficient amount of crystalline phases. However, as-milled amide-hydride systems often exhibit fast reaction kinetics and low degree of crystallinity. As an example, team members at Helmholtz–Zentrum Geesthacht had some difficulties with determining the reaction pathway of samples containing-$LiBH_4$, since reaction between $LiNH_2$ and $LiBH_4$ leads to the formation of "liquid-like" amorphous compounds. In order to shed further light on the reaction mechanism of the $Mg(NH_2)_2$+2LiH system, the acquired *in-situ* SR-PXD results have to be complemented with the results obtained by spectroscopy methods, such as X-ray absorption spectroscopy (XAS) or nuclear magnetic resonance (NMR). Additionally, the use of advanced microscopy techniques such as high-resolution transmission electron microscopy (HR-TEM) are powerful while determining the phases responsible for the improved hydrogen properties.

Additional attention should be given to understand the structure of main components, i.e. $Mg(NH_2)_2$, during hydrogen uptake and release reactions. High energy ball milling of $Mg(NH_2)_2$ leads to complete amorphization, whereas during operation it recrystallizes at ~180°C. To the best of my knowledge, very little is known about the impact of $Mg(NH_2)_2$ microstructure on the system behaviour. This challenging task will be addressed in the near future using distribution function (PDF) analysis.

Among the different systems investigated in this work $Mg(NH_2)_2$+LiH+$LiBH_4$ appears to be the most promising system for future applications. In fact, differently from the system containing $K_2Mn(NH_2)_4$ or K-modified $Li_xTi_yO_z$ additives, the system containing $LiBH_4$ possesses stable kinetic properties and tuneable thermodynamic properties. In particular, the possibility to achieve operating conditions, which match those requested for combining the

hydrogen storage system with a PEM fuel cell device, is extremely appealing from the application point of view. Although the possibility for this class of material to operate at temperatures below 100°C is proven [128], further improvements are necessary to achieve suitable reaction kinetics. A further step in the development of this material, in the view of a future application, will be the study of the impact of the material composition in large-scale systems. In fact, although the addition of selected additives sensibly improves the material properties in small to medium size batches, in large size batches, phenomena such as heat transport in the hydride bed and in the storage system (e.g. hydride bed plus tank) might be more relevant in determining the overall system performance. For this reason, a study of the system performance in medium size material batches (1 kg of material) is planned for the near future.

This work broadens the current knowledge on amide-hydride systems and presents a new strategy for developing high performance additives. Variations of the chemical composition of additives greatly influence the reaction kinetics and thermodynamics of amide-hydride systems. Bimetallic amide $K_2Mn(NH_2)_4$ and potassium modified lithium titanate $Li_xTi_yO_z$ accelerates the reaction kinetics of magnesium amide and lithium hydride system, whereas implementing lithium borohydride as additive has a positive impact both on accelerating reaction kinetics and changing thermodynamic properties. *In-situ* formation of highly ionic conductive compounds is expected to have great impact on hydrogen storage properties and investigating the effect of different highly ionic conductive species on amide-hydride systems is a highly interesting research direction for the future.

With the considerations above, the results in this work help the scientific community with the design of new additives for the Li-Mg-N-H system. There is no doubt that fundamental research is very important for understanding the reaction mechanism of amide–hydride systems. Additionally, it is worthy to note that cost calculations and up-scaling process must be taken into account in order to successfully develop amide–hydride systems that are competitive for hydrogen storage applications. In this regard, team members at Helmholtz–Zentrum Geesthacht have already obtained promising results. The research activities will continue by using advanced material preparation and characterization techniques.

Bibliography

[1] IRENA International Renewable Energy Agency, "Renewable power generation costs in 2018," in *SpringerReference*, Berlin/Heidelberg: Springer-Verlag, 2018, p. 160.

[2] IPCC, *Climate Change 2014: Synthesis Report. Contribution of Working Groups I, II and III to the Fifth Assessment Report of the Intergovernmental Panel on Climate Change*. IPCC, Geneva, Switzerland, 2014.

[3] "Effects of Global Warming." [Online]. Available: https://en.wikipedia.org/wiki/Effects_of_global_warming. [Accessed: 26-Nov-2019].

[4] U. Nations, "Paris Agreement," 2015.

[5] IPCC, "Global Warming of 1.5°C," 2018.

[6] S. Kharel and B. Shabani, "Hydrogen as a Long-Term Large-Scale Energy Storage Solution to Support Renewables," *Energies*, vol. 11, no. 10, p. 2825, Oct. 2018.

[7] "Energy density." [Online]. Available: https://en.wikipedia.org/wiki/Energy_density. [Accessed: 14-Jun-2019].

[8] A. Züttel, "Materials for hydrogen storage," *Mater. Today*, vol. 6, no. 9, pp. 24–33, Sep. 2003.

[9] G. Monterey, "Energy requirements for hydrogen gas compression and liquefaction as related to vehicle storage needs," *U.S Dep. Energy*, vol. 25, pp. 1–6, 2009.

[10] N. Sirosh, A. Abele, and A. Niedzwiecki, "Hydrogen Composite Tank Program," in *Proceedings of the 2002 US DOE Hydrogen Program*, 2002, pp. 1–7.

[11] "CTD-materials." [Online]. Available: https://www.ctd-materials.com/engineered-materials/kiboko/. [Accessed: 21-Jun-2019].

[12] Fuel Cells and Hydrogen Joint Undertaking, "Hydrogen Roadmap Europe: A Sustainable Pathway for the European Energy Transition," 2019.

[13] "Liquid hydrogen," *Wikipedia*. [Online]. Available: https://en.wikipedia.org/wiki/Liquid_hydrogen#Uses. [Accessed: 15-Nov-2019].

[14] S. Aceves, G. Berry, J. Martinezfrias, and F. Eespinosalosa, "Vehicular storage of hydrogen in insulated pressure vessels," *Int. J. Hydrogen Energy*, vol. 31, no. 15, pp. 2274–2283, Dec. 2006.

[15] R. K. Ahluwalia, J.-K. Peng, and T. Q. Hua, "Cryo-compressed hydrogen storage," in *Compendium of Hydrogen Energy*, vol. 2, Elsevier, 2016, pp. 119–145.

[16] "Wikipedia." [Online]. Available: https://en.wikipedia.org/wiki/Hydrogen-powered_aircraft. [Accessed: 20-Jun-2019].

[17] G. Petitpas, "Boil-off losses along LH_2 pathway," Livermore CA 94550, 2018.

[18] G. Scherer and E. Newson, "Analysis of the seasonal energy storage of hydrogen in liquid organic hydrides," *Int. J. Hydrogen Energy*, vol. 23, no. 1, pp. 19–25, 1998.

[19] N. Kariya, A. Fukuoka, and M. Ichikawa, "Efficient evolution of hydrogen from liquid cycloalkanes over Pt-containing catalysts supported on active carbons under 'wet–dry multiphase conditions,'" *Appl. Catal. A Gen.*, vol. 233, no. 1–2, pp. 91–102, Jul. 2002.

[20] P. Preuster, C. Papp, and P. Wasserscheid, "Liquid Organic Hydrogen Carriers (LOHCs):

Toward a Hydrogen-free Hydrogen Economy," *Acc. Chem. Res.*, vol. 50, no. 1, pp. 74–85, Jan. 2017.

[21] J. von Wild *et al.*, "Liquid Organic Hydrogen Carriers (LOHC): An auspicious alternative to conventional hydrogen storage technologies," *18th World Hydrog. Energy Conf. 2010*, vol. 78, no. March, pp. 189–197, Jun. 2010.

[22] J. Atilio Puszkiel, "Tailoring the Kinetic Behavior of Hydride Forming Materials for Hydrogen Storage," in *Gold Nanoparticles - Reaching New Heights*, M. Rahman, Ed. Intechopen, 2018.

[23] A. R. Ubbelohde, "Some properties of the metallic state II—Metallic hydrogen and deuterium," *Proc. R. Soc. London. Ser. A - Math. Phys. Sci.*, vol. 159, no. 897, pp. 306–313, Mar. 1937.

[24] A. You, M. A. Y. Be, and I. In, "Hysteresis in the palladium + hydrogen system," *Proc. R. Soc. London. Ser. A. Math. Phys. Sci.*, vol. 259, no. 1298, pp. 341–360, Dec. 1960.

[25] R. B. Schwarz and A. G. Khachaturyan, "Thermodynamics of open two-phase systems with coherent interfaces: Application to metal–hydrogen systems," *Acta Mater.*, vol. 54, no. 2, pp. 313–323, Jan. 2006.

[26] P. J. Cappillino, E. J. Lavernia, M. D. Ong, W. G. Wolfer, and N. Y. Yang, "Plastic deformation and hysteresis for hydrogen storage in Pd–Rh alloys," *J. Alloys Compd.*, vol. 586, pp. 59–65, Feb. 2014.

[27] T. B. Flanagan, C. N. Park, and D. H. Everett, "Hysteresis in metal hydrides: An illustration of entropy production," *J. Chem. Educ.*, vol. 64, no. 11, p. 944, Nov. 1987.

[28] A. Züttel, A. Borgschulte, and L. Schlapbach, *Hydrogen as a Future Energy Carrier*. WILEY-VCH Verlag GmbH & Co. KGaA, Weinheim, 2008.

[29] G. Walker, *Solid-State Hydrogen Storage, materials and chemistry*, 1st Edit. Woodhead Publishing, 2008.

[30] G. Sandrock, "A panoramic overview of hydrogen storage alloys from a gas reaction point of view," *J. Alloys Compd.*, vol. 293–295, pp. 877–888, 1999.

[31] K. Zeng, "Critical assessment and thermodynamic modeling of the Mg–H system," *Int. J. Hydrogen Energy*, vol. 24, no. 10, pp. 989–1004, Oct. 1999.

[32] M. Schwickardi and B. Bogdanovic, "Ti-doped alkali metal aluminium hydrides as potential novel reversible hydrogen storage materials," *J. Alloys Compd.*, vol. 254, pp. 1–9, 1997.

[33] P. Chen, Z. Xiong, J. Luo, J. Lin, and K. Lee Tan, "Interaction of hydrogen with metal nitrides and imides," *Nature*, vol. 420, no. 6913, pp. 302–304, 2002.

[34] S. Orimo, Y. Nakamori, J. R. Eliseo, A. Züttel, and C. M. Jensen, "Complex Hydrides for Hydrogen Storage," *Chem. Rev.*, vol. 107, no. 10, pp. 4111–4132, 2007.

[35] H. W. Li *et al.*, "Dehydriding and rehydriding processes of well-crystallized $Mg(BH_4)_2$ accompanying with formation of intermediate compounds," *Acta Mater.*, vol. 56, no. 6, pp. 1342–1347, 2008.

[36] P. Mauron *et al.*, "Stability and reversibility of $LiBH_4$," *J. Phys. Chem. B*, vol. 112, no. 3, pp. 906–910, 2008.

[37] S. Cahen, J. B. Eymery, R. Janot, and J. M. Tarascon, "Improvement of the $LiBH_4$ hydrogen desorption by inclusion into mesoporous carbons," *J. Power Sources*, vol. 189, no. 2, pp. 902–908, 2009.

[38] R. D. Stephens, A. F. Gross, S. L. Van Atta, J. J. Vajo, and F. E. Pinkerton, "The kinetic enhancement of hydrogen cycling in $NaAlH_4$ by melt infusion into nanoporous carbon aerogel,"

Nanotechnology, vol. 20, no. 20, 2009.

[39] P. Adelhelm and P. E. De Jongh, "The impact of carbon materials on the hydrogen storage properties of light metal hydrides," *J. Mater. Chem.*, vol. 21, no. 8, pp. 2417–2427, 2011.

[40] M. Dornheim, "Thermodynamics of Metal Hydrides: Tailoring Reaction Enthalpies of Hydrogen Storage Materials," in *Thermodynamics - Interaction Studies - Solids, Liquids and Gases*, InTech, 2011.

[41] J. J. Vajo, F. Mertens, C. C. Ahn, R. C. Bowman, and B. Fultz, "Altering Hydrogen Storage Properties by Hydride Destabilization through Alloy Formation: LiH and MgH_2 Destabilized with Si," *J. Phys. Chem. B*, vol. 108, no. 37, pp. 13977–13983, Sep. 2004.

[42] G. Barkhordarian, T. Klassen, M. Dornheim, and R. Bormann, "Unexpected kinetic effect of MgB_2 in reactive hydride composites containing complex borohydrides," *J. Alloys Compd.*, vol. 440, no. 1–2, pp. 18–21, 2007.

[43] J. J. Reilly and R. H. Wiswall, "Reaction of Hydrogen with Alloys of Magnesium and Copper," *Inorg. Chem.*, vol. 6, no. 12, pp. 2220–2223, 1967.

[44] H. Shao, M. Felderhoff, F. Schüth, and C. Weidenthaler, "Nanostructured Ti-catalyzed MgH_2 for hydrogen storage," *Nanotechnology*, vol. 22, no. 23, 2011.

[45] J. J. Vajo, S. L. Skeith, and F. Mertens, "Reversible storage of hydrogen in destabilized $LiBH_4$," *J. Phys. Chem. B*, vol. 109, no. 9, pp. 3719–3722, 2005.

[46] W. Luo and E. Rönnebro, "Towards a viable hydrogen storage system for transportation application," *J. Alloys Compd.*, vol. 404–406, pp. 392–395, 2005.

[47] H. Y. Leng, T. Ichikawa, S. Hino, N. Hanada, S. Isobe, and H. Fujii, "New Metal−N−H System Composed of $Mg(NH_2)_2$ and LiH for Hydrogen Storage," *J. Phys. Chem. B*, vol. 108, no. 26, pp. 8763–8765, Jul. 2004.

[48] Z. Xiong, G. Wu, J. Hu, and P. Chen, "Ternary Imides for Hydrogen Storage," *Adv. Mater.*, vol. 16, no. 17, pp. 1522–1525, Sep. 2004.

[49] Z. Xiong *et al.*, "Reversible Hydrogen Storage by a Li-Al-N-H Complex," *Adv. Funct. Mater.*, vol. 17, no. 7, pp. 1137–1142, May 2007.

[50] J. Hu, Y. Liu, G. Wu, Z. Xiong, and P. Chen, "Structural and Compositional Changes during Hydrogenation/Dehydrogenation of the Li−Mg−N−H System," *J. Phys. Chem. C*, vol. 111, no. 49, pp. 18439–18443, Dec. 2007.

[51] J. Wang *et al.*, "Potassium-Modified $Mg(NH_2)_2$/2LiH System for Hydrogen Storage," *Angew. Chemie Int. Ed.*, vol. 48, no. 32, pp. 5828–5832, Jul. 2009.

[52] Z. Xiong *et al.*, "Thermodynamic and kinetic investigations of the hydrogen storage in the Li-Mg-N-H system," *J. Alloys Compd.*, vol. 398, pp. 235–239, 2005.

[53] W. Luo and S. Sickafoose, "Thermodynamic and structural characterization of the Mg-Li-N-H hydrogen storage system," *J. Alloys Compd.*, vol. 407, pp. 274–281, 2006.

[54] J. Wang, H. Li, S. Wang, X. Liu, Y. Li, and L. Jiang, "The desorption kinetics of the $Mg(NH_2)_2$+LiH mixture," *Int. J. Hydrogen Energy*, vol. 34, no. 3, pp. 1411–1416, Feb. 2009.

[55] Y. Liu, K. Zhon, K. Luo, M. Gao, H. Pan, and Q. Wang, "Size-dependent kinetic enhancement in hydrogen absorption and desorption of the Li-Mg-N-H system," *J. Am. Chem. Soc.*, vol. 131, no. 5, pp. 1862–1870, 2009.

[56] S. Nayebossadri, "Kinetic rate-limiting steps in dehydrogenation of Li-N-H and Li-Mg-N-H systems - Effects of elemental Si and Al," *Int. J. Hydrogen Energy*, vol. 36, no. 14, pp. 8335–

8343, 2011.

[57] G. Gizer *et al.*, “Tuning the reaction mechanism and hydrogenation/dehydrogenation properties of 6$Mg(NH_2)_2$-9LiH system by adding LiBH4,” *Int. J. Hydrogen Energy*, vol. 44, no. 23, pp. 11920–11929, May 2019.

[58] L. Xie, Y. Li, R. Yang, Y. Liu, and X. Li, “Superior hydrogen desorption kinetics of $Mg(NH_2)_2$ hollow nanospheres mixed with MgH_2 nanoparticles,” *Appl. Phys. Lett.*, vol. 92, no. 85, pp. 231910–123921, 2008.

[59] P. E. de Jongh, M. Allendorf, J. J. Vajo, and C. Zlotea, “Nanoconfined light metal hydrides for reversible hydrogen storage,” *MRS Bull.*, vol. 38, no. 6, pp. 488–494, Jun. 2013.

[60] U. Ulmer, J. Hu, M. Franzreb, and M. Fichtner, “Preparation, scale-up and testing of nanoscale, doped amide systems for hydrogen storage,” *Int. J. Hydrogen Energy*, 2013.

[61] H. Cao *et al.*, “Improved kinetics of the $Mg(NH_2)_2$-2LiH system by addition of lithium halides,” *RSC Adv.*, vol. 4, no. 61, pp. 32555–32561, 2014.

[62] C. Liang *et al.*, “Enhanced dehydrogenation/hydrogenation kinetics of the $Mg(NH_2)_2$-2LiH system with NaOH additive,” *Int. J. Hydrogen Energy*, vol. 36, no. 3, pp. 2137–2144, 2011.

[63] J. Hu, A. Pohl, S. Wang, J. Rothe, and M. Fichtner, “Additive Effects of $LiBH_4$ and $ZrCoH_3$ on the Hydrogen Sorption of the Li-Mg-N-H Hydrogen Storage System,” *J. Phys. Chem. C*, vol. 116, no. 38, pp. 20246–20253, 2012.

[64] T. Durojaiye, J. Hayes, and A. Goudy, “Rubidium hydride: An exceptional dehydrogenation catalyst for the lithium amide/magnesium hydride system,” *J. Phys. Chem. C*, vol. 117, no. 13, pp. 6554–6560, 2013.

[65] G. Gizer *et al.*, “Enhancement Effect of Bimetallic Amide $K_2Mn(NH_2)_4$ and In-Situ Formed KH and Mn_4N on the Dehydrogenation/Hydrogenation Properties of Li–Mg–N–H System,” *Energies*, vol. 12, no. 14, p. 2779, Jul. 2019.

[66] J. Wang *et al.*, “Solid-solid heterogeneous catalysis: The role of potassium in promoting the dehydrogenation of the $Mg(NH_2)_2$/2LiH composite,” *ChemSusChem*, vol. 6, no. 11, pp. 2181–2189, 2013.

[67] C. Li, Y. Liu, Y. Pang, Y. Gu, M. Gao, and H. Pan, “Compositional effects on the hydrogen storage properties of $Mg(NH_2)_2$-2LiH-xKH and the activity of KH during dehydrogenation reactions,” *Dalt. Trans.*, vol. 43, no. 6, pp. 2369–2377, 2014.

[68] C. Li, Y. Liu, Y. Yang, M. Gao, and H. Pan, “High-temperature failure behaviour and mechanism of K-based additives in Li-Mg-N-H hydrogen storage systems,” *J. Mater. Chem. A*, vol. 2, no. 20, pp. 7345–7353, 2014.

[69] J. A. Puszkiel *et al.*, “A novel catalytic route for hydrogenation-dehydrogenation of 2LiH + MgB_2: Via in situ formed core-shell $LixTiO_2$ nanoparticles,” *J. Mater. Chem. A*, vol. 5, no. 25, pp. 12922–12933, 2017.

[70] H. Cao, G. Wu, Y. Zhang, Z. Xiong, J. Qiu, and P. Chen, “Effective thermodynamic alteration to $Mg(NH_2)_2$-LiH system: Achieving near ambient-temperature hydrogen storage,” *J. Mater. Chem. A*, vol. 2, no. 38, pp. 15816–15822, 2014.

[71] J. Hu, Y. Liu, G. Wu, Z. Xiong, Y. S. Chua, and P. Chen, “Improvement of Hydrogen Storage Properties of the Li–Mg–N–H System by Addition of $LiBH_4$,” *Chem. Mater.*, vol. 20, no. 13, pp. 4398–4402, Jul. 2008.

[72] H. Cao *et al.*, “New synthesis route for ternary transition metal amides as well as ultrafast amide–hydride hydrogen storage materials,” *Chem. Commun.*, vol. 52, no. 29, pp. 5100–5103, 2016.

[73] H. Cao *et al.*, “Ternary Amides Containing Transition Metals for Hydrogen Storage: A Case Study with Alkali Metal Amidozincates,” *ChemSusChem*, vol. 8, no. 22, pp. 3777–3782, Nov. 2015.

[74] H. Cao *et al.*, “In Situ X-ray Diffraction Studies on the De/rehydrogenation Processes of the K 2 [Zn(NH 2) 4]-8LiH System,” *J. Phys. Chem. C*, vol. 121, no. 3, pp. 1546–1551, Jan. 2017.

[75] S. Doppiu, L. Schultz, and O. Gutfleisch, “In situ pressure and temperature monitoring during the conversion of Mg into MgH_2 by high-pressure reactive ball milling,” *J. Alloys Compd.*, vol. 427, no. 1–2, pp. 204–208, Jan. 2007.

[76] J. H. Sharp, G. W. Brindley, and B. N. N. Achar, “Numerical Data for Some Commonly Used Solid State Reaction Equations,” *J. Am. Ceram. Soc.*, vol. 49, no. 7, pp. 379-, 1966.

[77] L. F. Jones, D. Dollimore, and T. Nicklin, “Comparison of experimental kinetic decomposition data with master data using a linear plot method,” *Thermochim. Acta*, vol. 13, no. 2, pp. 240–245, 1975.

[78] T. Ozawa, “Kinetic analysis by repeated temperature scanning. Part 1. Theory and methods,” *Thermochim. Acta*, vol. 356, no. 1–2, pp. 173–180, 2000.

[79] H. E. Kissinger, “Reaction Kinetics in Differential Thermal Analysis,” *Anal. Chem.*, vol. 29, no. 11, pp. 1702–1706, 1957.

[80] P. M. Madhusudanan, K. Krishnan, and K. N. Ninan, “New approximation for the p(x) function in the evaluation of non-isothermal kinetic data,” *Thermochim. Acta*, vol. 97, no. C, pp. 189–201, 1986.

[81] Rühl, S. Inorganic Crystal Structure Database (ICSD), A Focus on Crystallography, edited H. Müller, FIZ Karlsruhe, 6–10 (2015).

[82] Y. Cerenius *et al.*, “The crystallography beamline I711 at MAX II,” *J. Synchrotron Radiat.*, vol. 7, no. 4, pp. 203–208, 2000.

[83] H. M. Rietveld, “A profile refinement method for nuclear and magnetic structures,” *J. Appl. Crystallogr.*, vol. 2, pp. 65–71, 1968.

[84] L. Lutterotti, “Total pattern fitting for the combined size-strain-stress-texture determination in thin film diffraction,” *Nucl. Instruments Methods Phys. Res. Sect. B Beam Interact. with Mater. Atoms*, vol. 268, no. 3–4, pp. 334–340, 2010.

[85] U. Bösenberg *et al.*, “Characterization of metal hydrides by in-situ XRD,” *Int. J. Hydrogen Energy*, vol. 39, no. 18, pp. 9899–9903, 2014.

[86] C. Pistidda *et al.*, “First direct study of the ammonolysis reaction in the most common alkaline and alkaline earth metal hydrides by in situ SR-PXD,” *J. Phys. Chem. C*, vol. 119, no. 2, pp. 934–943, 2015.

[87] A. P. Hammersley, “FIT2D: An Introduction and Overview ESRF Internal Report,” *ESRF Intern. Rep.*, 1997.

[88] “XAFSmass, Freeware. Available online: www.cells.es/Beamlines/CLAESS/software/xafsmass.html (accessed on 11 October 2018),” no. October, p. 2018, 2018.

[89] B. Ravel and M. Newville, “ATHENA, ARTEMIS, HEPHAESTUS: data analysis for X-ray absorption spectroscopy using IFEFFIT,” *J Synchrotron Radiat*, pp. 1–16, 2005.

[90] G. Gizer *et al.*, “Improved kinetic behaviour of $Mg(NH_2)_2$-2LiH doped with nanostructured K-modified-$Li_xTi_yO_z$ for hydrogen storage,” *Sci. Rep.*, vol. 10, no. 1, p. 8, Jan. 2020.

[91] R. Janot, J. B. Eymery, and J. M. Tarascon, “Investigation of the processes for reversible hydrogen storage in the Li-Mg-N-H system,” *J. Power Sources*, vol. 164, no. 2, pp. 496–502, 2007.

[92] R. Parviz and R. A. Varin, “Combined effects of molar ratio and ball milling energy on the phase transformations and mechanical dehydrogenation in the lithium amide-magnesium hydride ($LiNH_2$ + $nMgH_2$)(n = 0.5–2.0) nanocomposites,” *Int. J. Hydrogen Energy*, vol. 38, no. 20, pp. 8313–8327, Jul. 2013.

[93] V. G. Linde and R. Juza, “IR-Spektren von Amiden und lmiden zwei- und dreiwertiger Metalle gestellt ; wenn das Praparat bisher noch nicht untersucht worden ist , werden,” *Z. Anorg. Allg. Chem.*, vol. 409, pp. 199–214, 1974.

[94] H. Leng, T. Ichikawa, and H. Fujii, “Hydrogen Storage Properties of Li−Mg−N−H Systems with Different Ratios of LiH/$Mg(NH_2)_2$,” *J. Phys. Chem. B*, vol. 110, no. 26, pp. 12964–12968, Jul. 2006.

[95] M. Drillon, J. M. Heintz, J. P. Kappler, E. Beaurepaire, and O. Durmeyer, “TiK XANES in superconducting $LiTi_2O_4$ and related compounds,” *J. Phys. Condens. Matter*, vol. 2, no. 28, pp. 6127–6136, 2002.

[96] J. Hu, E. Weidner, M. Hoelzel, and M. Fichtner, “Functions of $LiBH_4$ in the hydrogen sorption reactions of the 2LiH–$Mg(NH_2)_2$ system,” *Dalt. Trans.*, vol. 39, no. 38, p. 9100, 2010.

[97] A. Züttel *et al.*, “Hydrogen storage properties of $LiBH_4$,” *J. Alloys Compd.*, vol. 356–357, pp. 515–520, Aug. 2003.

[98] L. Xie, Y. Liu, G. Li, and X. Li, “Improving Hydrogen Sorption Kinetics of the $Mg(NH_2)_2$−LiH System by the Tuning Particle Size of the Amide,” *J. Phys. Chem. C*, vol. 113, no. 32, pp. 14523–14527, Aug. 2009.

[99] H. Wang *et al.*, “Effects of Stoichiometry on the H_2-Storage Properties of $Mg(NH_2)_2$-LiH-$LiBH_4$ Tri-Component Systems,” *Chem. - An Asian J.*, vol. 12, no. 14, pp. 1758–1764, Jul. 2017.

[100] Z. Xiong, G. Wu, J. Hu, P. Chen, W. Luo, and J. Wang, “Investigations on hydrogen storage over Li–Mg–N–H complex—the effect of compositional changes,” *J. Alloys Compd.*, vol. 417, no. 1–2, pp. 190–194, Jun. 2006.

[101] S. Isobe, T. Ichikawa, H. Leng, H. Fujii, and Y. Kojima, “Hydrogen desorption processes in Li–Mg–N–H systems,” *J. Phys. Chem. Solids*, vol. 69, no. 9, pp. 2234–2236, Sep. 2008.

[102] Y. Pang and Q. Li, “A review on kinetic models and corresponding analysis methods for hydrogen storage materials,” *Int. J. Hydrogen Energy*, vol. 41, no. 40, pp. 18072–18087, Oct. 2016.

[103] G. Amica, S. Enzo, P. A. Larochette, and F. C. Gennari, “Improvements in the hydrogen storage properties of the $Mg(NH_2)_2$–LiH composite by KOH addition,” *Phys. Chem. Chem. Phys.*, vol. 20, no. 22, pp. 15358–15367, 2018.

[104] Y. Liu, C. Li, B. Li, M. Gao, and H. Pan, “Metathesis Reaction-Induced Significant Improvement in Hydrogen Storage Properties of the KF-Added $Mg(NH_2)_2$–2LiH System,” *J. Phys. Chem. C*, vol. 117, no. 2, pp. 866–875, Jan. 2013.

[105] F. Torre *et al.*, “Kinetic improvement on the CaH_2-catalyzed $Mg(NH_2)_2$ + 2LiH system,” *J. Alloys Compd.*, vol. 645, no. S1, pp. S284–S287, Oct. 2015.

[106] L.-P. Ma *et al.*, “Catalytically Enhanced Hydrogen Storage Properties of $Mg(NH_2)_2$ + 2LiH Material by Graphite-Supported Ru Nanoparticles,” *J. Phys. Chem. C*, vol. 112, no. 46, pp. 18280–18285, Nov. 2008.

[107] W. Luo, V. Stavila, and L. E. Klebanoff, “New insights into the mechanism of activation and

hydrogen absorption of ($2LiNH_2$–MgH_2),” *Int. J. Hydrogen Energy*, vol. 37, no. 8, pp. 6646–6652, Apr. 2012.

[108] J. Wang *et al.*, “Effects of triphenyl phosphate on the hydrogen storage performance of the $Mg(NH_2)_2$–2LiH system,” *J. Mater. Chem.*, vol. 19, no. 15, p. 2141, 2009.

[109] B. X. Dong, L. Song, J. Ge, Y. L. Teng, and S. Y. Zhang, “The ternary amide KLi3(NH2)4: An important intermediate in the potassium compound-added Li-N-H systems,” *RSC Adv.*, 2014.

[110] W. Luo, V. Stavila, and L. E. Klebanoff, “New insights into the mechanism of activation and hydrogen absorption of (2LiNH2–MgH2),” *Int. J. Hydrogen Energy*, vol. 37, no. 8, pp. 6646–6652, Apr. 2012.

[111] P. Chen, Z. Xiong, L. Yang, G. Wu, and W. Luo, “Mechanistic Investigations on the Heterogeneous Solid-State Reaction of Magnesium Amides and Lithium Hydrides,” *J. Phys. Chem. B*, vol. 110, no. 29, pp. 14221–14225, Jul. 2006.

[112] B. Li, Y. Liu, J. Gu, Y. Gu, M. Gao, and H. Pan, “Mechanistic investigations on significantly improved hydrogen storage performance of the $Ca(BH_4)_2$-added $2LiNH_2/MgH_2$ system,” *Int. J. Hydrogen Energy*, vol. 38, no. 12, pp. 5030–5038, Apr. 2013.

[113] H. Pan, S. Shi, Y. Liu, B. Li, Y. Yang, and M. Gao, “Improved hydrogen storage kinetics of the Li–Mg–N–H system by addition of $Mg(BH_4)_2$,” *Dalt. Trans.*, vol. 42, no. 11, pp. 3802–3811, 2013.

[114] H. Wang, H. Cao, G. Wu, T. He, and P. Chen, “The improved Hydrogen Storage Performances of the Multi-Component Composite: $2Mg(NH_2)_2$–3LiH–$LiBH_4$,” *Energies*, vol. 8, no. 7, pp. 6898–6909, Jul. 2015.

[115] G. J. Lewis *et al.*, “High throughput screening of the ternary $LiNH_2$–MgH_2–$LiBH_4$ phase diagram,” *J. Alloys Compd.*, vol. 446–447, pp. 355–359, Oct. 2007.

[116] G. P. Meisner, M. L. Scullin, M. P. Balogh, F. E. Pinkerton, and M. S. Meyer, “Hydrogen Release from Mixtures of Lithium Borohydride and Lithium Amide: A Phase Diagram Study,” *J. Phys. Chem. B*, vol. 110, no. 9, pp. 4186–4192, Mar. 2006.

[117] M. Matsuo *et al.*, “Complex Hydrides with $(BH_4)^-$ and $(NH_2)^-$ Anions as New Lithium Fast-Ion Conductors,” *J. Am. Chem. Soc.*, vol. 131, no. 45, pp. 16389–16391, Nov. 2009.

[118] M. Y. Yan *et al.*, “Experimental study on hydrogen storage properties of Li–Mg–N–H based tank,” *J. Alloys Compd.*, vol. 603, pp. 19–22, Aug. 2014.

[119] N. Z. Abd.Khalim Khafidz, Z. Yaakob, K. L. Lim, and S. N. Timmiati, “The kinetics of lightweight solid-state hydrogen storage materials: A review,” *Int. J. Hydrogen Energy*, vol. 41, no. 30, pp. 13131–13151, Aug. 2016.

[120] L.-P. Ma, P. Wang, H.-B. Dai, and H.-M. Cheng, “Catalytically enhanced dehydrogenation of Li–Mg–N–H hydrogen storage material by transition metal nitrides,” *J. Alloys Compd.*, vol. 468, no. 1–2, pp. L21–L24, Jan. 2009.

[121] P. Wang *et al.*, “Breaking scaling relations to achieve low-temperature ammonia synthesis through LiH-mediated nitrogen transfer and hydrogenation,” *Nat. Chem.*, vol. 9, no. 1, pp. 64–70, Jan. 2017.

[122] B. Bogdanović, A. Ritter, and B. Spliethoff, “Active MgH_2-Mg Systems for Reversible Chemical Energy Storage,” *Angew. Chemie Int. Ed. English*, vol. 29, no. 3, pp. 223–234, Mar. 1990.

[123] G. Capurso *et al.*, “Metal Hydride-Based Hydrogen Storage Tank Coupled with an Urban Concept Fuel Cell Vehicle: Off Board Tests,” *Adv. Sustain. Syst.*, vol. 2, no. 6, p. 1800004, Jun. 2018.

[124] M. Baricco *et al.*, “SSH2S: Hydrogen storage in complex hydrides for an auxiliary power unit based on high temperature proton exchange membrane fuel cells,” *J. Power Sources*, vol. 342, pp. 853–860, Feb. 2017.

[125] C. Li, Y. Liu, Y. Yang, M. Gao, and H. Pan, “High-temperature failure behaviour and mechanism of K-based additives in Li–Mg–N–H hydrogen storage systems,” *J. Mater. Chem. A*, vol. 2, no. 20, pp. 7345–7353, 2014.

[126] Y. Liu, Y. Yang, X. Zhang, Y. Li, M. Gao, and H. Pan, “Insights into the dehydrogenation reaction process of a K-containing $Mg(NH_2)_2$–2LiH system,” *Dalt. Trans.*, vol. 44, no. 41, pp. 18012–18018, 2015.

[127] T. Durojaiye, J. Hayes, and A. Goudy, “Potassium, rubidium and cesium hydrides as dehydrogenation catalysts for the lithium amide/magnesium hydride system,” *Int. J. Hydrogen Energy*, vol. 40, no. 5, pp. 2266–2273, Feb. 2015.

[128] H. Wang *et al.*, “Near Ambient Condition Hydrogen Storage in a Synergized Tricomponent Hydride System,” *Adv. Energy Mater.*, vol. 7, no. 13, p. 1602456, Jul. 2017.

Appendix

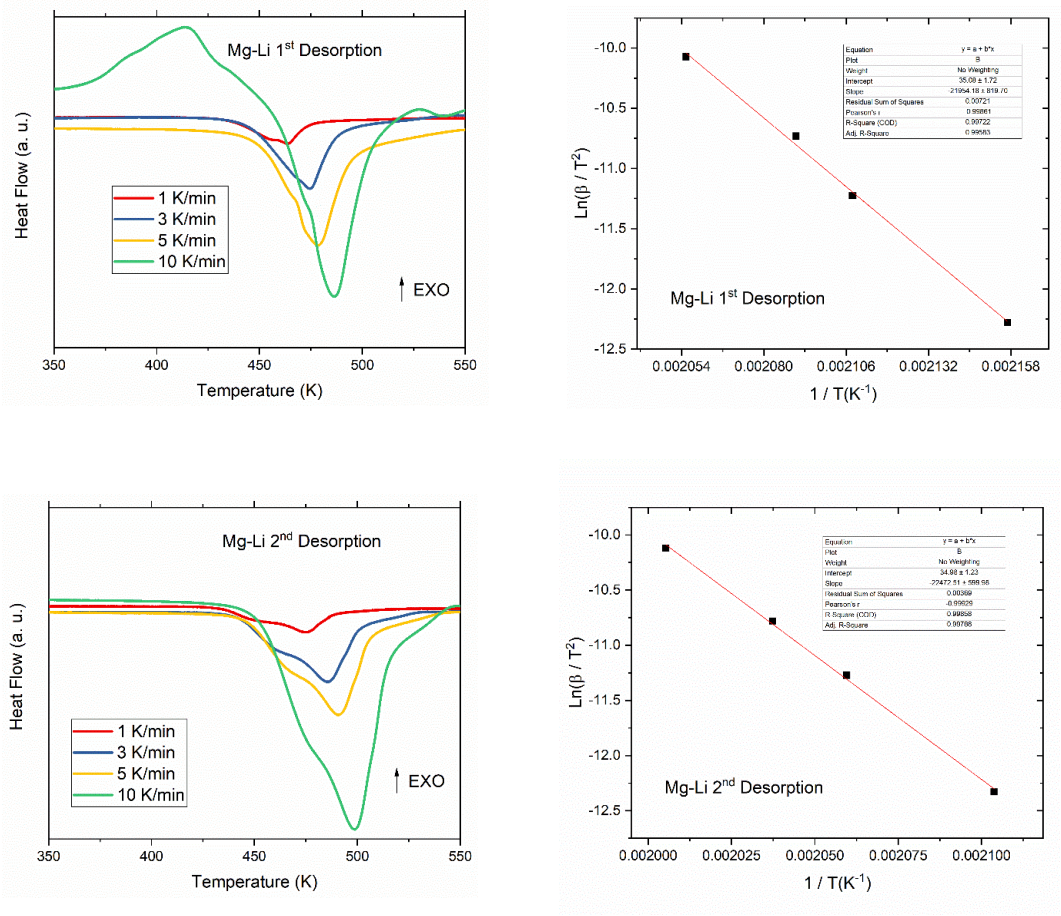

Figure A1 DSC and corresponding Arrhenius plots of Mg-Li ($Mg(NH_2)_2$+2LiH) at the 1st and 2nd desorption

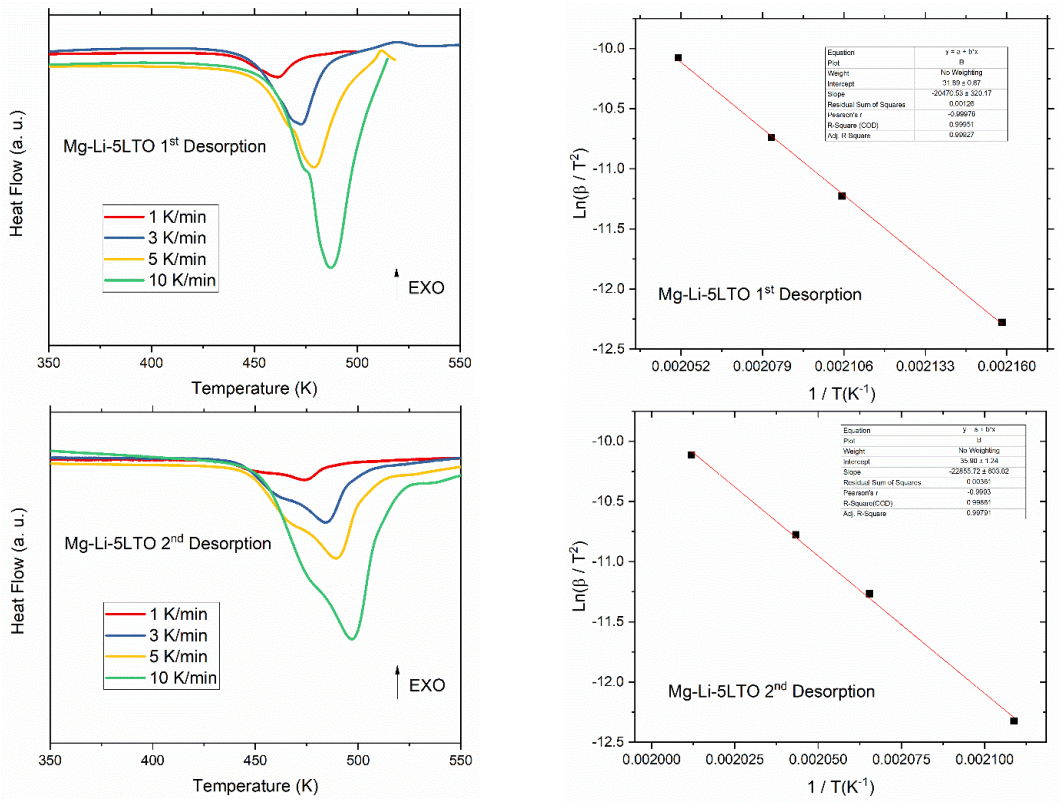

Figure A2 DSC and corresponding Arrhenius plots of Mg-Li-5LTO at the 1st and 2nd desorption

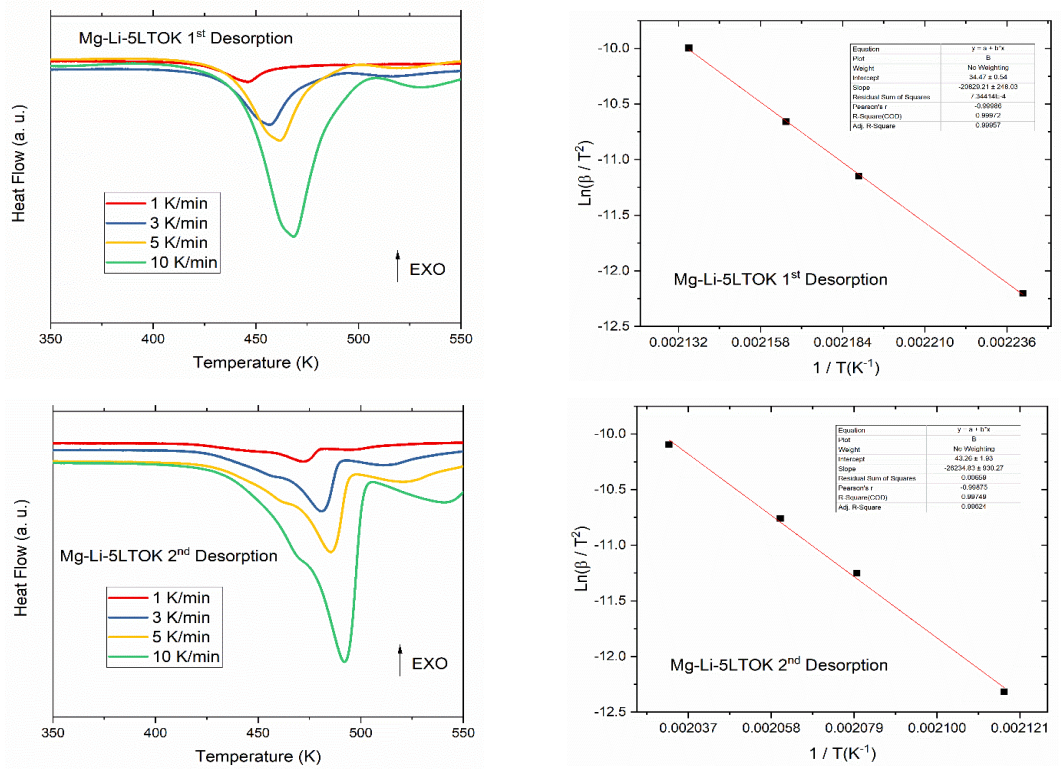

Figure A3 DSC and corresponding Arrhenius plots of Mg-Li-5LTOK at the 1st and 2nd desorption

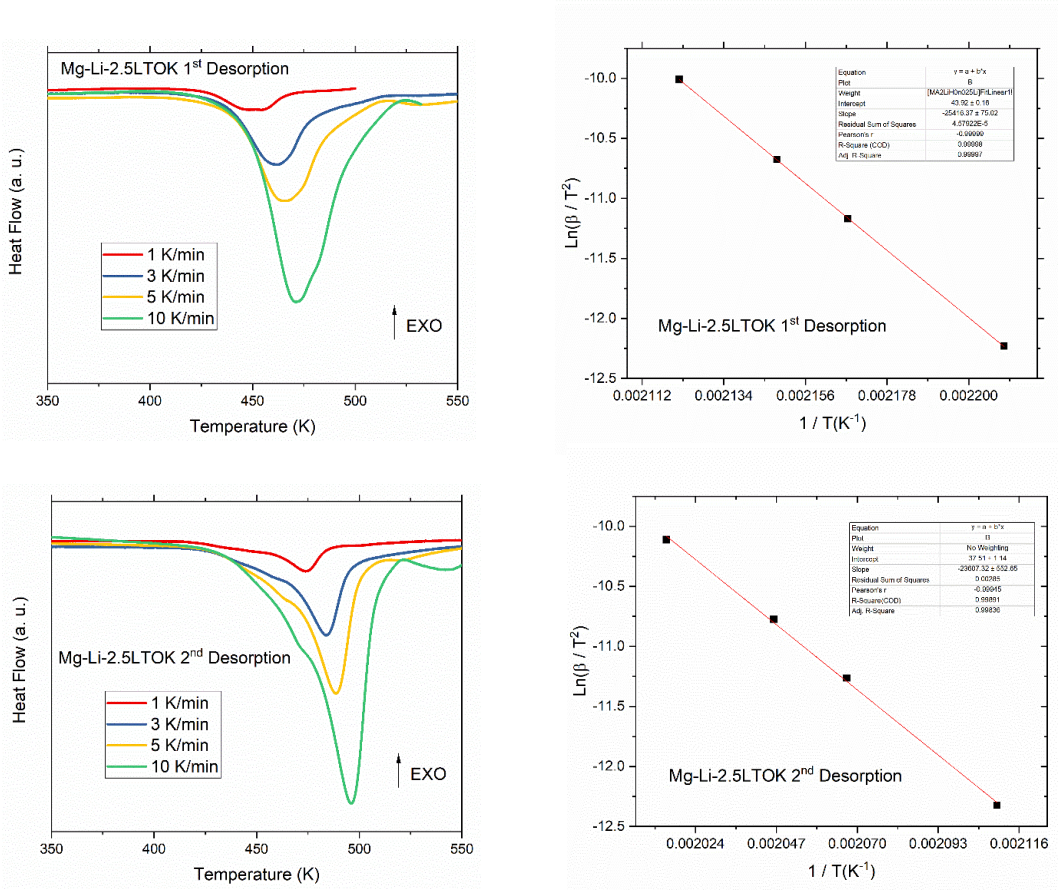

Figure A4 DSC and corresponding Arrhenius plots of Mg-Li-2.5LTOK at the 1st and 2nd desorption

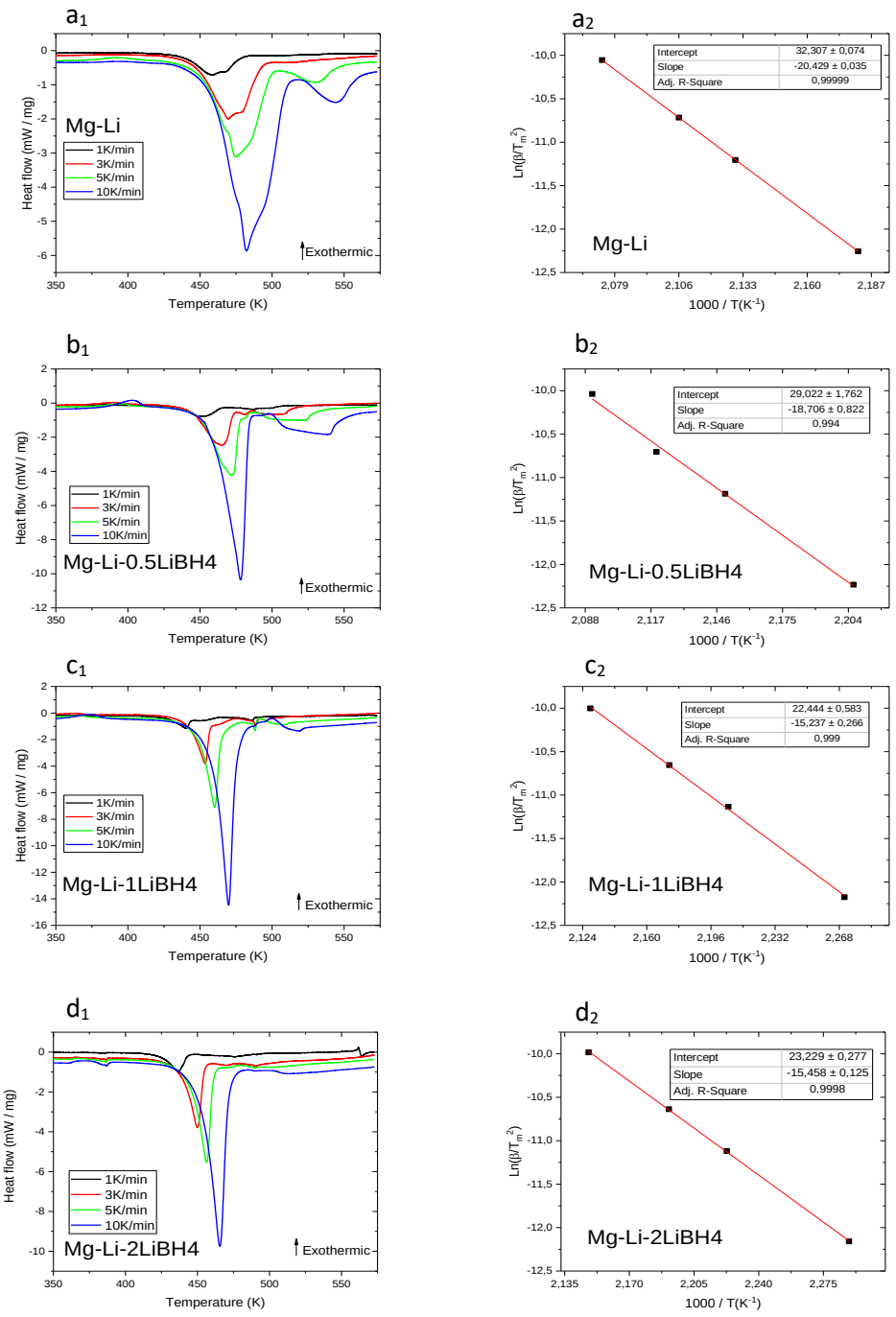

Figure A5 DSC curves of as-milled samples (a_1-d_1) and corresponding Kissinger plots (a_2-d_2)

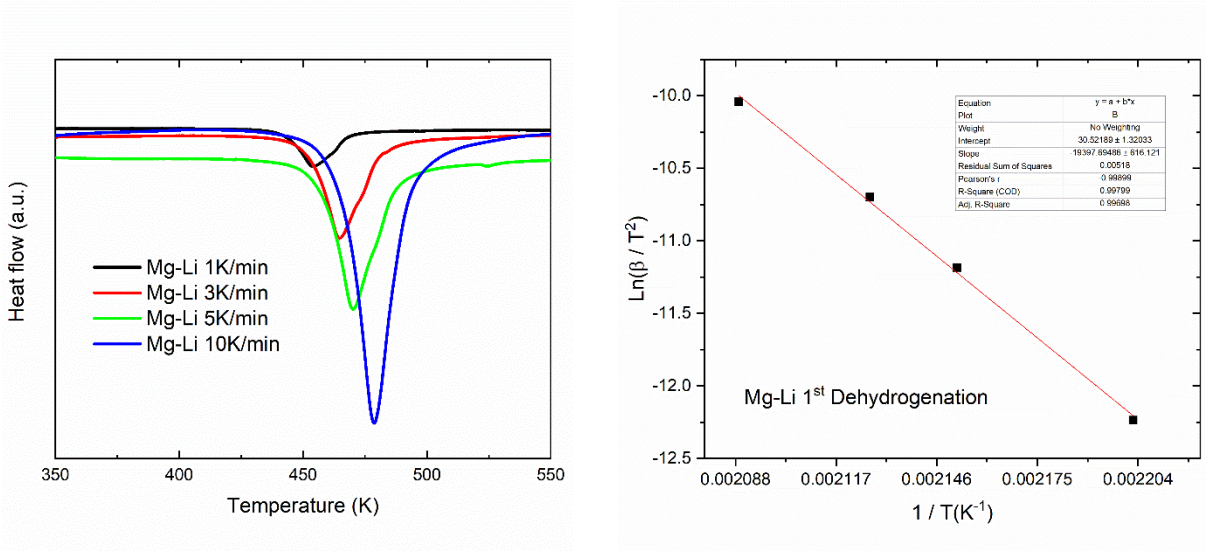

Figure A6 DSC and corresponding Arrhenius plots of Mg-Li ($Mg(NH_2)_2$+2LiH) at the 1st dehydrogenation

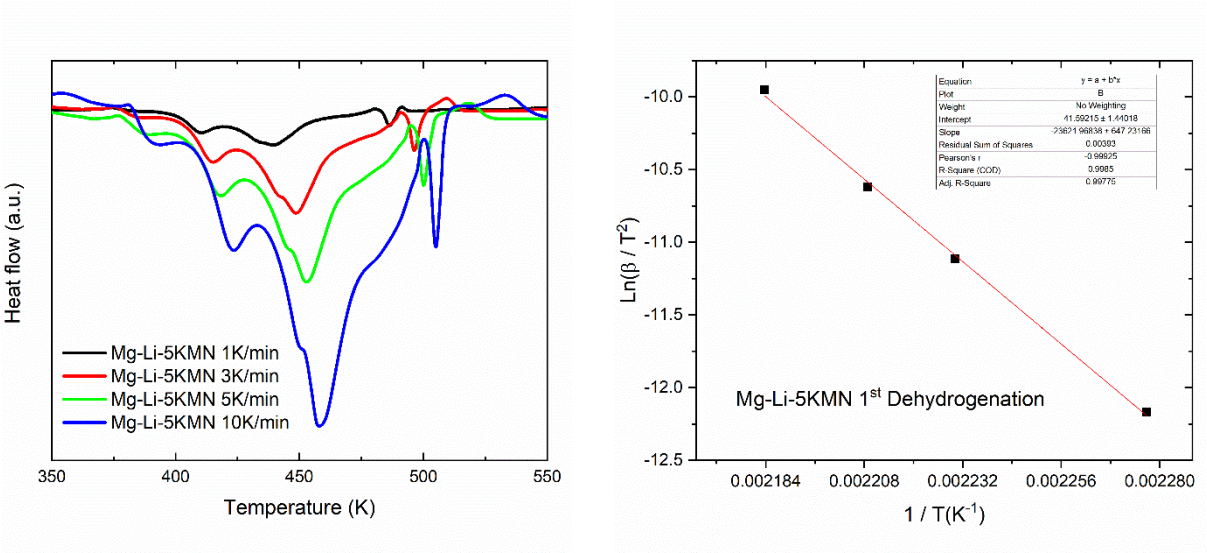

Figure A7 DSC and corresponding Arrhenius plots of Mg-Li-5KMN at the 1st dehydrogenation

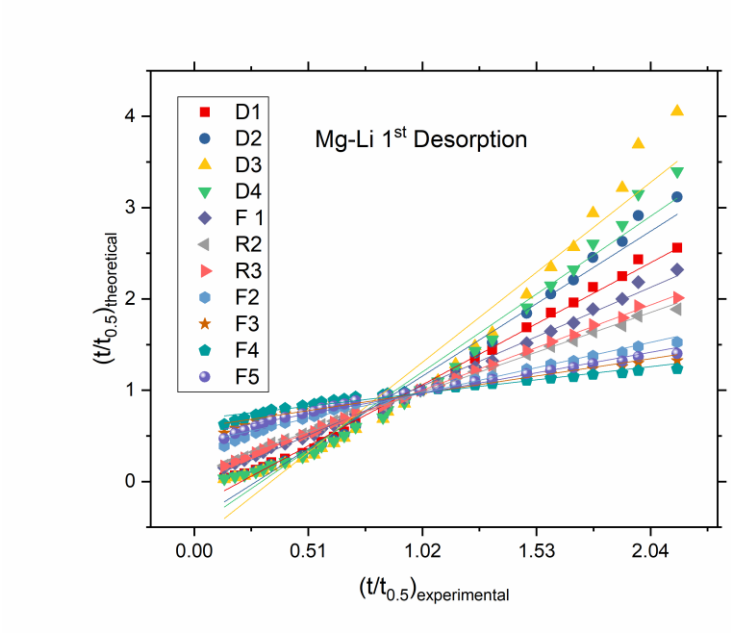

Figure A8 $(t/t_{0.5})_{experimental}$ vs. $(t/t_{0.5})_{theoretical}$ plot for sample Mg-Li $(Mg(NH_2)_2+2LiH)$ at 1st desorption

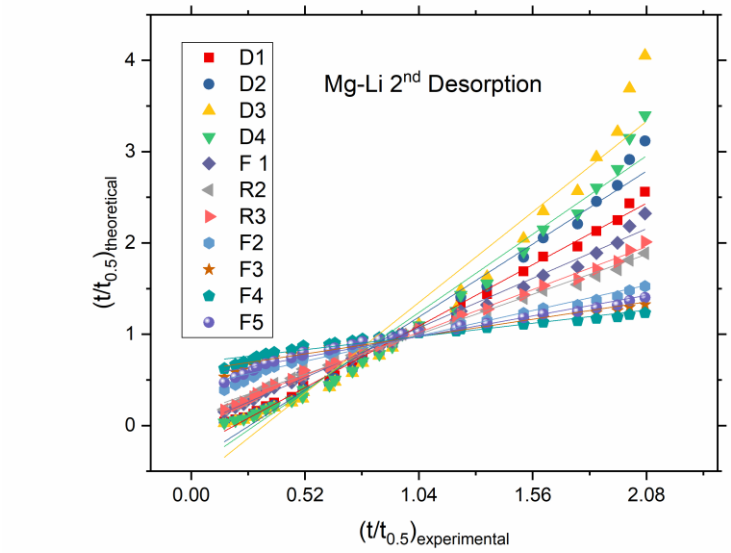

Figure A9 − $(t/t_{0.5})_{experimental}$ vs. $(t/t_{0.5})_{theoretical}$ plot for sample Mg-Li $(Mg(NH_2)_2+2LiH)$ at 2nd desorption

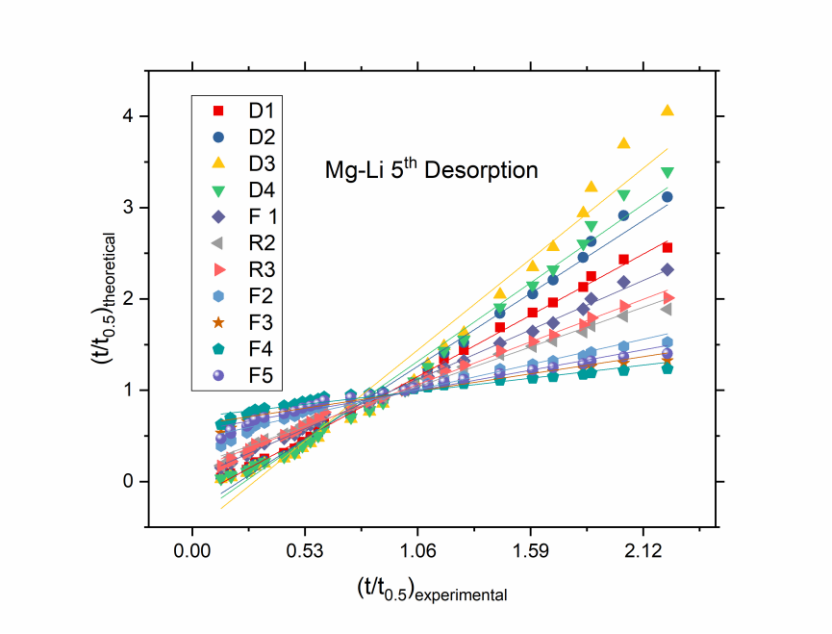

Figure A10 $(t/t_{0.5})_{experimental}$ vs. $(t/t_{0.5})_{theoretical}$ plot for sample Mg-Li ($Mg(NH_2)_2$+2LiH) at 5th desorption

Table A1 Fitting results for the desorption curves of Mg-Li material.

$Mg(NH_2)_2$+2LiH (Mg-Li) 1st Desorption Fraction (0.10-0.80)	Intercept Value	Intercept Error	Slope Value	Slope Error	Statistics Adr. R-Square
D1 one-dimensional diffusion	-0.27626	0.02211	1.31016	0.01975	0.9939
D2 two-dimensional diffusion	-0.43203	0.04872	1.55547	0.04351	0.9793
D3 Jander eq. for three dimensional diffusion	-0.66457	0.09721	1.93167	0.08682	0.94818
D4 Ginstling-Braunshtein eq. for three dimensional diffusion	-0.50397	0.063	1.67114	0.05626	0.97027
F1 JMA - n = 1	-0.03271	0.01531	1.05852	0.01367	0.99552
R2 two - dimensional phase	0.11038	0.00959	0.85378	0.00856	0.99729
R3 three dimensional phase boundary	0.06666	0.00615	0.91517	0.00549	0.99903
F2 JMA - n = 1/2	0.41636	0.01364	0.54313	0.01218	0.98659
F3 JMA - n = 1/3	0.58797	0.01417	0.37134	0.01265	0.96958
F4 JMA - n = 1/4	0.68106	0.01275	0.2831	0.01138	0.9581
F5 JMA - n = 2/5	0.51712	0.01445	0.44051	0.01291	0.97732
$Mg(NH_2)_2$+2LiH (Mg-Li) 2nd Desorption Fraction (0.10-0.80)	Intercept Value	Intercept Error	Slope Value	Slope Error	Statistics Adr. R-Square
D1 one-dimensional diffusion	-0.25805	0.01988	1.29451	0.01773	0.99496
D2 two-dimensional diffusion	-0.41046	0.04688	1.53694	0.0418	0.9804
D3 Jander eq. for three dimensional diffusion	-0.63673	0.09623	1.90755	0.0858	0.9481
D4 Ginstling-Braunshtein eq. for three dimensional diffusion	-0.48057	0.06146	1.65099	0.0548	0.97108
F1 JMA - n = 1	-0.01609	0.01947	1.04386	0.01736	0.99259
R2 two - dimensional phase	0.12411	0.01464	0.84163	0.01306	0.99354
R3 three dimensional phase boundary	0.0812	0.01284	0.90231	0.01145	0.99567
F2 JMA - n = 1/2	0.42589	0.01662	0.53455	0.01482	0.97966
F3 JMA - n = 1/3	0.59482	0.0159	0.36512	0.01418	0.96083
F4 JMA - n = 1/4	0.68642	0.01399	0.27821	0.01248	0.94838
F5 JMA - n = 2/5	0.52508	0.01663	0.43331	0.01483	0.96932
$Mg(NH_2)_2$+2LiH (Mg-Li) 5th Desorption Fraction (0.10-0.80)	Intercept Value	Intercept Error	Slope Value	Slope Error	Statistics Adr. R-Square
D1 one-dimensional diffusion	-0.19098	0.01483	1.26539	0.01344	0.99696
D2 two-dimensional diffusion	-0.33515	0.03405	1.50708	0.03086	0.9888
D3 Jander eq. for three dimensional diffusion	-0.55048	0.07631	1.87837	0.06917	0.96463
D4 Ginstling-Braunshtein eq. for three dimensional diffusion	-0.40175	0.04625	1.62118	0.04193	0.98225
F1 JMA - n = 1	0.03675	0.01119	1.02174	0.01014	0.99735
R2 two - dimensional phase	0.16967	0.01733	0.82056	0.01571	0.9902
R3 three dimensional phase boundary	0.12904	0.01339	0.88082	0.01214	0.99489
F2 JMA - n = 1/2	0.45548	0.01819	0.52046	0.01649	0.97359
F3 JMA - n = 1/3	0.6156	0.01701	0.35488	0.01542	0.95141
F4 JMA - n = 1/4	0.70247	0.01481	0.27017	0.01342	0.93739
F5 JMA - n = 2/5	0.54947	0.01796	0.42145	0.01628	0.96121

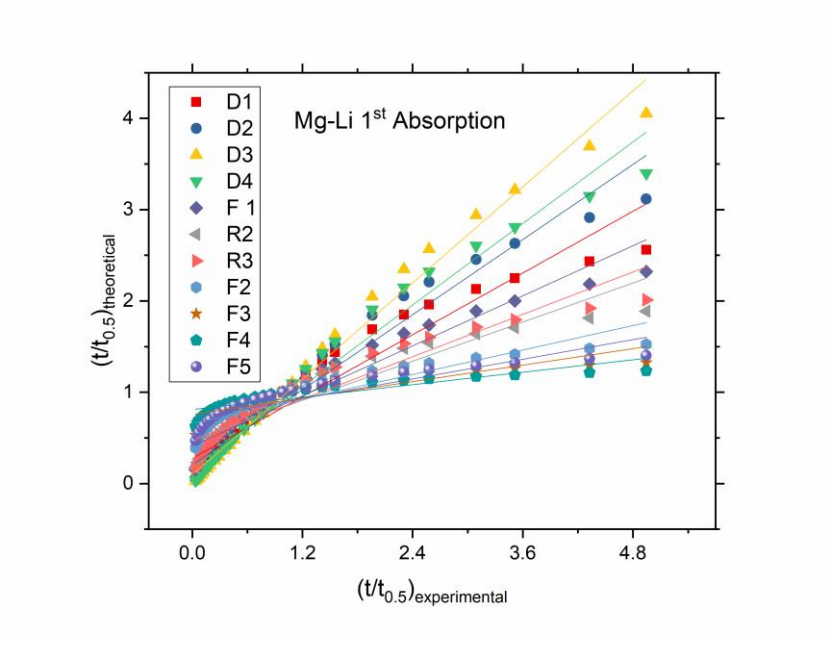

Figure A11 $(t/t_{0.5})_{experimental}$ vs. $(t/t_{0.5})_{theoretical}$ plot for sample Mg-Li ($Mg(NH_2)_2$+2LiH) at 1st absorption

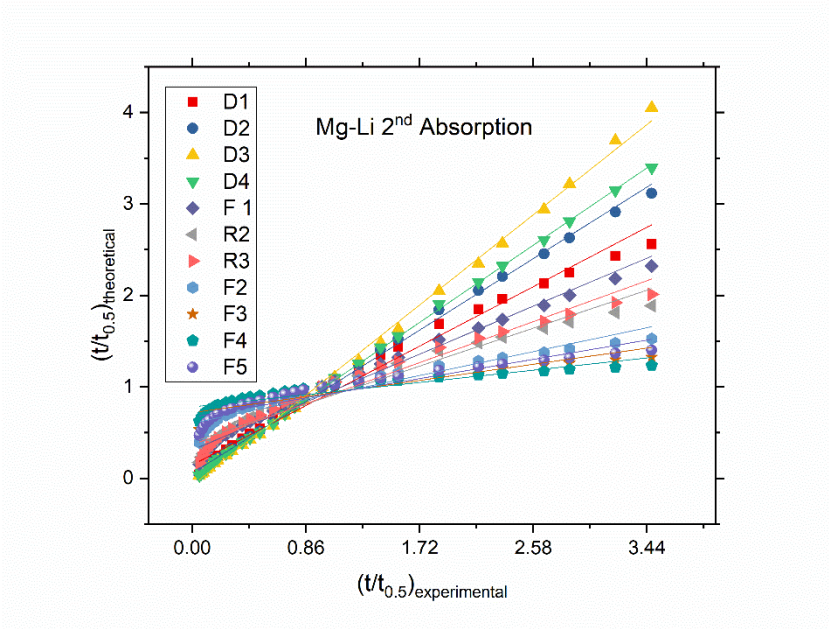

Figure A12 $(t/t_{0.5})_{experimental}$ vs. $(t/t_{0.5})_{theoretical}$ plot for sample Mg-Li ($Mg(NH_2)_2$+2LiH) at 2nd absorption

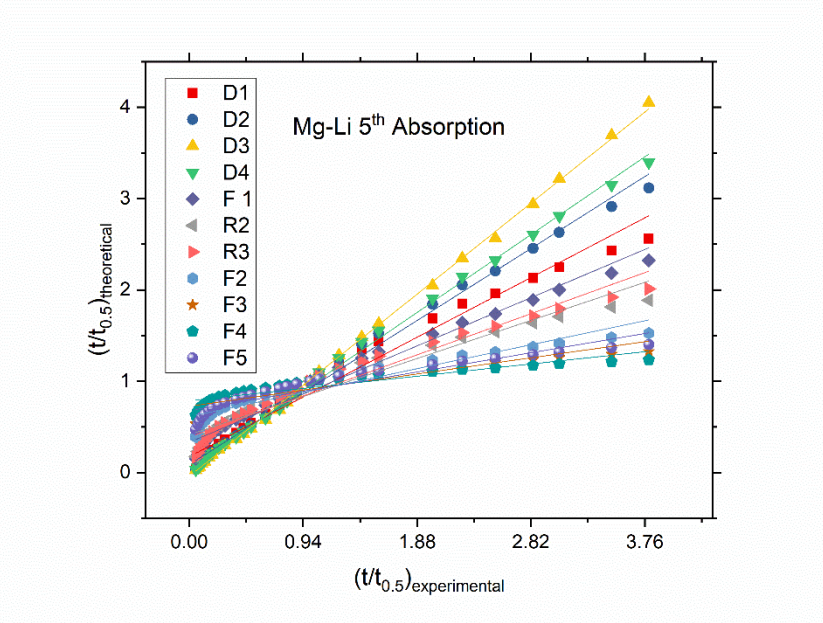

Figure A13 $(t/t_{0.5})_{experimental}$ vs. $(t/t_{0.5})_{theoretical}$ plot for sample Mg-Li ($Mg(NH_2)_2$+2LiH) at 5th absorption

Table A2 Fitting results for the absorption curves of Mg-Li material.

$Mg(NH_2)_2$+2LiH (Mg-Li) 1st Absorption Fraction (0.10-0.80)	Intercept Value	Intercept Error	Slope Value	Slope Error	Statistics Adr. R-Square
D1 one-dimensional diffusion	0.27581	0.05505	0.56387	0.03039	0.92707
D2 two-dimensional diffusion	0.20333	0.04848	0.68579	0.02676	0.96044
D3 Jander eq. for three dimensional diffusion	0.09406	0.03508	0.8764	0.01936	0.98698
D4 Ginstling-Braunshtein eq. for three dimensional diffusion	0.16967	0.04457	0.74409	0.0246	0.9713
F1 JMA - n = 1	0.41169	0.04221	0.4569	0.0233	0.93422
R2 two - dimensional phase	0.4829	0.04665	0.35708	0.02575	0.87629
R3 three dimensional phase boundary	0.46104	0.04556	0.38676	0.02515	0.89711
F2 JMA - n = 1/2	0.65776	0.0341	0.22355	0.01882	0.83836
F3 JMA - n = 1/3	0.75619	0.02648	0.15027	0.01462	0.79498
F4 JMA - n = 1/4	0.81051	0.02144	0.11357	0.01184	0.77131
F5 JMA - n = 2/5	0.71516	0.02988	0.17949	0.0165	0.81299
$Mg(NH_2)_2$+2LiH (Mg-Li) 2nd Absorption Fraction (0.10-0.80)	Intercept Value	Intercept Error	Slope Value	Slope Error	Statistics Adr. R-Square
D1 one-dimensional diffusion	0.14562	0.02739	0.75576	0.01834	0.98435
D2 two-dimensional diffusion	0.05548	0.01268	0.90954	0.00849	0.99765
D3 Jander eq. for three dimensional diffusion	-0.07838	0.01611	1.14717	0.01079	0.99762
D4 Ginstling-Braunshtein eq. for three dimensional diffusion	0.01404	0.0057	0.98246	0.00382	0.99959
F1 JMA - n = 1	0.30895	0.02272	0.60986	0.01521	0.98346
R2 two - dimensional phase	0.39564	0.0323	0.48301	0.02163	0.94854
R3 three dimensional phase boundary	0.36899	0.02961	0.5209	0.01983	0.9623
F2 JMA - n = 1/2	0.60159	0.02632	0.30381	0.01762	0.91648
F3 JMA - n = 1/3	0.71707	0.02172	0.20546	0.01454	0.88036
F4 JMA - n = 1/4	0.78044	0.01803	0.15576	0.01207	0.85972
F5 JMA - n = 2/5	0.66909	0.02397	0.24481	0.01605	0.89565
$Mg(NH_2)_2$+2LiH (Mg-Li) 5th Absorption Fraction (0.10-0.80)	Intercept Value	Intercept Error	Slope Value	Slope Error	Statistics Adr. R-Square
D1 one-dimensional diffusion	0.17338	0.03308	0.69585	0.0208	0.97642
D2 two-dimensional diffusion	0.08687	0.02004	0.8392	0.0126	0.99395
D3 Jander eq. for three dimensional diffusion	-0.04185	0.00957	1.06112	0.00602	0.99913
D4 Ginstling-Braunshtein eq. for three dimensional diffusion	0.04705	0.01341	0.90726	0.00843	0.99767
F1 JMA - n = 1	0.33098	0.02656	0.56183	0.0167	0.97668
R2 two - dimensional phase	0.41445	0.03524	0.44379	0.02216	0.93679
R3 three dimensional phase boundary	0.38879	0.03285	0.47902	0.02066	0.95211
F2 JMA - n = 1/2	0.61377	0.0279	0.27883	0.01755	0.90305
F3 JMA - n = 1/3	0.72558	0.02269	0.18833	0.01427	0.86509
F4 JMA - n = 1/4	0.787	0.01873	0.14267	0.01178	0.84364
F5 JMA - n = 2/5	0.6791	0.02518	0.22451	0.01583	0.88108

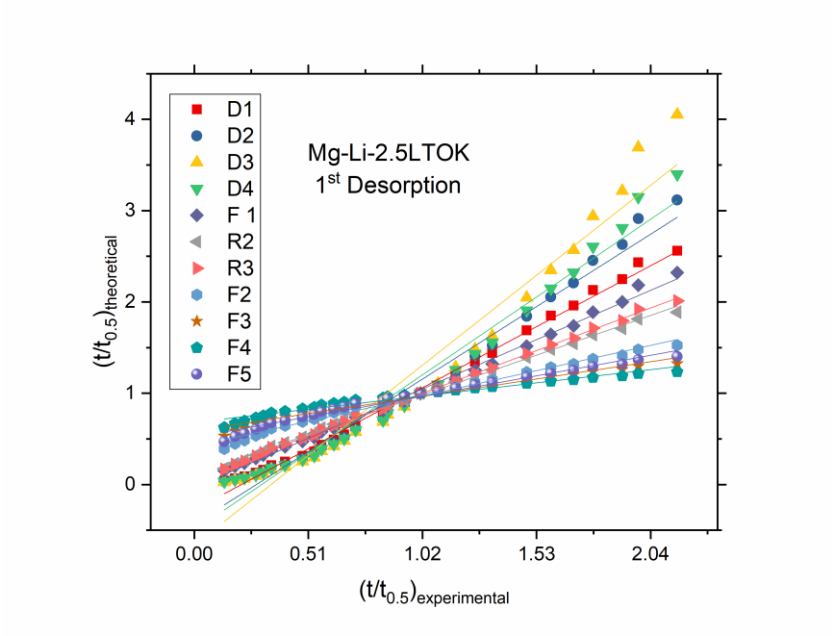

Figure A14 $(t/t_{0.5})_{experimental}$ vs. $(t/t_{0.5})_{theoretical}$ plot for sample Mg-Li-2.5LTOK at 1st desorption

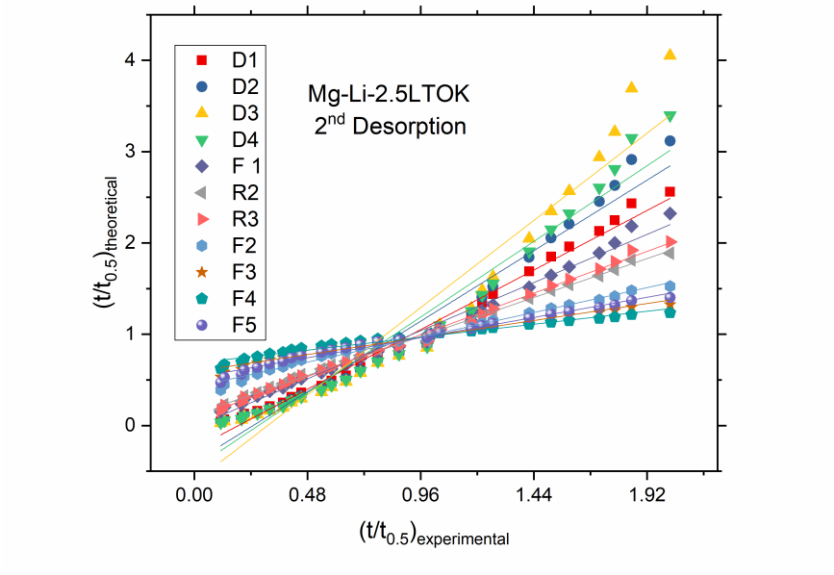

Figure A15 $(t/t_{0.5})_{experimental}$ vs. $(t/t_{0.5})_{theoretical}$ plot for sample Mg-Li-2.5LTOK at 2nd desorption

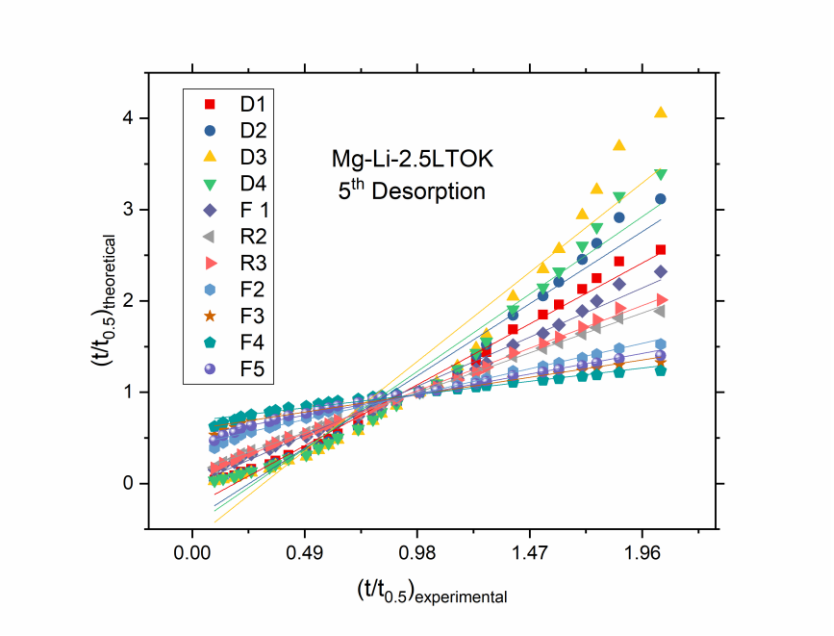

Figure A16 $(t/t_{0.5})_{experimental}$ vs. $(t/t_{0.5})_{theoretical}$ plot for sample Mg-Li-2.5LTOK at 5th desorption

Table A3 Fitting results for the desorption curves of Mg-Li-2.5LTOK material.

$Mg(NH_2)_2$+2LiH+0.025LTOK (Mg-Li-2.5LTOK) 1st Des. Fraction (0.10-0.80)	Intercept Value	Intercept Error	Slope Value	Slope Error	Statistics Adr. R-Square
D1 one-dimensional diffusion	-0.2396	0.02113	1.3283	0.01954	0.99419
D2 two-dimensional diffusion	-0.38732	0.04927	1.5757	0.04557	0.9779
D3 Jander eq. for three dimensional diffusion	-0.60701	0.09841	1.95455	0.09103	0.94456
D4 Ginstling-Braunshtein eq. for three dimensional diffusion	-0.45535	0.06386	1.69223	0.05907	0.96812
F1 JMA - n = 1	-0.00231	0.01712	1.07232	0.01583	0.99415
R2 two - dimensional phase	0.13424	0.0087	0.86564	0.00805	0.99767
R3 three dimensional phase boundary	0.09245	0.00648	0.92764	0.00599	0.99887
F2 JMA - n = 1/2	0.43163	0.01336	0.55057	0.01236	0.98657
F3 JMA - n = 1/3	0.59839	0.01383	0.37646	0.01279	0.96972
F4 JMA - n = 1/4	0.68899	0.01245	0.287	0.01152	0.95826
F5 JMA - n = 2/5	0.52949	0.01412	0.44657	0.01306	0.97742
$Mg(NH_2)_2$+2LiH+0.025LTOK (Mg-Li-2.5LTOK) 2nd Des. Fraction (0.10-0.80)	Intercept Value	Intercept Error	Slope Value	Slope Error	Statistics Adr. R-Square
D1 one-dimensional diffusion	-0.25464	0.03255	1.3592	0.03057	0.98652
D2 two-dimensional diffusion	-0.40179	0.06211	1.60861	0.05834	0.96566
D3 Jander eq. for three dimensional diffusion	-0.62039	0.1136	1.9903	0.1067	0.9278
D4 Ginstling-Braunshtein eq. for three dimensional diffusion	-0.4695	0.0774	1.72603	0.07269	0.95422
F1 JMA - n = 1	-0.01499	0.02521	1.09786	0.02368	0.98759
R2 two - dimensional phase	0.12155	0.00924	0.88899	0.00868	0.99743
R3 three dimensional phase boundary	0.07973	0.01155	0.95167	0.01085	0.9965
F2 JMA - n = 1/2	0.42254	0.01139	0.56655	0.01069	0.99047
F3 JMA - n = 1/3	0.59153	0.01212	0.3881	0.01138	0.97728
F4 JMA - n = 1/4	0.68351	0.01109	0.29616	0.01042	0.96763
F5 JMA - n = 2/5	0.52166	0.0122	0.46004	0.01146	0.98352
$Mg(NH_2)_2$+2LiH+0.025LTOK (Mg-Li-2.5LTOK) 5th Des. Fraction (0.10-0.80)	Intercept Value	Intercept Error	Slope Value	Slope Error	Statistics Adr. R-Square
D1 one-dimensional diffusion	-0.25222	0.03054	1.36081	0.02875	0.98808
D2 two-dimensional diffusion	-0.39979	0.05947	1.61148	0.05598	0.9684
D3 Jander eq. for three dimensional diffusion	-0.6193	0.11009	1.99538	0.10364	0.93193
D4 Ginstling-Braunshtein eq. for three dimensional diffusion	-0.46776	0.07447	1.72955	0.07011	0.95745
F1 JMA - n = 1	-0.0134	0.02268	1.09956	0.02135	0.98992
R2 two - dimensional phase	0.12336	0.0072	0.88979	0.00678	0.99843
R3 three dimensional phase boundary	0.08149	0.00888	0.95273	0.00836	0.99793
F2 JMA - n = 1/2	0.42369	0.01076	0.56706	0.01013	0.99145
F3 JMA - n = 1/3	0.59237	0.01191	0.38839	0.01122	0.97796
F4 JMA - n = 1/4	0.68417	0.01097	0.29636	0.01033	0.96819
F5 JMA - n = 2/5	0.52263	0.01188	0.46041	0.01118	0.98431

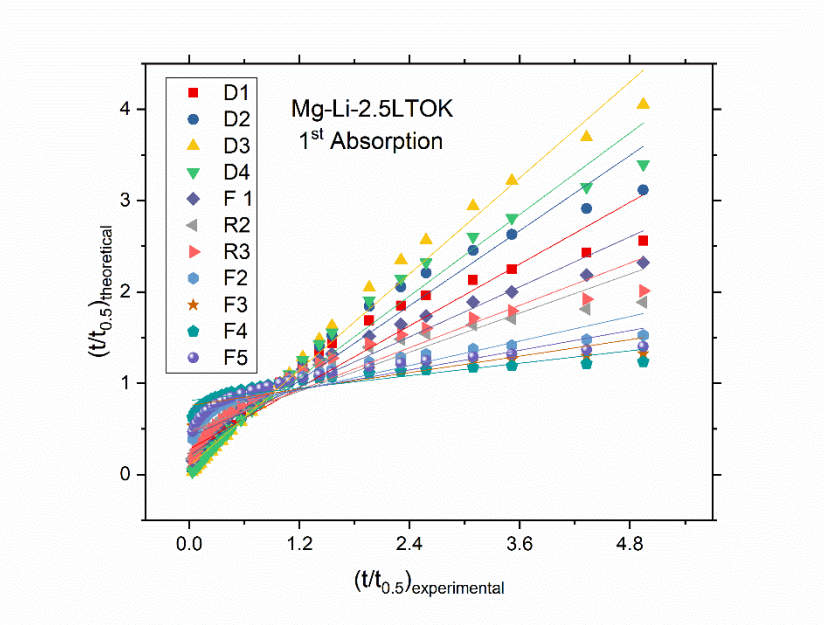

Figure A17 $(t/t_{0.5})_{experimental}$ vs. $(t/t_{0.5})_{theoretical}$ plot for sample Mg-Li-2.5LTOK at 1st absorption

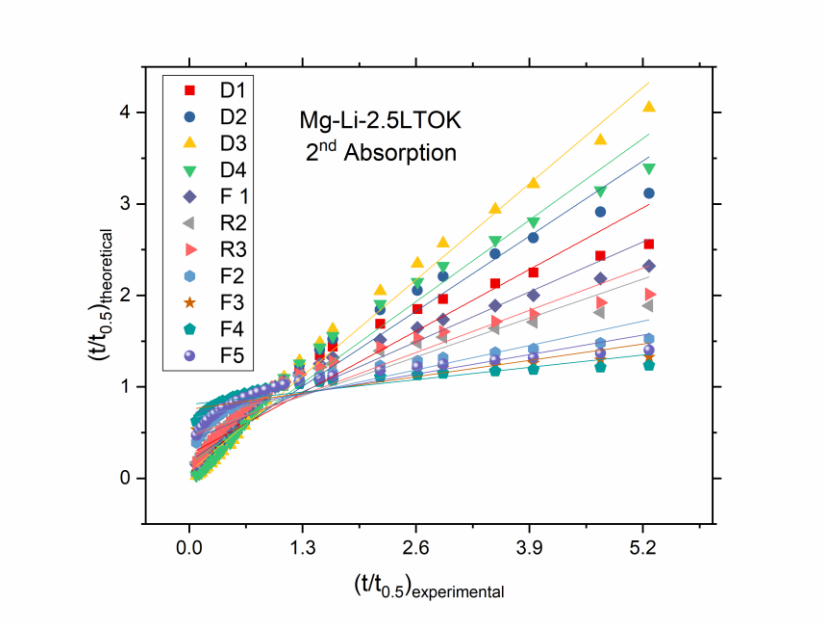

Figure A18 $(t/t_{0.5})_{experimental}$ vs. $(t/t_{0.5})_{theoretical}$ plot for sample Mg-Li-2.5LTOK at 1st absorption

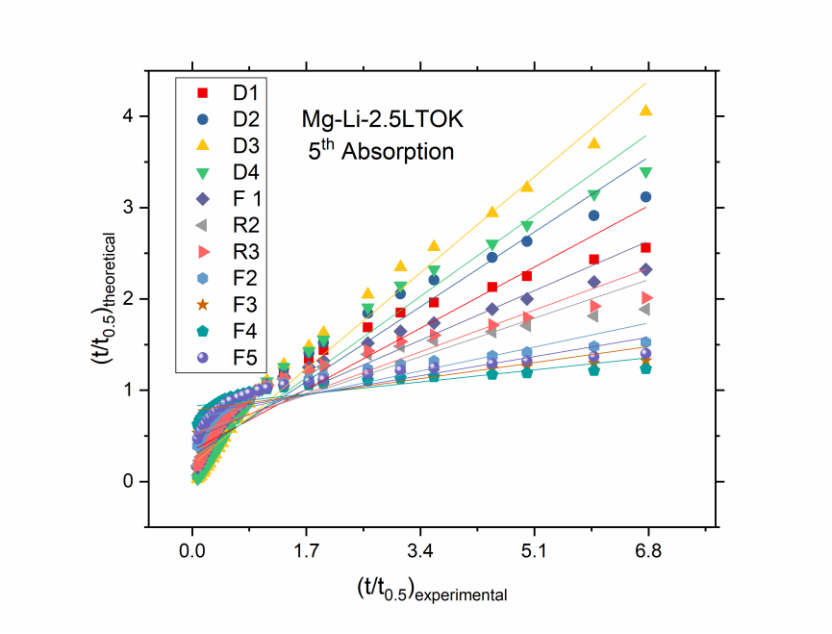

Figure A19 $(t/t_{0.5})_{experimental}$ vs. $(t/t_{0.5})_{theoretical}$ plot for sample Mg-Li-2.5LTOK at 1st absorption

Table A4 Fitting results for the absorption curves of Mg-Li-2.5LTOK material.

$Mg(NH_2)_2$+2LiH+0.025LTOK (Mg-Li-2.5LTOK) 1st Abs. Fraction (0.10-0.80)	Intercept Value	Intercept Error	Slope Value	Slope Error	Statistics Adr. R-Square
D1 one-dimensional diffusion	0.27581	0.05505	0.56387	0.03039	0.92707
D2 two-dimensional diffusion	0.20333	0.04848	0.68579	0.02676	0.96044
D3 Jander eq. for three dimensional diffusion	0.09406	0.03508	0.8764	0.01936	0.98698
D4 Ginstling-Braunshtein eq. for three dimensional diffusion	0.16967	0.04457	0.74409	0.0246	0.9713
F1 JMA - n = 1	0.41169	0.04221	0.4569	0.0233	0.93422
R2 two - dimensional phase	0.4829	0.04665	0.35708	0.02575	0.87629
R3 three dimensional phase boundary	0.46104	0.04556	0.38676	0.02515	0.89711
F2 JMA - n = 1/2	0.65776	0.0341	0.22355	0.01882	0.83836
F3 JMA - n = 1/3	0.75619	0.02648	0.15027	0.01462	0.79498
F4 JMA - n = 1/4	0.81051	0.02144	0.11357	0.01184	0.77131
F5 JMA - n = 2/5	0.71516	0.02988	0.17949	0.0165	0.81299
$Mg(NH_2)_2$+2LiH+0.025LTOK (Mg-Li-2.5LTOK) 2nd Abs. Fraction (0.10-0.80)	Intercept Value	Intercept Error	Slope Value	Slope Error	Statistics Adr. R-Square
D1 one-dimensional diffusion	0.26146	0.0579	0.51869	0.02917	0.92108
D2 two-dimensional diffusion	0.18461	0.051	0.63176	0.0257	0.95717
D3 Jander eq. for three dimensional diffusion	0.0687	0.03641	0.8084	0.01834	0.98628
D4 Ginstling-Braunshtein eq. for three dimensional diffusion	0.1489	0.04684	0.6858	0.0236	0.96898
F1 JMA - n = 1	0.40034	0.04488	0.42008	0.02261	0.92726
R2 two - dimensional phase	0.47488	0.04904	0.32767	0.02471	0.86626
R3 three dimensional phase boundary	0.45203	0.04804	0.35515	0.02421	0.88809
F2 JMA - n = 1/2	0.65309	0.03571	0.20489	0.01799	0.82661
F3 JMA - n = 1/3	0.75326	0.02761	0.13756	0.01391	0.78189
F4 JMA - n = 1/4	0.80839	0.02232	0.1039	0.01124	0.75764
F5 JMA - n = 2/5	0.71157	0.03121	0.16439	0.01573	0.8004
$Mg(NH_2)_2$+2LiH+0.025LTOK (Mg-Li-2.5LTOK) 5th Abs. Fraction (0.10-0.80)	Intercept Value	Intercept Error	Slope Value	Slope Error	Statistics Adr. R-Square
D1 one-dimensional diffusion	0.3387	0.06242	0.3943	0.02533	0.89936
D2 two-dimensional diffusion	0.27618	0.05714	0.48183	0.02319	0.94101
D3 Jander eq. for three dimensional diffusion	0.18242	0.04526	0.61871	0.01837	0.97674
D4 Ginstling-Braunshtein eq. for three dimensional diffusion	0.24727	0.0538	0.5237	0.02184	0.95509
F1 JMA - n = 1	0.46309	0.04904	0.31922	0.0199	0.90469
R2 two - dimensional phase	0.52565	0.05167	0.24786	0.02097	0.83706
R3 three dimensional phase boundary	0.50638	0.05112	0.26907	0.02074	0.86099
F2 JMA - n = 1/2	0.68555	0.03717	0.15453	0.01508	0.79381
F3 JMA - n = 1/3	0.77554	0.02843	0.10345	0.01154	0.74622
F4 JMA - n = 1/4	0.8254	0.02287	0.07802	0.00928	0.72071
F5 JMA - n = 2/5	0.73795	0.03227	0.12377	0.0131	0.76583

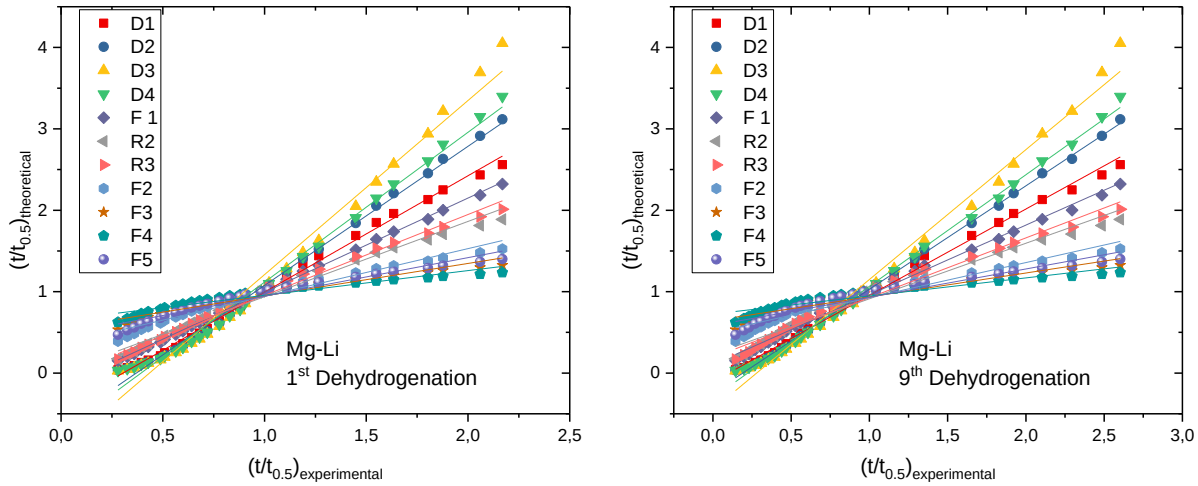

Figure A20 $(t/t_{0.5})_{experimental}$ vs. $(t/t_{0.5})_{theoretical}$ plot for sample Mg-Li ($6Mg(NH_2)_2$+9LiH) at 1st and 9th dehydrogenation

Table A5 Fitting results for the 1st dehydrogenation of the Mg-Li ($6Mg(NH_2)_2$+9LiH) material.

$6Mg(NH_2)_2$+9LiH 1st Dehydrogenation Fraction (0.10-0.80)	Intercept Value	Intercept Error	Slope Value	Slope Error	Statistics Adr. R-Square
D1 one-dimensional diffusion	-0.435	0.021	1.429	0.019	0.995
D2 two-dimensional diffusion	-0.632	0.027	1.709	0.024	0.995
D3 Jander eq. for three dimensional diffusion	-0.929	0.067	2.139	0.060	0.979
D4 Ginstling-Braunshtein eq. for three dimensional diffusion	-0.723	0.038	1.841	0.034	0.991
F1 JMA - n = 1	-0.162	0.008	1.156	0.007	0.999
R2 two - dimensional phase	0.014	0.026	0.924	0.023	0.983
R3 three dimensional phase boundary	-0.039	0.021	0.994	0.019	0.991
F2 JMA - n = 1/2	0.357	0.024	0.586	0.022	0.965
F3 JMA - n = 1/3	0.549	0.022	0.399	0.019	0.940
F4 JMA - n = 1/4	0.652	0.019	0.303	0.017	0.924
F5 JMA - n = 2/5	0.470	0.023	0.474	0.021	0.951

Table A6 Fitting results for the 9th dehydrogenation of the Mg-Li ($6Mg(NH_2)_2$+9LiH) material.

$6Mg(NH_2)_2$+9LiH 9th Dehydrogenation Fraction (0.10-0.80)	Intercept Value	Intercept Error	Slope Value	Slope Error	Statistics Adr. R-Square
D1 one-dimensional diffusion	-0.106	0.019	1.061	0.016	0.994
D2 two-dimensional diffusion	-0.242	0.010	1.271	0.008	0.999
D3 Jander eq. for three dimensional diffusion	-0.446	0.041	1.595	0.033	0.989
D4 Ginstling-Braunshtein eq. for three dimensional diffusion	-0.305	0.017	1.371	0.014	0.997
F1 JMA - n = 1	0.105	0.016	0.856	0.012	0.994
R2 two - dimensional phase	0.230	0.028	0.682	0.023	0.971
R3 three dimensional phase boundary	0.192	0.025	0.734	0.020	0.981
F2 JMA - n = 1/2	0.496	0.025	0.431	0.020	0.946
F3 JMA - n = 1/3	0.644	0.021	0.292	0.017	0.916
F4 JMA - n = 1/4	0.725	0.018	0.222	0.014	0.898
F5 JMA - n = 2/5	0.583	0.023	0.348	0.019	0.929

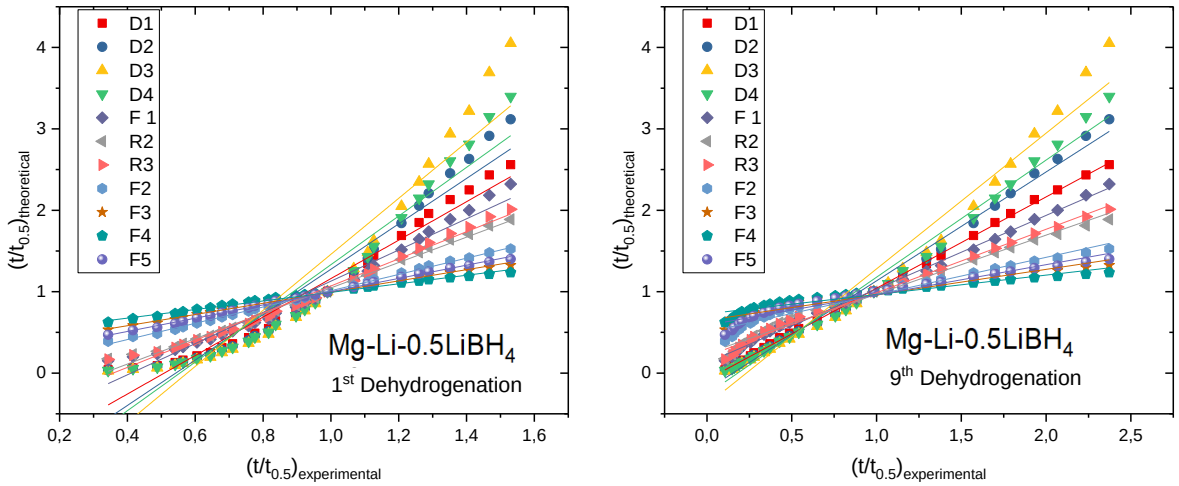

Figure A21 $(t/t_{0.5})_{experimental}$ vs. $(t/t_{0.5})_{theoretical}$ plot for sample Mg-Li-0.5LiBH$_4$ at 1st and 9th dehydrogenation

Table A7 Fitting results for the 1st dehydrogenation of the Mg-Li-0.5LiBH$_4$ material.

6Mg(NH$_2$)$_2$+9LiH +0.5 LiBH$_4$ 1st Dehydrogenation Fraction (0.10-0.80)	Intercept Value	Intercept Error	Slope Value	Slope Error	Statistics Adr. R-Square
D1 one-dimensional diffusion	-1.202	0.091	2.362	0.094	0.961
D2 two-dimensional diffusion	-1.513	0.141	2.788	0.145	0.934
D3 Jander eq. for three dimensional diffusion	-1.982	0.227	3.442	0.233	0.893
D4 Ginstling-Braunshtein eq. for three dimensional diffusion	-1.657	0.166	2.989	0.171	0.921
F1 JMA - n = 1	-0.787	0.064	1.916	0.066	0.970
R2 two - dimensional phase	-0.513	0.028	1.559	0.029	0.991
R3 three dimensional phase boundary	-0.596	0.038	1.666	0.039	0.986
F2 JMA - n = 1/2	0.012	0.007	1.000	0.007	0.999
F3 JMA - n = 1/3	0.307	0.008	0.688	0.008	0.996
F4 JMA - n = 1/4	0.465	0.009	0.527	0.009	0.993
F5 JMA - n = 2/5	0.186	0.007	0.814	0.007	0.998

Table A8 Fitting results for the 9th dehydrogenation of the Mg-Li-0.5LiBH$_4$ material.

6Mg(NH$_2$)$_2$+9LiH +0.5 LiBH$_4$ 9th Dehydrogenation Fraction (0.10-0.80)	Intercept Value	Intercept Error	Slope Value	Slope Error	Statistics Adr. R-Square
D1 one-dimensional diffusion	-0.080	0.007	1.122	0.006	0.999
D2 two-dimensional diffusion	-0.204	0.027	1.337	0.023	0.992
D3 Jander eq. for three dimensional diffusion	-0.387	0.068	1.667	0.058	0.968
D4 Ginstling-Braunshtein eq. for three dimensional diffusion	-0.261	0.039	1.439	0.034	0.985
F1 JMA - n = 1	0.127	0.012	0.905	0.011	0.996
R2 two - dimensional phase	0.243	0.019	0.726	0.016	0.987
R3 three dimensional phase boundary	0.208	0.015	0.780	0.013	0.993
F2 JMA - n = 1/2	0.503	0.019	0.460	0.016	0.967
F3 JMA - n = 1/3	0.648	0.017	0.313	0.015	0.942
F4 JMA - n = 1/4	0.728	0.015	0.238	0.013	0.927
F5 JMA - n = 2/5	0.588	0.018	0.372	0.016	0.953

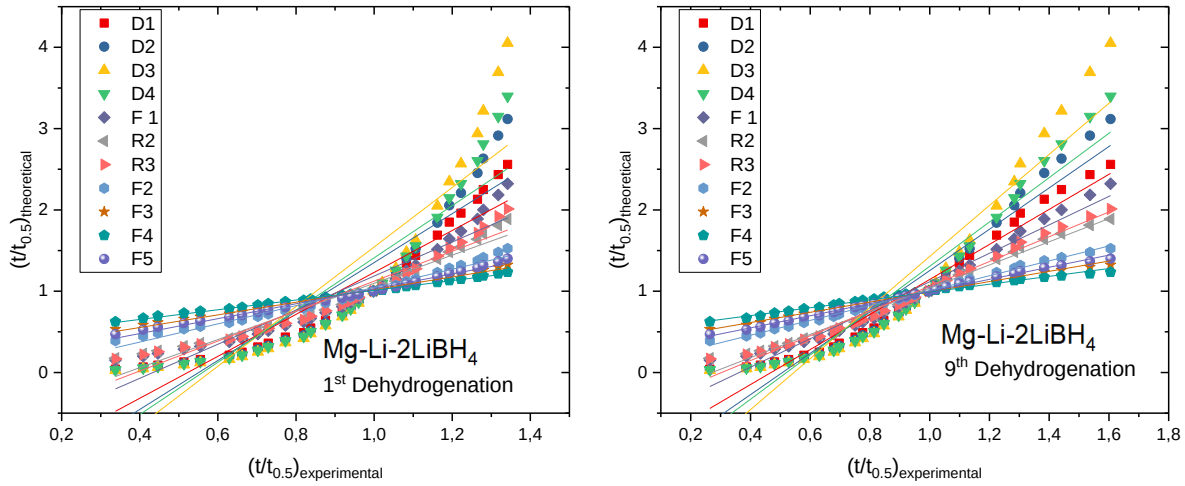

Figure A22 $(t/t_{0.5})_{experimental}$ vs. $(t/t_{0.5})_{theoretical}$ plot for sample Mg-Li-2LiBH$_4$ at 1st and 9th dehydrogenation

Table A9 Fitting results for the 1st dehydrogenation of the Mg-Li-2LiBH$_4$ material.

6Mg(NH$_2$)$_2$+9LiH +2LiBH$_4$ 1st Dehydrogenation Fraction (0.10-0.80)	Intercept Value	Intercept Error	Slope Value	Slope Error	Statistics Adr. R-Square
D1 one-dimensional diffusion	-1.349	0.160	2.580	0.169	0.895
D2 two-dimensional diffusion	-1.658	0.228	3.010	0.242	0.851
D3 Jander eq. for three dimensional diffusion	-2.122	0.341	3.665	0.361	0.790
D4 Ginstling-Braunshtein eq. for three dimensional diffusion	-1.801	0.262	3.212	0.278	0.831
F1 JMA - n = 1	-0.910	0.121	2.096	0.129	0.907
R2 two - dimensional phase	-0.633	0.068	1.731	0.073	0.955
R3 three dimensional phase boundary	-0.717	0.084	1.841	0.089	0.941
F2 JMA - n = 1/2	-0.074	0.030	1.120	0.032	0.979
F3 JMA - n = 1/3	0.242	0.012	0.777	0.013	0.992
F4 JMA - n = 1/4	0.413	0.006	0.597	0.007	0.997
F5 JMA - n = 2/5	0.112	0.018	0.917	0.020	0.988

Table A10 Fitting results for the 9th dehydrogenation of the Mg-Li-2LiBH$_4$ material.

6Mg(NH$_2$)$_2$+9LiH +2LiBH$_4$ 9th Dehydrogenation Fraction (0.10-0.80)	Intercept Value	Intercept Error	Slope Value	Slope Error	Statistics Adr. R-Square
D1 one-dimensional diffusion	-1.011	0.089	2.155	0.090	0.955
D2 two-dimensional diffusion	-1.290	0.133	2.544	0.135	0.929
D3 Jander eq. for three dimensional diffusion	-1.713	0.210	3.140	0.213	0.889
D4 Ginstling-Braunshtein eq. for three dimensional diffusion	-1.421	0.156	2.727	0.158	0.917
F1 JMA - n = 1	-0.635	0.061	1.751	0.062	0.967
R2 two - dimensional phase	-0.387	0.030	1.425	0.031	0.987
R3 three dimensional phase boundary	-0.462	0.038	1.523	0.039	0.983
F2 JMA - n = 1/2	0.092	0.011	0.915	0.011	0.996
F3 JMA - n = 1/3	0.362	0.009	0.630	0.009	0.994
F4 JMA - n = 1/4	0.507	0.009	0.483	0.009	0.991
F5 JMA - n = 2/5	0.251	0.009	0.746	0.009	0.996

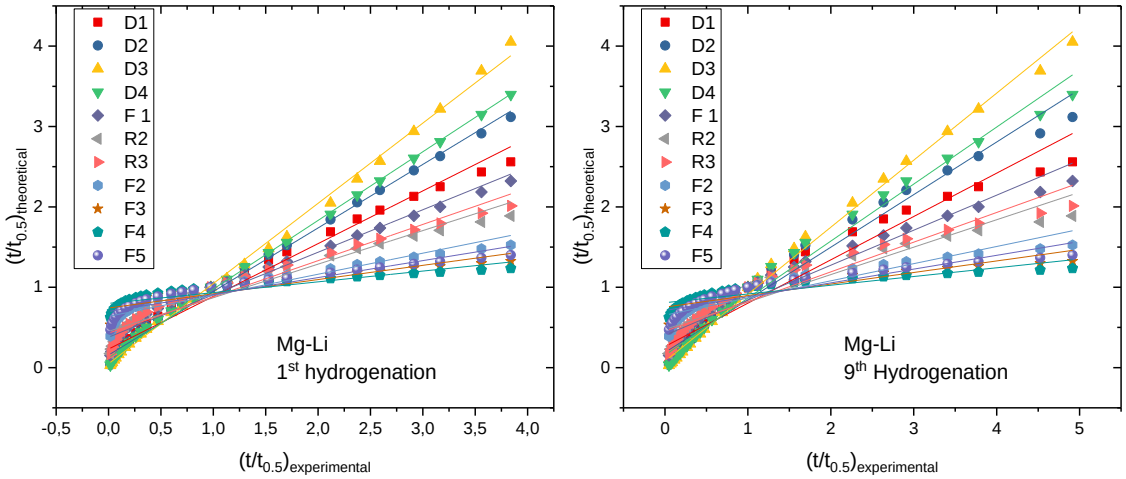

Figure A23 $(t/t_{0.5})_{experimental}$ vs. $(t/t_{0.5})_{theoretical}$ plot for sample Mg-Li at 1st and 9th hydrogenation

Table A11 Fitting results for the 1st hydrogenation of the Mg-Li material.

$6Mg(NH_2)_2$+9LiH 1st hydrogenation Fraction (0.10-0.80)	Intercept Value	Intercept Error	Slope Value	Slope Error	Statistics Adr. R-Square
D1 one-dimensional diffusion	0,231	0,030	0,656	0,018	0,979
D2 two-dimensional diffusion	0,157	0,018	0,791	0,011	0,995
D3 Jander eq. for three dimensional diffusion	0,049	0,018	0,998	0,011	0,997
D4 Ginstling-Braunshtein eq. for three dimensional diffusion	0,123	0,013	0,854	0,008	0,998
F1 JMA - n = 1	0,379	0,026	0,529	0,016	0,975
R2 two - dimensional phase	0,452	0,034	0,418	0,021	0,937
R3 three dimensional phase boundary	0,429	0,032	0,451	0,020	0,952
F2 JMA - n = 1/2	0,638	0,027	0,262	0,017	0,901
F3 JMA - n = 1/3	0,742	0,022	0,177	0,014	0,862
F4 JMA - n = 1/4	0,799	0,018	0,134	0,011	0,840
F5 JMA - n = 2/5	0,698	0,025	0,211	0,015	0,878

Table A12 Fitting results for the 9th hydrogenation of the Mg-Li material.

$6Mg(NH_2)_2$+9LiH 9th hydrogenation Fraction (0.10-0.80)	Intercept Value	Intercept Error	Slope Value	Slope Error	Statistics Adr. R-Square
D1 one-dimensional diffusion	0,263	0,048	0,539	0,025	0,944
D2 two-dimensional diffusion	0,189	0,039	0,655	0,020	0,974
D3 Jander eq. for three dimensional diffusion	0,079	0,021	0,834	0,011	0,995
D4 Ginstling-Braunshtein eq. for three dimensional diffusion	0,155	0,034	0,710	0,018	0,983
F1 JMA - n = 1	0,402	0,038	0,436	0,020	0,947
R2 two - dimensional phase	0,475	0,044	0,341	0,023	0,892
R3 three dimensional phase boundary	0,453	0,042	0,369	0,022	0,912
F2 JMA - n = 1/2	0,653	0,033	0,214	0,017	0,853
F3 JMA - n = 1/3	0,753	0,026	0,144	0,013	0,809
F4 JMA - n = 1/4	0,808	0,021	0,109	0,011	0,785
F5 JMA - n = 2/5	0,711	0,029	0,172	0,015	0,827

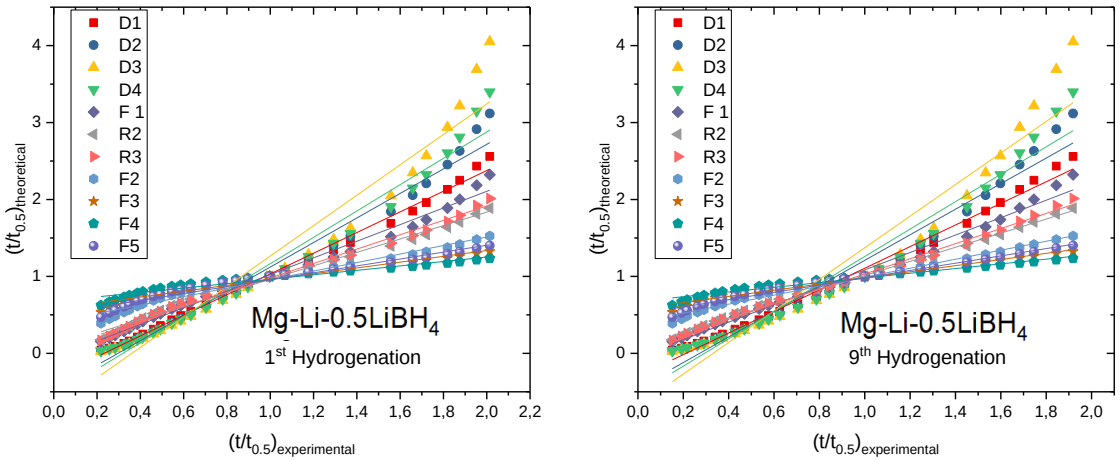

Figure A24 $(t/t_{0.5})_{experimental}$ vs. $(t/t_{0.5})_{theoretical}$ plot for sample Mg-Li-0.5LiBH$_4$ at 1st and 9th hydrogenation

Table A13 Fitting results for the 1st hydrogenation of the Mg-Li-0.5LiBH$_4$ material.

6Mg(NH$_2$)$_2$+9LiH+0.5LiBH$_4$ 1st hydrogenation Fraction (0.10-0.80)	Intercept Value	Intercept Error	Slope Value	Slope Error	Statistics Adr. R-Square
D1 one-dimensional diffusion	-0,312	0,021	1,344	0,019	0,995
D2 two-dimensional diffusion	-0,473	0,050	1,595	0,045	0,979
D3 Jander eq. for three dimensional diffusion	-0,713	0,102	1,977	0,092	0,945
D4 Ginstling-Braunshtein eq. for three dimensional diffusion	-0,548	0,065	1,713	0,059	0,969
F1 JMA - n = 1	-0,057	0,025	1,082	0,022	0,989
R2 two - dimensional phase	0,091	0,019	0,872	0,017	0,990
R3 three dimensional phase boundary	0,045	0,018	0,935	0,016	0,992
F2 JMA - n = 1/2	0,405	0,020	0,553	0,018	0,973
F3 JMA - n = 1/3	0,581	0,018	0,378	0,016	0,953
F4 JMA - n = 1/4	0,676	0,016	0,288	0,014	0,940
F5 JMA - n = 2/5	0,509	0,019	0,448	0,017	0,962

Table A14 Fitting results for the 9th hydrogenation of the Mg-Li-0.5LiBH$_4$ material.

6Mg(NH$_2$)$_2$+9LiH+0.5LiBH$_4$ 9th hydrogenation Fraction (0.10-0.80)	Intercept Value	Intercept Error	Slope Value	Slope Error	Statistics Adr. R-Square
D1 one-dimensional diffusion	-0,298	0,030	1,404	0,029	0,989
D2 two-dimensional diffusion	-0,452	0,063	1,661	0,059	0,967
D3 Jander eq. for three dimensional diffusion	-0,680	0,118	2,053	0,111	0,926
D4 Ginstling-Braunshtein eq. for three dimensional diffusion	-0,523	0,079	1,782	0,075	0,954
F1 JMA - n = 1	-0,048	0,027	1,132	0,026	0,986
R2 two - dimensional phase	0,094	0,010	0,917	0,010	0,997
R3 three dimensional phase boundary	0,051	0,013	0,982	0,012	0,996
F2 JMA - n = 1/2	0,406	0,013	0,584	0,012	0,988
F3 JMA - n = 1/3	0,580	0,013	0,400	0,013	0,974
F4 JMA - n = 1/4	0,675	0,012	0,305	0,011	0,964
F5 JMA - n = 2/5	0,508	0,014	0,474	0,013	0,980

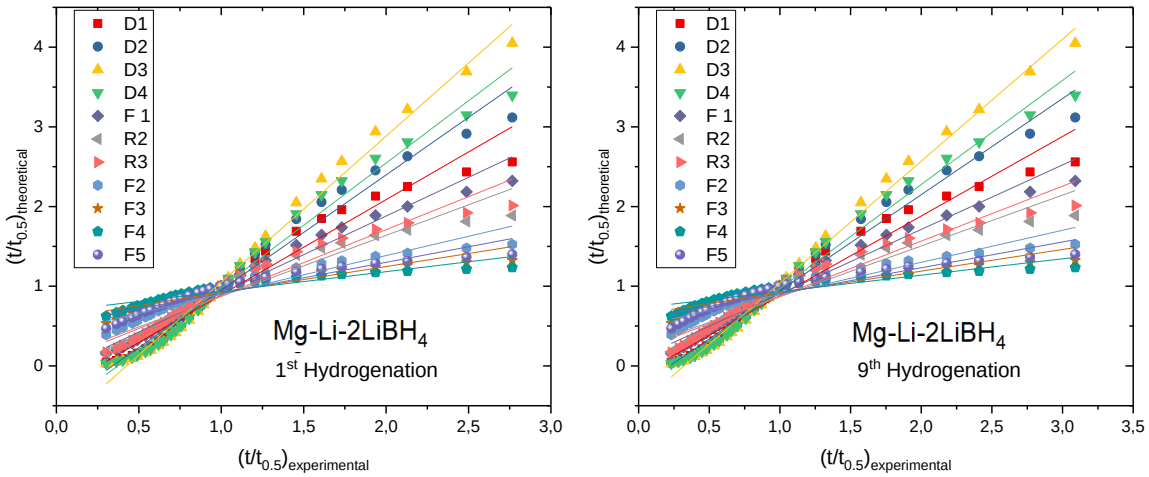

Figure A25 $(t/t_{0.5})_{experimental}$ vs. $(t/t_{0.5})_{theoretical}$ plot for sample Mg-Li-2LiBH$_4$ at 1st and 9th hydrogenation

Table A15 Fitting results for the 1st hydrogenation of the Mg-Li-2LiBH$_4$ material.

6Mg(NH$_2$)$_2$+9LiH+2LiBH$_4$ 1st hydrogenation Fraction (0.10-0.80)	Intercept Value	Intercept Error	Slope Value	Slope Error	Statistics Adr. R-Square
D1 one-dimensional diffusion	-0,305	0,061	1,196	0,049	0,957
D2 two-dimensional diffusion	-0,492	0,053	1,444	0,043	0,977
D3 Jander eq. for three dimensional diffusion	-0,780	0,047	1,832	0,038	0,989
D4 Ginstling-Braunshtein eq. for three dimensional diffusion	-0,581	0,050	1,563	0,040	0,983
F1 JMA - n = 1	-0,061	0,042	0,971	0,034	0,968
R2 two - dimensional phase	0,106	0,051	0,766	0,041	0,927
R3 three dimensional phase boundary	0,055	0,049	0,827	0,039	0,942
F2 JMA - n = 1/2	0,418	0,038	0,483	0,031	0,901
F3 JMA - n = 1/3	0,592	0,030	0,327	0,025	0,867
F4 JMA - n = 1/4	0,686	0,025	0,248	0,020	0,848
F5 JMA - n = 2/5	0,521	0,034	0,390	0,027	0,882

Table A16 Fitting results for the 9th hydrogenation of the Mg-Li-2LiBH$_4$ material.

6Mg(NH$_2$)$_2$+9LiH+2LiBH$_4$ 9th hydrogenation Fraction (0.10-0.80)	Intercept Value	Intercept Error	Slope Value	Slope Error	Statistics Adr. R-Square
D1 one-dimensional diffusion	-0,116	0,052	0,998	0,039	0,960
D2 two-dimensional diffusion	-0,265	0,042	1,207	0,032	0,982
D3 Jander eq. for three dimensional diffusion	-0,492	0,031	1,531	0,023	0,994
D4 Ginstling-Braunshtein eq. for three dimensional diffusion	-0,335	0,037	1,306	0,028	0,988
F1 JMA - n = 1	0,094	0,037	0,810	0,028	0,969
R2 two - dimensional phase	0,228	0,046	0,638	0,035	0,926
R3 three dimensional phase boundary	0,187	0,044	0,689	0,033	0,942
F2 JMA - n = 1/2	0,496	0,035	0,402	0,026	0,897
F3 JMA - n = 1/3	0,646	0,028	0,272	0,021	0,861
F4 JMA - n = 1/4	0,726	0,023	0,206	0,017	0,841
F5 JMA - n = 2/5	0,584	0,031	0,324	0,023	0,876

Acknowledgements

First of all, I would like to express my sincere gratitute to Dr. Claudio Pistidda, Dr. Martin Dornheim and Prof. Dr. Thomas Klassen who made it possible to conduct my studies at Helmholtz Zentrum Geesthacht. I am grateful for their kind supervision. I appreciate the funding from CAS-HZG collaborative project ‘‘RevHy’’ – ‘‘Study on the synthesis, structures and performances of complex hydrides systems for Reversible high capacity Hydrogen storage at low temperatures’’.

Besides, I would like to thank to all collaboration partners. I thank to the beamline scientists Dr. Jo-Chi Tseng and Dr. Jozef Bednarcik from ‘DESY – Hamburg, Germany’ for the allocation of beamtime and support with data collection. I thank to Dr. Thomas Gemming for TEM observations and to Maria Victoria Castro Riglos for TEM analysis. Dr. José Martín Ramallo-López and Dr. Martin Mizrahi are acknowledged for performing X-ray absorption spectroscopy measurements.

I thank to all colleagues from HZG, especially to Dr. Claudio Pistidda and Dr. Julián Puszkiel for the support during my studies. I want to thank to my friends Dr. Antonio Santoru and Dr. Thi Tu Le for the moments we had together during my PhD. Dr. Hujun Cao and Dr. Giovanni Capurso was very kind and always helpful, Oliver Metz always helped me with technical matters.

Finally, I would like to thank to my family. My dear family, particularly my father, mother and brother always encouraged and supported me with my decisions. I thank to my wife and my children from the bottom of my heart. Their love, energy and motivation made me always stronger.

Curriculum vitae

Personal Information	
Name:	Gökhan Gizer
Nationality:	Turkish
Date of Birth:	16/10/1988
Place of Birth:	Ağrı, Turkey

Professional experience	
2014 – Today	Helmholtz-Zentrum Geesthacht Institute of Materials Research / Nanotechnology Department Scientific researcher

Education	
2014 – Today	Helmut-Schmidt-University, Department of Mechanical Engineering Target degree: Ph.D.
2012 – 2014	Hacettepe University, Department of Nanotechnology and Nanomedicine Degree: Master Degree
2007 – 2012	Karadeniz Technical University, Department of Physics Degree: Bachelor Degree